# Self-Organization of Bioinspired Fibrous Surfaces

Dissertation advisor
**Joanna Aizenberg**

Author
**Sung Hoon Kang**

# Self-Organization of Bioinspired Fibrous Surfaces

## Abstract

Nature uses fibrous surfaces for a wide range of functions such as sensing, adhesion, structural color, and self-cleaning. However, little is known about how fiber properties enable them to self-organize into diverse and complex functional forms. Using polymeric micro/nanofiber arrays with tunable properties as model systems, we demonstrate how the combination of mechanical and surface properties can be harnessed to transform an array of anchored nanofibers into a variety of complex, hierarchically organized dynamic functional surfaces. We show that the delicate balance between fiber elasticity and surface adhesion plays a critical role in determining the shape, chirality, and hierarchy of the assembled structures. We further report a strategy for controlling the long-range order of fiber assemblies by manipulating the shape and movement of the liquid-vapor interface. Our study provides fundamental understanding of the pattern formation by self-organization of bioinspired fibrous surfaces. Moreover, our new strategies offer a foundation for designing a vast assortment of functional surfaces with adhesive, optical, water-repellent, capture and release, and many more capabilities with the structural and dynamic sophistication of their biological counterparts.

# Table of Contents

# Acknowledgements

I feel the course of Ph.D. is like a journey. The journey has a lot of ups and downs. It becomes exciting as one finds good companion along the roads and sees the hidden treasures. My Ph.D. has been an exciting journey due to many people that I was fortunate to interact and get inspiration.

First of all, I would like to thank my advisor Prof. Joanna Aizenberg for her support and guidance. Joanna gave me freedom and environment that I could explore various interesting topics at the interface among different disciplines. Thanks to her supervision, I had opportunities to work with great people and develop myself as an independent researcher. I also would like to thank my committee members. It has been fun to work with Prof. L. Mahadevan for his breath and depth of knowledge as well as his insights capturing underlying principles of various interesting phenomena. Especially, I am grateful to Maha for his help on my assembly project through his scaling analysis and discussion about adhesion-mediated elastocapillary interaction. I like to thank Prof. Katia Bertoldi for wonderful collaboration on understanding mechanisms of buckling-induced pattern formation. Discussion with Katia and colleagues has been always inspiring and fun. I am grateful to Prof. Vinothan Manoharan for his time and advice.

I also would like to thank other faculty that I was fortunate to interact. I am grateful for Prof.

Frans Spaepen for his course (Applied Physics 282, Solids: Structure and Defects) and his advice and comments. Frans' course gave a lot of inspiration for my research because I feel there are a lot of similarities between classical material science theory and the mesoscale phenomena that I worked with. I also appreciate him that he spares time for students so that one can ask questions of broad subjects. I like to thank Prof. Shriram Ramanathan for his help when I applied to Harvard for Ph.D. study. Shriram's help and encouragement were crucial for starting my Ph.D. study at Harvard. I am also grateful to Dr. Ian Morrison for his course (Applied Physics 226, Capillarity and Wetting) through which I was introduced the topic of capillarity and wetting.

I am also grateful to my collaborators, Mr. Sicong Shan of Bertoldi group, Dr. Agnese Seminara of Brenner group, Dr. Darren Lipomi of Whitesides group, Mr. Mikhail Katz of Capasso group, and Dr. Mughees Khan of Wyss Institute for their help and discussion.

I like to thank my lab mates with whom I have enjoyed my Ph.D. study. I am grateful for Dr. Boaz Pokroy, who used to be a postdoc in our group and now a professor at Israel Institute of Technology. With Boaz's guidance and encouragement, I was introduced to my thesis topic and could jump start my research. I would like to thank Alexander Epstein and Lidiya Mishchenko who have spent four years together as first three students who joined the group. I enjoyed time with them and I send my best wishes for their future. I like to thank Drs. Ning Wu, Alison Grinthal, Tak Sing Wong, Wim Noorduin, Philseok Kim, Wendong Wang, Oguz Umut Salman,

and Prof. Lev Truskinovsky (Ecole Polytechnique), whom I have collaborated with. I also enjoyed conversation with them regarding various topics. I am also grateful to a visiting summer student, Mr. Francis Gibaud from Ecole Polytechnique and an undergraduate student Mr. Jacob Kureh from Harvard, who worked together on my assembly project. Francis and Jacob's insights and dedication were helpful to understand the assembly process better. I am also grateful to rest of Aizenberg group members (Dr. Benjamin Hatton, Dr. Allon Hochbaum, Dr. Michael Bucaro, Dr. Ximin He, Ms. Lauren Zarzar, Dr. Yolanda Vasquez, Mr. Ian Burgess, Dr. Sindy Tang, Dr. James Weaver, Dr. Elisa Maldonado, Dr. Mathias Kolle, Mr. Ronn Friedlander, Dr. Xi Yao, Ms. Ankita Shastri, Dr. Roy Ziblat, Dr. Xu Hou, Dr. Nicholas Vogel) who opened my eyes on various topics and helped me in many aspects. I appreciate Ms. Marina DiDonato-McLaughlin for her administrative support to take care of a large number of people.

I would like to thank staffs of the Harvard Center for Nanoscale Systems, especially Dr. Dave Lange for his help on scanning electron microscopes and Mr. Ed Macomber for his help on sputtering and evaporative deposition systems. I would like to thank the National Science Foundation for their financial support through the Harvard the Materials Research Science and Engineering Center and the Center for Nanoscale Systems and the Air Force for their financial support.

I am really grateful for my wife's family, my parents-in-law and sister-in-law, without their

help, I could not continue my Ph.D. study. I also thank my parents for their continuous support.

Finally, I would like to thank my family, my wife, Kiryoung and my daughters, Narae and Narah, who have been always with me during all ups and downs of my journey. I cannot thank enough for their love and support.

# List of Figures

# List of Tables

# Chapter 1 Introduction

## 1.1. Interesting phenomena from interaction of structured solids with stimuli

Life is full of dynamic behaviors. Our body encounters various situations during daily activities and responds in many different ways depending on stimuli. In contrast, most of synthetic materials systems are rather static. Their properties are not dynamically changing as biological systems do. As a result, we need to find a different material suitable for each circumstance. Inspired by natural systems, we are interested in developing dynamic materials systems that can reconfigure themselves by interaction with stimuli. Realizing dynamic materials systems gives us a new challenge for scientific studies, but it will be rewarding effort because it can uncover new phenomena that will deepen our understanding of physics and open new applications that will benefit our life.

To address the question, we have been interested in a variety of phenomena happening by interaction of solids with stimuli. We have investigated structured solids at various length scales, which can respond to stimuli such as liquids and electromagnetic waves. Introducing structures on solids can open exciting opportunities to make stimuli-responsive material systems. For

example, structured solids can move and/or change shapes by liquids or electromagnetic waves. If we place a drop of a liquid on a flat material such as a piece of plastic, nothing interesting happens on a solid. However, if we introduce structures on the same material as Figure 1[1] and put a liquid, intriguing patterns appear as the liquid evaporates as shown in Figure 2[2]. Moreover, if we structure the liquid using another identical structured surface, complex ordered patterns appear as Figure 3[1]. Besides formation of pattern, if we infuse a liquid into a structured material and place another immiscible liquid, the composite surface can show a remarkable liquid-repellent behavior for a wide variety of liquids and even solids[3]. In addition, instead of applying a liquid, if we scan with an electron beam the same structure as shown in Figure 1, the fibers bend by the interaction with the beam as shown in Figure 4[4]. These and other interesting phenomena of the interaction of structured, fibrous surfaces with various stimuli, such as exposure to a liquid or e-beam make the subject of this thesis.

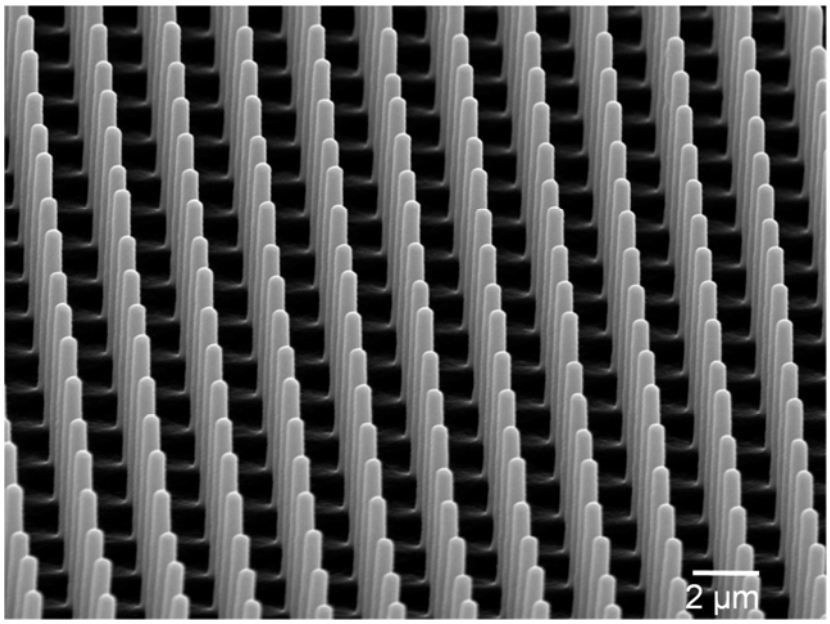


Figure 1. A scanning electron microscope (SEM) image of a structured surface composed of a square array of nanofibers. Reprinted from ref. 1 with permission from American Physical Society.


Figure 2. An image of a single fiber arrays shown in Fig. 1 self-organized into a complex pattern by interaction with an evaporating liquid. The image was taken with a SEM and was digitally enhanced for color. Reprinted from ref. 2 with permission from AAAS.

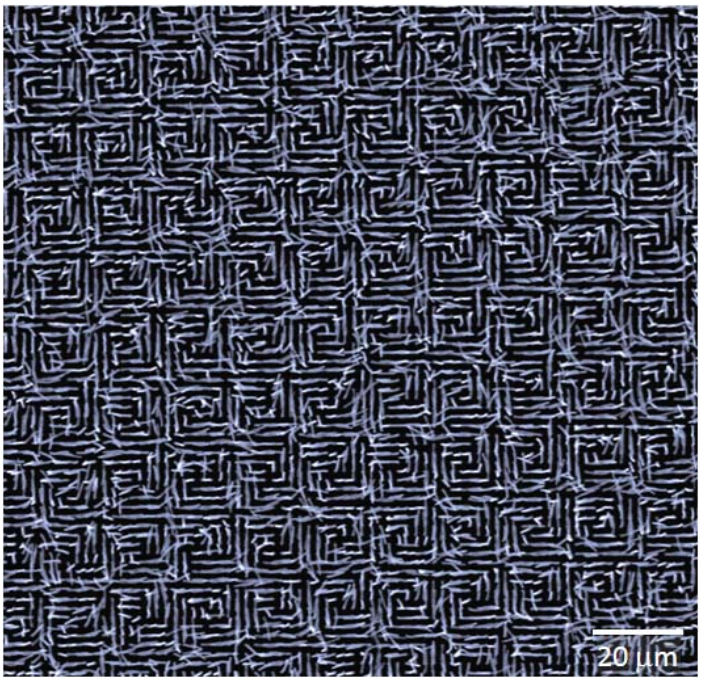


Figure 3. A complex Moire pattern with a long-range order generated by interaction of two superimposed fiber arrays shown in Figure 1 with a structured liquid. Reprinted from ref. 1 with permission from American Physical Society.

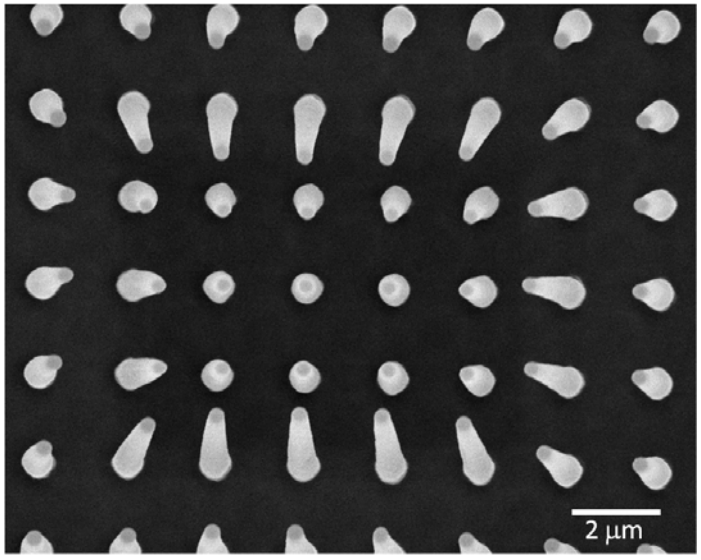


Figure 4. Nanofiber arrays bent toward the center of the image by electron beam. Reprinted from ref. 4 with permission from American Physical Society.

## 1.2. Inspiration from natural fibrous surfaces with unique properties

Among many structured materials, we have been focused on fibrous surfaces that have been widely used in nature. Fibrous surfaces have properties that make them versatile in various natural systems. For example, their high surface area to volume ratio provides many ways to interact along its length and gives mechanical flexibility to deform into a variety of ways[5]. Moreover, as the feature size approaches a micro- and nanoscales, the fibers become much more flexible with the bending force comparable to surface forces[2].

By controlling its orientation, assembly, and movement, a fibrous surface may display a variety of intriguing characteristics. For example, cilia in lungs can sense foreign objects and can transport them by its motion[6]. Water strider uses its fibrous legs for striking capability of walking on water[7]. A gecko can climb onto almost any surface by using its hierarchical fibrous surfaces. There are many different species that utilize fibrous surfaces for adhesion[8]. Inspired by many interesting natural examples, there have been a lot of efforts to make synthetic functional surfaces with properties such as water-repellency[9,10], pumping and mixing of fluids[11], and sensing of molecules[12].

However, if we want to make synthetic fibrous surfaces to develop functional surfaces, there is a challenge known as clustering or lateral adhesion, which has been observed in a variety

of material systems such as carbon nanotubes[13], nanowires[14], and polymer microstructures mimicking the foot of a gecko[15]. It was reported that the clustering phenomenon happens when a solvent evaporated during processing[16]. The clustering behavior has been considered as a detrimental effect that leads to the uncontrolled collapse of structures. Similar phenomena are also observed in nature such as the tarsi (segmented foot) of a beetle (*Hemisphaerota cyanea*)[17]. But, in the case of the beetle, the clustering is reversible and the insect utilizes this phenomenon to control its foot adhesion to surfaces by manipulating the extent of the bundling of its fibrous segmented foot[18].

While we can avoid the clustering phenomena by making fibers stiff and changing surface properties to prevent interaction with their neighbors, the self-assembly behavior of fibrous surfaces can provide unique opportunities to make complex hierarchical structures which cannot be achieved by other methods. In addition, the surface-attachment of fibers gives us additional parameters to manipulate the assembly process such as asymmetry, long-range order, and reversibility[19].

## 1.3. Pattern formation by interaction of fibrous surfaces with a liquid

In the previous section, we mentioned that the assembly happens when a solvent evaporates during processing. The mechanism of the clustering is following. When a drop of a liquid forms on a surface, there is a force that tries to minimize the surface area, which is called as a surface tension[20]. If we introduce a liquid onto two fibers as Figure 5, there is a force from surface tension that tries to minimize the surface area, which attracts two fibers. Moreover, there is a counteracting elastic force because fibers are attached to a substrate. In addition, there is an adhesion force between fibers as they touch each other. The interaction of these three forces can generate complex patterns.

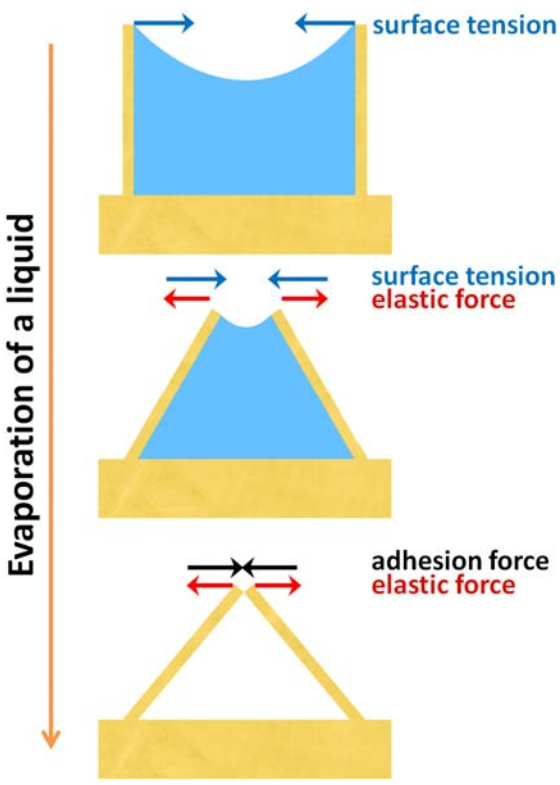


Figure 5. Schematic of an assembly of two fibers by an evaporating liquid. The arrows in the figure show the directions of forces acting on the fibers.

## 1.4. Motivation of this study and key questions to address

In literature, there have been several studies to understand the pattern formation of fibrous surfaces. Kim and Mahadevan studied the effect of elastic modulus on the deformation behavior of macroscopic sheets. By considering capillary and elastic forces acting on the sheets, they showed good agreement between theoretical and experimental shapes of sheets[21]. In addition, Bico and his colleagues reported hierarchical bundling of fibers of a wet brush as they withdrew a brush from a bath of a liquid. By balancing capillary and elastic energies for multiple fibers,

they obtained the relation between the bundle size and the dry length of fibers, which showed good agreement with experimental results[22]. In both cases, the phenomena were explained by competition between the elastic and capillary force terms.

To extract relevant parameters affecting the assembly based on the information about the forces acting in the assembly process, we have raised the following questions:

1) **What are the parameters that affect the assembly of fiber arrays?**
2) **How can we form complex patterns, for example, chiral structure and/or hierarchical patterns often observed in nature, by controlling parameters of the self-organizing system?**
3) **How can we control the long-range order of the assembly?**

To address the questions above, we have been studying:

1) formation of hierarchical chiral patterns by self-organization of fibrous surfaces **(Chapter 2)**
2) how to control the shape and size of the assembling fibers by changing the properties of fibrous surfaces **(Chapter 3)**
3) formation of a long-range order by controlling the liquid-air interface shape using the superposition of fibrous surfaces **(Chapter 4)**
4) formation of large-area, uniform assembly patterns by manipulating the movement of the

liquid-air interface **(Chapter 5)**

5) kinetics of the hierarchical assembly by using an analytical method based on a spring-block model **(Chapter 6)**
6) movement of fiber arrays by electron beam and its potential use in patterning **(Chapter 7)**
7) application of assembly phenomena as security features based on optical effects from structural changes **(Chapter 8)**
8) controlling pattern formation from cellular structures by swelling-induced buckling **(Chapter 9)**
9) liquid-infused structured surfaces that can repel various liquids and solids by minimizing surface adhesion **(Chapter 10)**

The summary of our findings and a perspective of our work are provided in **Chapter 11.**

# Chapter 2 Hierarchical Chiral Assembly

In chapter 2, we have studied how we can form complex patterns by self-organization of fibers, focusing on hierarchical and/or chiral patterns which are abundant in nature, but difficult to achieve using photolithography process. This chapter is based on our published paper (ref. 2). The content is used with permission from AAAS.

## 2.1. Chirality

Non-centrosymmetric chiral, coiled, and spiral configurations are ubiquitous in nature, spanning from amino acids to mollusk shells to galaxies[23]. On a mesoscopic scale, such structures are abundant in biological systems, and these are usually composed of helical fibers that are often further assembled into higher-order hierarchical materials. Natural examples include DNA helices, amyloid fibers[24], cellulose fibrils in wood[25], hierarchy in bone[26,27], and chirally spinning nodal cilia[28], to name a few, with implications on a variety of functions from information transfer to mechanical integrity and control of the body symmetry in morphogenesis. Man-made coiled and spiral materials and designs on a macroscopic scale are widely used in our everyday life—from ropes and bolts to helicopter rotors. On the molecular scale, chirality plays a

critical role in asymmetric chemical synthesis and catalysis[29], liquid crystals[30], supramolecular chemistry[31,32], and organic and inorganic crystal engineering[33]. Artificial coiled structures at the mesoscale are rare, and these usually have simple geometries of one-dimensional helical fibers and ribbons[23,30-32,34]. At any length scale, twist and handedness in superstructures generally originate from either the assembly of noncentrosymmetric building blocks or the application of a chiral field or template[23-27,30-35]. We have uncovered a unique phenomenon of capillarity-driven self-organization of a nanobristle into helical clusters and demonstrated for the first time, the fabrication of nontrivial, hierarchically assembled, coiled mesostructures over large areas, in which neither the assembling elements nor the environment are chiral, guided by and consistent with simple theoretical considerations.

## 2.2. Scaling analysis

Our approach is presented in Figure 6a. We consider a periodic array of nanofibers, each of which is anchored at one end on a substrate and free at the other. A locally stable configuration of the bristles is just a uniform array of non-interacting straight fibers (first-order structures). However, this is not necessarily a globally stable state: When the array is immersed in a liquid that is then evaporated, capillary forces associated with the liquid/vapor menisci between the free ends of the geometrically soft bristles may cause them to deform laterally and adhere to each

other. The effect of elastocapillary coalescence[36] has been described for a well known phenomenon of clumping in wet hair[22] or paintbrush immersed in paint[21]. Similar clustering behavior is observed in nature in the examples of the tarsi of beetles[17] and spiders[37]. The morphology and dynamics of the ensuing structures are a result of the competition between intrafiber elasticity and interfiber adhesion[21,22,36]. Individual fibers that are long enough can bend easily to accommodate the capillary forces associated with the menisci between adjacent fibers.

A simple scaling analysis allows us to construct a set of rough criteria for the existence of these structures, in terms of the properties of the elastic circular nanofibers of diameter $D$, height $h$, interfiber distance $p$, Young's modulus $E$, bending stiffness $B \sim ED^4$, and adhesive energy[38] per unit area $J$ as well as the properties of the evaporating liquid of interfacial tension $\gamma$, in which they are immersed. Assuming that the fibers do not break through the meniscus, the longitudinal forces due to the pinned contact line cause the fibers to buckle[36]; however, because the fibers have a circular cross section, there is no preferred plane of buckling. In addition, the multiple pinned menisci attract each other via a weak capillary interaction mediated by the interface[39]. For the fibers to come together, the force $F_B \sim Bp/h^3$ to bend two adjacent fibers until they are just in contact at their tips must be comparable to the capillary force $F_C \sim \gamma D$ due to the menisci connecting the hemispherical ends. This yields a critical fiber height $h_c \sim (Bp/\gamma D)^{1/3} \sim (Ep/\gamma)^{1/3} D$, below which capillary forces will be unable to maintain a bent configuration and the bent fibers

return to their upright state once the liquid has evaporated (regime I). When $h > h_c$, two neighboring fibers can retain contact as long as they are held together by either capillary forces or short-range van der Waals forces (after drying). A different characteristic length scale, $h_a \sim (Ep/J)^{1/3}D$, based on interfiber adhesion dictates whether the fibers will stay in their adhered state once capillary forces bring them together; for instance, if $h_a > h_c$ and $h_a > h > h_c$, the fibers will come together during the drying process but then separate eventually, corresponding to regime I. (These length scales may be modified by the wettability of the fibers.). When $h > h_c$ and $h \geq h_a$, we expect the fibers to form second-order stable clusters that usually reflect the symmetry of the underlying lattice (regime IIa). When $h >> h_a$, the fibers can cluster to increase their adhesive contact via a chiral rearrangement of the fibers (regime IIb) and eventually twist around each other (regime IIc).

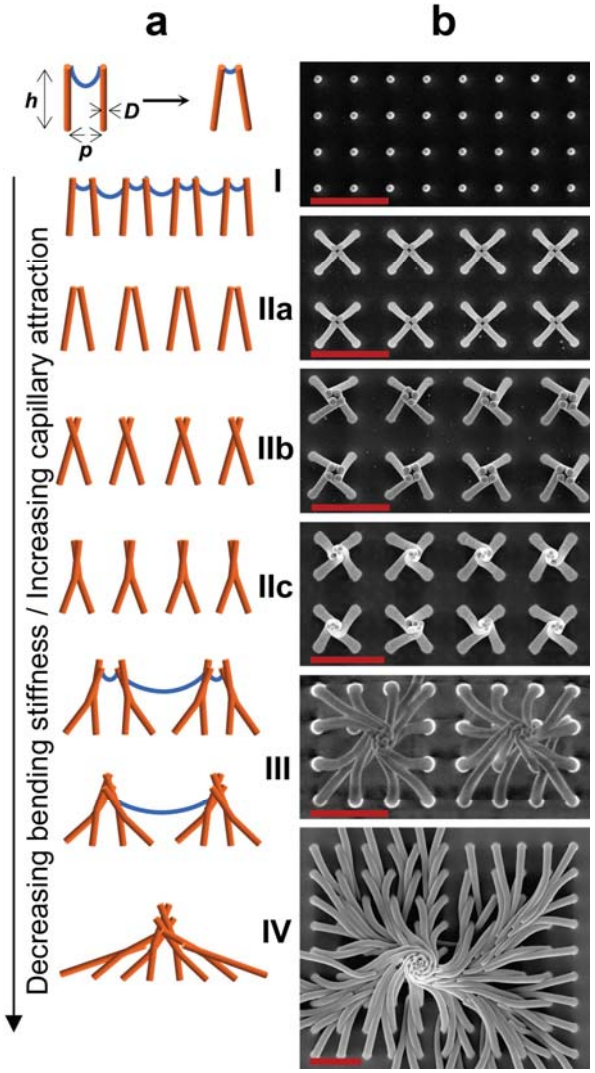


Figure 6. (a) Schematic diagram and (b) SEM images of hierarchical chiral assembly of nanofiber arrays. Scale bars are 4 μm. Reprinted from ref. 2 with permission from AAAS.

To understand this in a minimal model, we consider the adhesion of two initially straight free fibers wound around each other along uniform helices of pitch $p$ and radius[38] $R$. Adhesive contact can now occur over a patch of approximately constant width $a$ that winds around each fiber and is determined by the solution of a Johnson-Kendall-Roberts model-like problem[40], yielding $a \sim (J/E)^{1/3} R^{2/3}$ [up to logarithmic factors of the form $\ln(h/R)$]. Then, the total energy of

two fibers of length $h$ is the sum of the adhesive energy and the elastic energy (assumed to be caused by bending alone) and can be written as $U \sim -J_a h(1 + 1/P^2)^{1/2} + Bh/R^2(1 + P^2)^2$, where $P = p/2\pi R$. Here, the first term corresponds to the energy of adhesion between two helices, whereas the second term corresponds to the elastic energy required to deform a naturally straight fiber into a helix. For relatively stiff fibers, when $B/J_a R^2 > 1$, it is evident that the minimum energy solution favors $P \rightarrow \infty$ (i.e., straight fibers); whereas for soft fibers, when $B/J_a R^2 \leq 1$, minimizing U requires that the dimensionless pitch be as small as possible, which may be achieved by having $R \sim D/2$, $P \sim O(1)$ [i.e., a tightly wound helical configuration maximizing the length of contact between the fibers and corresponding to a second-order cluster (regime IIc)]. For fibers that have rotationally symmetric circular cross sections and are driven by a homogeneously drying front, the chirality of an individual cluster should be random. However, any asymmetry in the fiber cross section, fiber orientation, or the direction of the drying front can clearly lead to a specific handedness in the pattern. In any event, these helical clusters will then interact via the meniscus-driven capillary field to form higher-order coiled assemblies (III, IV,…) until the growing assembly is eventually halted by the elastic field that penalizes large deformations[22].

## 2.3. Experimental demonstration of hierarchical chiral assembly

To test these ideas, we studied the evaporation-induced self-assembly in a square array of epoxy nanofibers fabricated as described previously[5]. Droplets of wetting liquids (including anhydrous ethanol, isopropyl alcohol, anhydrous toluene, acetone, and mixtures of ethanol and water at different ratios) were placed on horizontally oriented substrates ($p$ = 2 μm, $D$ = 300 nm, $h$ = 4 to 9 μm, $E$ = 0.1 to 2 GPa, and controlled wall roughness) and were allowed to evaporate at ambient conditions. The evaporation-induced interactions and self-organization of the bristle were studied with the use of optical microscopy (Leica DMRX connected to a QImaging Evolution VF cooled color CCD camera) and a field emission scanning electron microscope (Zeiss Ultra 55). The resulting structures were in substantial agreement with the simple theory sketched above, and all of the predicted structures—from the first-order unclustered nanobristle to the fourth-order helical bundles—were observed (Figure 6b). By using a periodic square array of nanofibers, we achieved a long-range order in the assembled bristle, such that large-area (up to millimeters), uniform domains of highly periodic bundles were generated from the nanometer-sized building blocks. Figure 7(a) illustrates the mechanism for the propagation of order in the array of the assembling fibers. When the liquid evaporates to the level of the free tips, a meniscus connecting the neighboring fibers is formed. In an equally spaced array, the lateral

capillary forces acting on each fiber are fully balanced, and no lateral movement occurs. However, imperfections and instabilities, which include local differences in the evaporation rate, pinning of the contact line, and variations in the interfiber lattice spacing, will nucleate the first fiber cluster at a particular location rather than randomly (for example, between fibers h and g). As a result, the next fiber i will sense an anisotropic force field where $F_{ih} < F_{ij}$ and will bend in the direction of the fiber j. This process will propagate through the bristle and generate long-range ordered domains (Figure 7a). For example, to bias the system to form periodic second-order bundles over a large area, we chose conditions that would lead solely to the formation of clusters of four bristles whose stiffness would not allow their further assembly into higher-order structures. Epoxy bristles with $E$ = 1 GPa, $D$ = 300 nm, $h$ = 5 μm, and $p$ = 2 μm immersed in ethanol as a wetting liquid satisfied this condition. Figure 7b shows a fragment of the corresponding assembled structure with the marked long-range order.

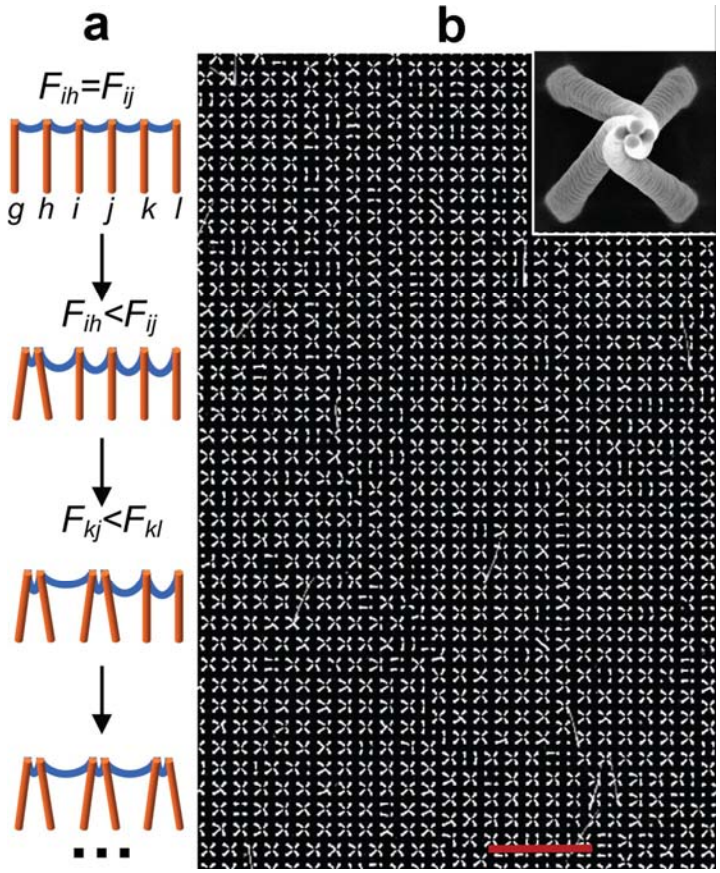


Figure 7. (a) Schematic diagram showing the mechanism of the propagation of the assembly of fibers and (b) a large area SEM image with uniform clusters of four nanoposts. Here domains appear due to multiple nucleation sites of the assembly. Scale bar is 20 μm. Reprinted from ref. 2 with permission from AAAS.

## 2.4. Kinetics of the assembly

A detailed microscopy study shows that the cluster twisting is a dynamic, multistep process with distinctive kinetics and a growth mechanism that involves the sequential coalescence of self-similar coiled blocks to yield organized helical patterns on very large scales (Figure 8a). To achieve the formation of higher-order structures III to V, the nanofibers were specifically designed to have rough, banded walls. In addition to increasing flexibility, this segmented,

"wormlike" geometry (Figure 8a, inset) provides the pinning of the receding contact line by reentrant curvature [41,42] and, thus, an increase in the capillary attraction necessary to bring the larger clusters together. The history of the hierarchical assembly process is imprinted in the makeup of the final helical structures: The lower-order braids and bundles can be clearly identified in the larger coiled clusters (Figure 6b and Figure 8a). The kinetics of this multistep process is depicted in Figure 8b. Because the instabilities leading to the chiral rearrangement of the clustered fibers are random, a mixture of bundles with the right- and left-handed twist was observed.

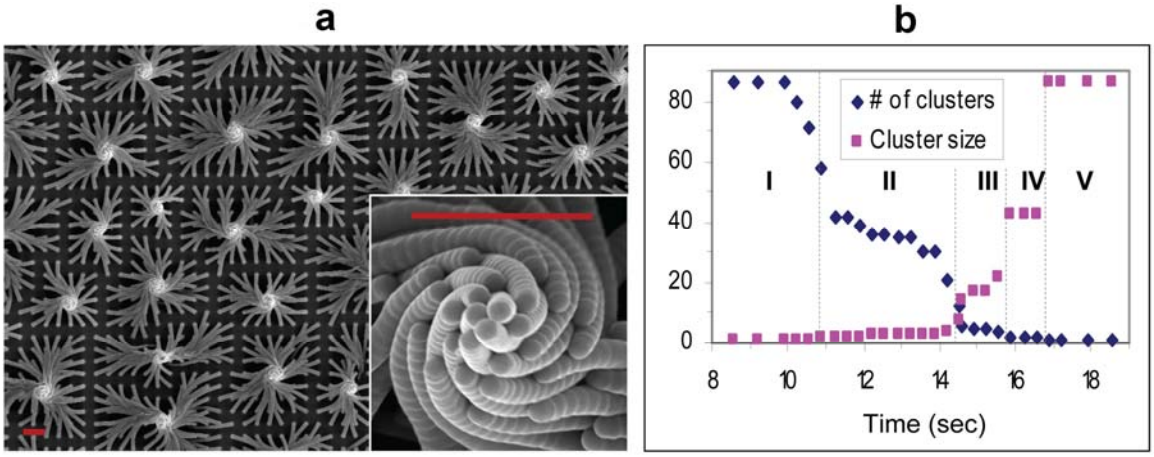


Figure 8. (a) SEM showing an array of fibers ($h$ = 8 μm) self-organized from the ethanol solution into the level IV and V helical assemblies. (Inset) Magnified view of the coiled core. Scale bars, 3 μm. (b) Kinetics of the hierarchical assembly. The growth of one representative cluster is shown. The cluster size is defined as the number of fibers in the bundle. The multistep, sequential coalescence of the small blocks into higher-order structures is apparent. The y axis denotes the number or size of clusters. Reprinted from ref. 2 with permission from AAAS.

## 2.5. Control of chiral assembly

To optimize our system to achieve the uniform handedness of the clusters, we used two approaches to the bristle design. The fibers were either (i) rendered elliptical in cross section or (ii) an array of tilted fibers was used[5]. The ellipses' axes or the tilt direction of the fibers were chosen to make a small angle with the principal unit cell directions in the underlying square lattice (Figure 9a). Such a design induces anisotropy in the stiffness of the bristle that results in a directional, off-axis bending of the fibers under the influence of the capillary forces and allows us to form an ordered array of helices with uniform controlled right- or left-handedness (Figure 9a). This is similar in concept to the use of a pre-tilt layer in liquid crystal displays to bias otherwise vertically aligned nematic crystals and prevent the formation of defects during switching[43]. Alternatively, the pattern and orientation of the assembled coiled bundles could also be orchestrated by changing the direction of the evaporation front. The Figure 9b provides an example of the latter approach—a woven carpet composed of braids of nanofibers uniformly plaited parallel to the surface—that results from the evaporation front moving parallel to the substrate.

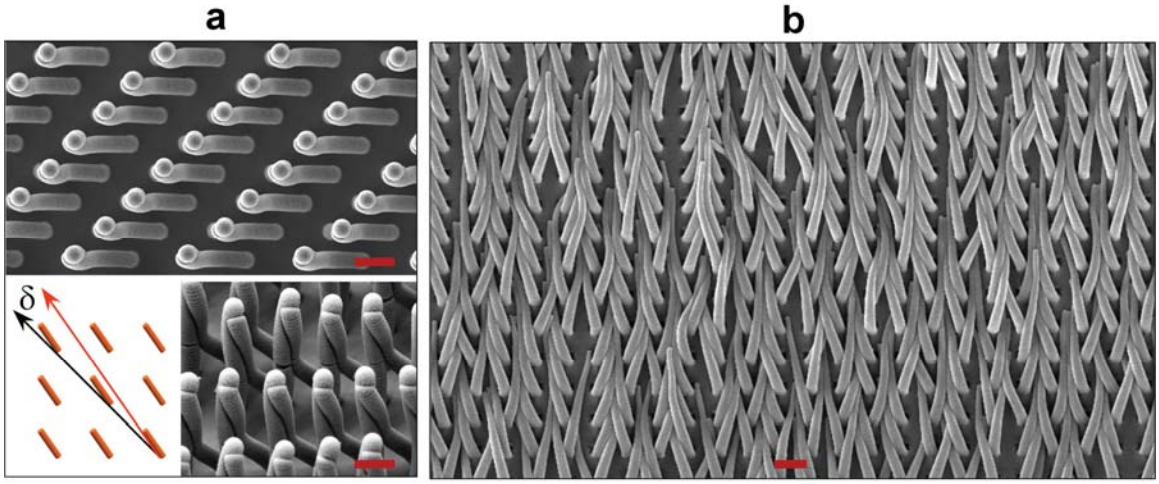


Figure 9. (a) Top and angled SEM views showing an array of ordered helical pairs with uniform handedness. (Inset) Schematic diagram that illustrates the substrate design. The bristles were first tilted in the direction that forms a small angle δ with the principal diagonal direction of the underlying square lattice (shown by the red and black lines, respectively) and then allowed to assemble. (b) Evaporation along the surface results in the woven braids assembled parallel to the substrate. Scale bars, 2 μm. Reprinted from ref. 2 with permission from AAAS.

## 2.6. Summary and possible applications

Recent studies show that the adhesive properties in a variety of biological systems arise from the conformal attachment of microscopic fibers to surfaces and objects and their subsequent entanglement[17,18]. The observed mechanical interlocking in our artificial, spirally assembling bristle can be used in a similar manner and may lead to an effective adhesive and particle-trapping system. Figure 10 shows microspheres that are captured through conformal wrapping and twisting of the nanobristle. The process is equally applicable for attaching to objects with arbitrary shapes and surfaces with various topographies. Though lateral adhesion is

known to occur in high–aspect ratio structures such as photoresists and soft lithographic stamps[44,45], arrays of carbon and ZnO nanotubes[46,47], and biomimetic setal adhesives[15], this process has been generally described as an unwanted outcome that leads to the uncontrolled collapse of the structures. The clustered features were usually irregular in size, and no order over the large area was observed unless templating was used[48]. Here we have demonstrated that the process can, in fact, be finely tuned to yield organized nontrivial, helical assemblies with controlled size, pattern, hierarchy, and handedness over large areas. These mesoscale coiled structures may be useful in a number of applications: They have the ability to store elastic energy and information embodied in the adhesive patterns that can be created at will. Additionally, they may be used as an efficient adhesive or capture-and-release system, provide the foundation for hierarchically assembled structural materials, and be used to induce chiral flow patterns in the ambient flow and thus be applied for enhanced mixing and directed transport at the micron and submicron scale. These structures may serve as the seed for the spontaneous breaking of symmetry on large scales, just as chirally spinning cilia ultimately control the left-right asymmetry in vertebrate morphogenesis[28].

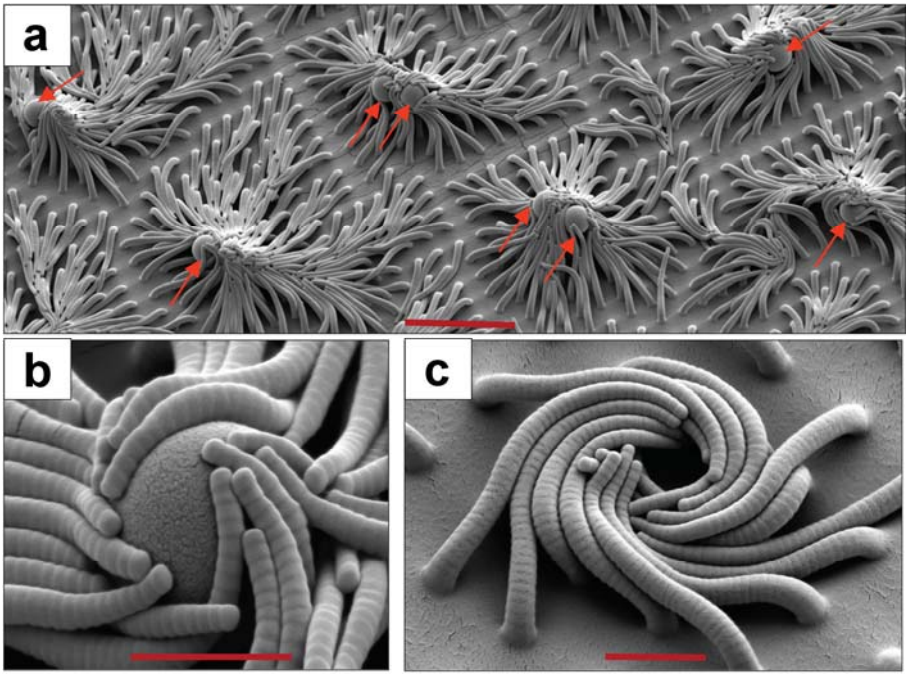


Figure 10. (a) Low-magnification SEM showing the capture of the 2.5 μm polystyrene spheres (indicated by arrows). Scale bar, 10 μm. (b) Magnified view depicting a single sphere trapped through the conformal wrapping of the nanofibers. Scale bar, 2 μm. (C) Coiled whirlpools remain after the removal of the spheres. Scale bar, 2 μm. Reprinted from ref. 2 with permission from AAAS.

# Chapter 3 Control of Assembly by Manipulating Fiber Properties

In chapter 3, we have studied how we can control the shape and size of the assembly by changing the properties of fibers. To address this issue, we have systematically varied the properties of fibers and developed a model based on the previous studies and our new experimental observations. This chapter is based on our published paper (ref. 49). The content is used with permission from American Chemical Society.

## 3.1. Introduction

Self-assembly is becoming increasingly important as a bottom-up route for building novel structures and controlling functions at length scales ranging from the nanometer to millimeter[50-52]. As current miniaturization methods for microelectronics and robotics approach their theoretical limit and/or commercially feasible minimum size, self-assembly provides new fabrication and manufacturing strategies that can overcome these challenges[52]. Consequently, much work has focused on the control of assembly at molecular scales[50,51,53], and there is currently a growing interest in understanding and manipulating the assembly process at larger

(submicrometer to millimeter) length scales. Various driving forces for self-assembly have been studied at these larger length scales[54], including gravity[55], magnetic force[56], electrostatic interaction[57], entropy[58], and capillary interaction[59]. Among these, capillary effects have received particular attention at the microscale because of their relatively significant magnitude, tunability, and simplicity[54], and a number of studies have demonstrated the formation of complex two- and three- dimensional structures by this method[60-64]. Among many building blocks, synthetic fibers have been self-assembled by capillarity in a wide range of systems, such as macroscopic hairs of a brush[22], a micrometer scale polymeric surface mimicking the foot of the gecko[15], as well as nanowires[65] and nanotubes[13,66]. However, there was little or no control of the assembly size or pattern in any of these artificial systems unless laborious e-beam prepatterning of the array was used[67]. Our study is inspired by a wide range of biological systems in which assembly of nanofibers has functional significance. Just as a tantalizing example, the beetle *Hemisphaerota cyanea* controls the assembly size of its tarsi (segmented feet) by adjusting the secretion of an oily liquid to adjust its adhesion to a surface[17].

We are interested in investigating the relation between the intrinsic features of the nanoscale building blocks and the final assembly pattern as a basis for selecting parameters that specify desired structures. Despite several works reporting the self- assembly of synthetic fibrous surfaces, relatively little is known about how the many parameters of the system influence the

size and kinetics of self-assembly. In previous studies, the contributions of the properties of building blocks to the assembly process were described by competition between elasticity and capillarity for wet macroscopic systems[21,22,68], as well as microfibers[69,70] and nanoscopic systems such as carbon nanotubes[13] and silicon nanorods[14]. Two studies have analyzed the correlation between assembly size and the aspect ratio of the filaments, their diameter, Young's modulus, and the surface tension of the liquid[14,69]. In scaling terms, both studies used static energy minimization and derived the relationship as equation (1);

$$N \sim \frac{E_C}{E_E} \sim \frac{D^2 \gamma \cos^2 \theta}{D^4 (p-D)^2 E / h^3} \sim \frac{\gamma h^3 \cos^2 \theta}{D^2 (p-D)^2 E} \qquad (1)$$

where $N$ is the average number of fibers in one assembly, $E_C$ is the capillary interaction energy, $E_E$ is the elastic energy term, $h$ is the height of the fibers, $\gamma$ is the surface tension of the liquid, $D$ is the diameter of the fiber, $p$ is the distance between the fibers, $E$ is the Young's modulus of the fiber, and $\theta$ is the equilibrium contact angle of the liquid on the surface of the fibers. However, all of these studies neglected any kinetic effects and assumed that the assembled bundles stay together once they are formed without considering the effects of the adhesion even though it alone maintains the assembly after the system dries and capillary forces disappear.

Going beyond the size of the assembled clusters, their shape may have important implications for nanofabrication of advanced materials. For example, hierarchical chiral architectures provide useful mechanical robustness in cellulose fibrils in wood[25] and mineralized

collagen fibrils in bone[27] or structural color, *via* complex polarization-sensitive structures in beetles[71] and butterflies[72]. In the Chapter 2, we have shown the hierarchical chiral assembly of polymer bristles by evaporative self-assembly without using chiral building blocks or a chiral environment and developed a model for the assembly process based on interaction of elastic, capillary, and adhesion forces[2]. Our theoretical analysis shows that adhesion between the posts by short- range van der Waals forces is important in inducing chirality and determining the size and shape of the final clusters. Since this evaporation-induced chiral assembly of fibers has not been observed in other studies, it is critical to analyze further the factors and conditions that would lead to controlled formation of functionally important structures. In this chapter, using periodic arrays of nanofibers with controlled modulus, geometry, and surface properties (Figure 11), we show how varying the parameters of the fibers associated with capillarity, elasticity, and adhesion gives us simple ways of controlling the chirality, size, and shape of the assemblies.

## 3.2. Experimental methods to control fiber properties

Nanofiber arrays were fabricated by producing negative elastomeric molds of the original fibrous arrays and replicating them in a polymer using the method described earlier (Figure 11a)[5]. Four silicon masters were used in this study. The master #1 had arrays of fibers with a diameter of 250 nm, a height of 8 μm and a pitch of 2 μm. The fiber surface showed a pronounced

scalloping at the side walls due to the fabrication process. This master was used in most parts of this study. Replicas with different moduli and geometries were fabricated from this master using soft lithography-based methods (Figure 11). The master #2 had arrays of fibers with a diameter of 1700 nm, a height of 10 μm and a pitch of 3.5 μm. The master #3 had the same lateral dimensions as #1 and a height of 5 μm. The master #4 has the same feature sizes as the master #1, but it had no scalloping at the top half of the fibers. With the exception for the modulus study, all fibers were made from commercially available UV-curable epoxy (UVO-114 from Epoxy Technology, Billerica, MA). Self-assembly was induced by placing a small volume (10-20 μL) of 200 proof absolute anhydrous ethanol (Pharmco-AAPER) on a sample to cover the entire area and letting the solvent evaporate under ambient conditions. As the solvent evaporated, the fibers assembled and retained a certain assembly pattern after the system was completely dried (Figure 11b). Then, samples were characterized by optical microscopes and/or scanning electron microscopes (SEM). For SEM, the samples were coated with Pt/Pd for 60 sec at 40 mA current with Cressington 208 HR sputter coater for imaging and characterized by JEOL JSM-639 OLV scanning electron microscope or Zeiss Ultra 55 scanning electron microscope. To study the effects of elasticity of the fibers, we varied the geometry (Figure 11c,d) or the modulus (Figure 11e,f). The effect of adhesion was assessed either by using plasma treatment to activate reactive surface functional groups (Figure 11g) or by chemical functionalization of the surface (Figure

11h).

To vary the radius of the fiber, new negative molds with adjusted hole sizes were made by the following procedures. To increase the radius of the replica without changing other parameters, metal films of controlled thickness were deposited to the initial epoxy replica by using the AJA International ATC 2200 sputtering system of Harvard Center for Nanoscale System and then the coated replica was used to make negative molds with increased hole diameters (Figure 11c). From the new molds, epoxy replicas with increased fiber diameters were made. In the case of metal deposition, we used silver for its fastest deposition rate among available target materials, but other materials can be also used. For reduction of the radius of the fiber, plasma etching by Femto plasma cleaner (Diener electronic GmbH) was used to thin down the epoxy replica followed by making negative molds with reduced hole diameters and fabricating replicas with reduced diameters from the new negative molds (Figure 11d).

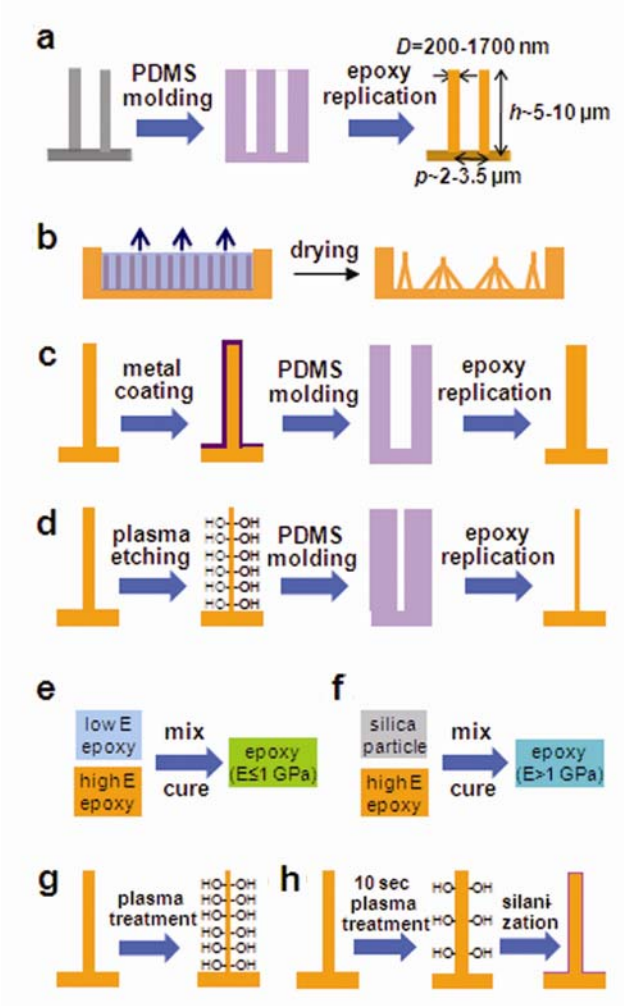


Figure 11. Schematics of the fabrication procedures for making fibers of controlled properties. (a) Schematic of the sample fabrication procedure and the geometry of the arrays of polymeric nanofiber arrays used in the study. (b) Schematic of the assembly of nanofibers by evaporation of the applied liquid. (c-h) Schematics of the methods used to change the parameters of the fibers: (c) increasing the diameter, (d) decreasing the diameter, (e) decreasing the modulus of the fiber ($E \leq 1$ GPa), (f) increasing the modulus of the fiber ($E > 1$ GPa), (g) increasing adhesion, (h) changing the wetting property. Reprinted with permission from ref. 49. Copyright 2010 American Chemical Society.

As another way of varying elastic property of the fiber, we used materials with different moduli by mixing epoxy of different moduli (Figure 11e) or adding inorganic nanoparticles to

epoxy (Figure 11f). In a previous work, it was reported that by controlling the ratio of two liquid epoxy resins, Dow D. E. R. 331™ (stiff epoxy resin) and Dow D. E. R. 732™ (soft epoxy resin) and adding 5 wt% UV cross-linking initiator (Cyracure UVI 6976™, available from Dow), it was possible to change the modulus of the mixed material from ~ 2 MPa to 1 GPa depending on the weight percent of the stiff epoxy resin[5]. In our study, we used this approach to make fibers with a modulus no greater than 1 GPa. The modulus value of the material was taken from the previous work in literature[5]. To make fibers with a modulus higher than 1 GPa, we added small amount (2 wt% or 4 wt%) of hexamethyldisilazane treated $SiO_2$ nanoparticles (available from Gelest, Inc.) to UV curable epoxy resin (UVO 114 available from Epoxy Technology, modulus ~ 1 GPa). Then, the two components were mixed by sonicating with Branson digital sonifier with ice around the container to prevent large increase in temperature from the sonication. After mixing, the mixture was put in a vacuum to remove bubbles before putting them in a negative mold and curing with UV. The flexure modulus of the composite materials were measured using 4 point bending test with Instron 5566 universal materials testing machine by making bulk specimens.

## 3.3. Effects of the fiber diameter on the size and shape of the assembly

To systematically increase the diameter of the nanofibers, the fibers were coated with a metal film of a controlled thickness. This changes both the surface properties and modulus of the resulting fibers while increasing the diameter. To decrease the diameter of the fibers, the surfaces were etched in oxygen plasma for controlled periods of time. This reduces the fiber diameter and also changes the surface properties and therefore adhesive and capillary interaction in the assembling system. To decouple the effect of the geometry from the effect of adhesion, surface tension, and stiffness, both metal-coated and plasma-etched structures were further replicated in the original polymer (Figure 11c,d). When only the diameter of a fiber was increased, while other parameters were kept constant (modulus, $E \sim 1$ GPa; height, $h \sim 8$ μm; and pitch, $p \sim 2$ μm), the number of fibers per assembly decreased (Figure 12a-d) so that $N^{-1} \sim D^2(p - D)^2$, as shown in Figure 12d, consistent with equation (1) , since changing the diameter also alters the spacing between the fibers and, as a result, both the capillary force and the elastic force[14,69]. For large fiber diameters, the final size of the assembly in the dry sample falls slightly below the expected value. Careful analysis of the SEM images (Figure 12c) shows that the assemblies have some anisotropy so that, although larger assemblies were formed initially, they were subsequently divided into smaller clusters. Optical microscope studies confirmed that a bigger assembly was

indeed formed when the system was wet but divided into subclusters when the system dried. This result suggests that the surface adhesion is not strong enough to accommodate the increase in fiber elasticity. The shape of the assembled clusters, however, does not show any gradual transformation with fiber diameter: chirality appears only for a narrow range of intermediate diameters.

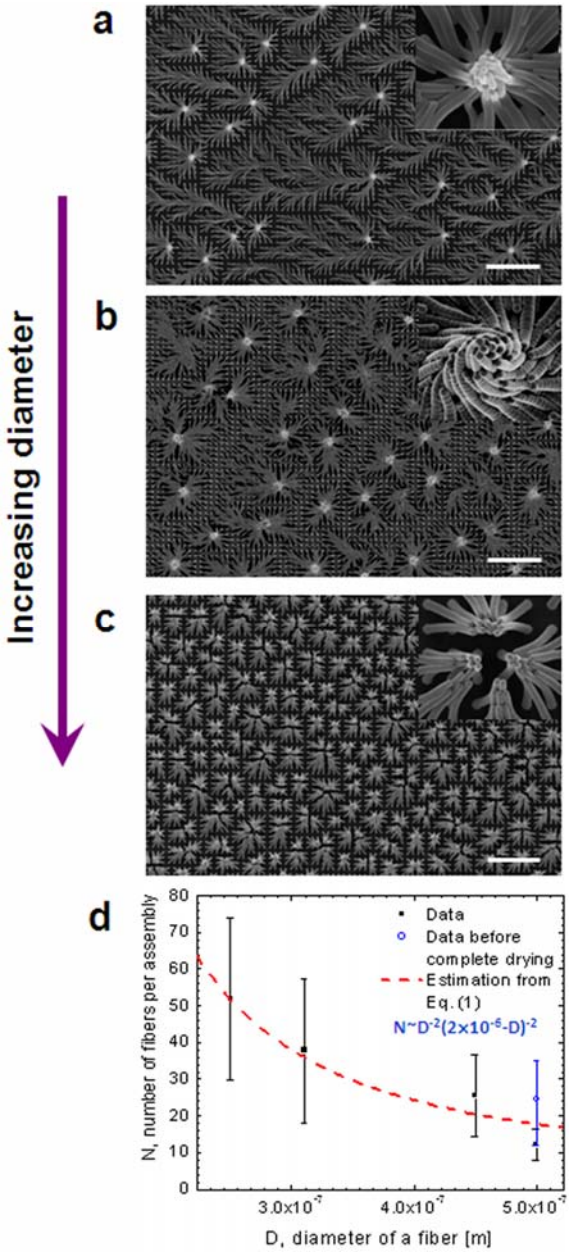


Figure 12. Effect of the fiber diameter on the size and pattern of assembled clusters. (a-c) SEM images showing the assembly of fibers with different diameters: (a) *D*~200 nm, (b) *D*~250 nm, (c) *D*~500 nm. (d) Plot of the number of fibers per assembled cluster as a function of the diameter of a nanofiber for a fixed modulus and length. The modulus and the length of the fibers were 1 GPa and 8 μm, respectively. For all images, the scale bar is 20 μm and the insets show the high-magnification images of each condition. Reprinted with permission from ref. 49. Copyright 2010 American Chemical Society.

## 3.4. Effects of anisotropy of fibers on the size and shape of the assembly

We now extend our study to include the role of anisotropy in fiber cross section and spacing as commonly seen in biologically occurring fibrous surfaces used for sensing[73], adhesion[18], and superhydrophobicity[7]. The simplest way to include the anisotropy is to fabricate fiber arrays by deforming the elastomeric mold[5]. Applying force along a lattice direction to the original mold with the circular holes, as illustrated in Figure 13a, causes the holes to become elliptical and change the lattice parameters. This leads to fibers with an elliptical cross section that assemble into anisotropic clusters as in Figure 13a.

By analyzing SEM images covering an area of 150 μm by 100 μm, we obtained statistics for the size of the assembly along the short and the long lattice axes to decouple effects along each axis and found that the ratio of the assembly size along both axes ($N_1/N_2$) scales with the square of the ratio of the long and the short diameter of ellipses times the ratio of the spacing between fibers as below:

$$\frac{N_1}{N_2} \sim 3.1 \pm 1.5 \approx \left(\frac{E_C}{E_E}\right)_1 / \left(\frac{E_C}{E_E}\right)_2 = (\frac{D_2}{D_1})^2 (\frac{p_2 - D_2}{p_1 - D_1})^2 \sim (1.6 \pm 0.8)^2 (1.1)^2$$

($N_1$: the size of assembly along the short lattice direction, $N_2$: the size of assembly along the short lattice direction, $D_1$: the smaller diameter of the post with elliptical cross-section, $D_2$: the larger

diameter of the post with elliptical cross-section, $p_1$: the distance between fibers along the short lattice direction, $p_2$: the distance between fibers along the long lattice direction). The result is consistent with the prediction from equation (1). (considering that the changes in the lattice spacing and deflection in the direction of the short lattice direction compared to the long lattice direction scales as $(D_2/D_1)^2$ for a beam with elliptical cross-section, since the moments of inertia in the $D_1$ and $D_2$ direction are $I_1 = \frac{\pi D_1^3 D_2}{64}$ , $I_2 = \frac{\pi D_1 D_2^3}{64}$ , respectively and $N_1 \sim \frac{\pi D_1 D_2 \gamma h^3 \cos^2\theta}{\frac{\pi}{64} D_1^3 D_2 (p_1 - D_1)^2 E} \propto \frac{1}{D_1^2 (p_1 - D_1)^2}$ if $\gamma$, $\theta$, $h$, and $E$ are constants.

In addition to changing the cross section and the spacing of the fiber arrays, we can also introduce anisotropy in the array by using tilted fibers[5]. Such an approach allows for the fine-tuning of the size and shape of the assembled clusters. For example, a square array of nanofibers (modulus, $E \sim 1$ GPa; height, $h \sim 5$ μm; and pitch, $p \sim 2$ μm) that forms tetramers similar to Figure 13b if there is no tilting will assemble into achiral dimers by using posts tilted along a lattice direction (Figure 13c). This form of anisotropy can also be utilized to control the chirality. Tilting the fibers slightly off the lattice direction[2] leads to dimers with uniform chirality as shown in Figure 13d.

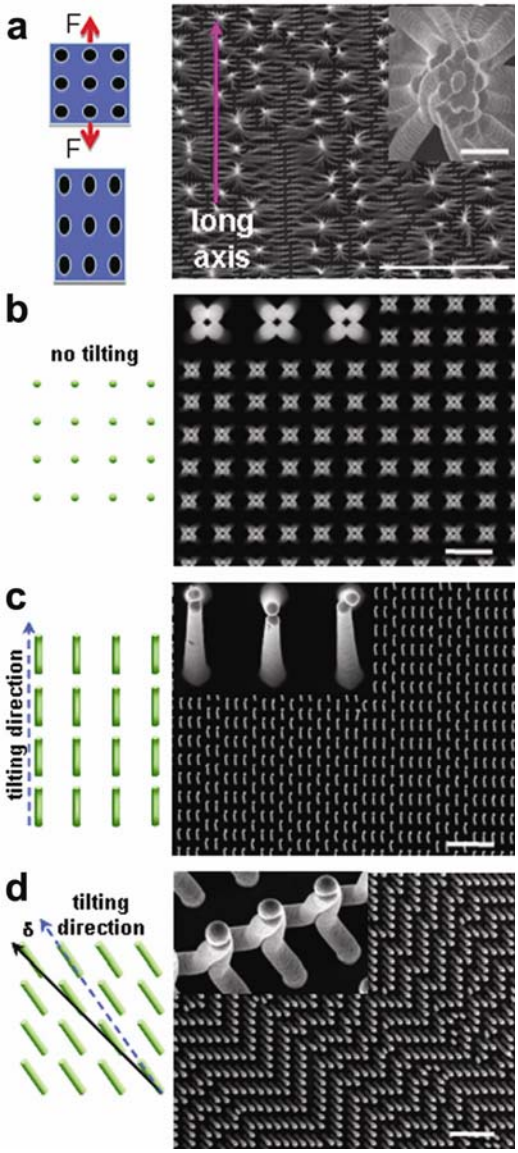


Figure 13. Effect of the anisotropy on the size and pattern of assembled clusters. Left column shows schematics (not drawn to scale) of the method used to fabricate various nanofiber arrays, and right column shows SEM images of the assemblies of corresponding nanofiber arrays. The insets show the high-magnification image of the corresponding SEM image. (a) Elliptical cross section nanofibers (h ~ 8 μm) arranged into a rectangular lattice assemble into anisotropic clusters elongated in the direction of the short axis if the ellipse (scale bar: 50 μm). The long axis indicates the direction in which the tensile force was applied. The inset shows the elliptical cross section of the fibers (scale bar: 1 μm). (b) Square array of cylindrical nanofibers oriented perpendicular to the surface assemble into a regular array of tetramers. (c) Fibers tilted along a lattice direction form a regular array of achiral dimers instead of tetramers. (d) Fibers tilted slightly off a diagonal lattice direction form chiral dimers with a uniform twisting direction.

Scale bars: 10 μm. Reprinted with permission from ref. 49. Copyright 2010 American Chemical Society.

## 3.5. Effects of elastic modulus of fibers on the size and shape of the assembly

In addition to changing the diameter of the fibers or symmetry of the array, we studied the effect of the elasticity by varying the elastic modulus of the material (Figure 11e,f). To systematically change the modulus of the fibers, two approaches were used: (i) adding the softener to the original polymer to decrease the stiffness of the fibers (Figure 11e), and (ii) mixing the polymer with silica nanoparticles to increase the stiffness of the fibers (Figure 11f). Note that while the former approach may also change the adhesive properties of the system, the latter would primarily affect the elastic modulus.

Changing the modulus showed a trend similar to changing the diameter, that is, appearance of chirality at intermediate modulus values, disordered achiral structures at a low modulus, and ordered achiral structures at a high modulus. The size of the assembly decreased with increasing modulus, as shown in the representative SEM images (Figure 14a-c), and in the statistical analysis (Figure 14d) for the moduli tested (E ~ 400 MPa, 600 MPa, 1 GPa, 1.6 GPa, and 2.4 GPa). From the analysis, the number of fibers per assembly is inversely proportional to the

modulus. In addition, when either modulus or diameter increases, the observed range of the assembly sizes decreases, consistent with a previous study on aggregation of bundles of wet hair, showing that the range is proportional to the maximum assembly size[74].

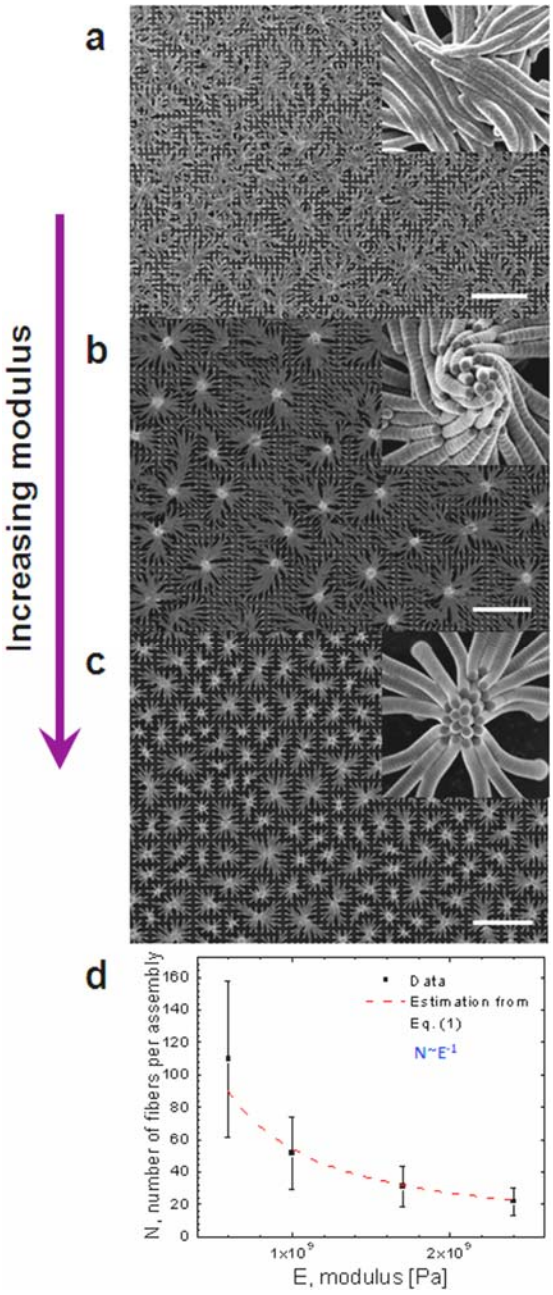


Figure 14. Effect of the fiber modulus on the size and pattern of assembled clusters. (a-c) SEM images of assembly of fiber array with different moduli (E): (a) E~400 MPa, (b) E~1 GPa, (c)

E~2.4 GPa. The diameter and the length of the fibers were fixed to 250 nm and 8 μm, respectively. The scale bars are 20 μm. The insets show high magnification images of the assemblies, which were used to check the onset of the chirality for each condition. (d) Plot of the number of fibers per assembly as a function of the modulus for fixed diameter and length of the fiber. The fitting shows 1/E dependence. Reprinted with permission from ref. 49. Copyright 2010 American Chemical Society.

## 3.6. Effects of adhesion and wetting properties of fibers on the size and shape of the assembly

Compared to the effects of elastic and capillary force terms, the effect of changing the adhesion force term has received little attention. We varied the adhesion of the fibers by using plasma treatment of the polymeric samples to activate reactive surface functional groups (Figure 11g)[75]. Though we do not have quantitative values for the resulting adhesion between the fibers, we expect that adhesion increases with plasma treatment time, as assessed by a qualitative comparison of forces required to slide two fibrous surfaces facing each other after making contacts. We observed that as the plasma treatment time increased, the chirality disappeared in the samples that showed substantial twisting when untreated. The assembled fibers then zipped parallelly instead of twisting helically, and the size of the clusters decreased as shown in Figure 15. This decrease in the size of the assemblies is somewhat counterintuitive since, in addition to increasing adhesion, plasma treatment decreases the diameter of the fibers and is therefore expected to increase the cluster size, if purely elastocapillarity arguments (equation (1)) are used

(Figure 15d). However, if plasma treatment increases the adhesion sufficiently, this more than makes up for the decrease in the diameter.

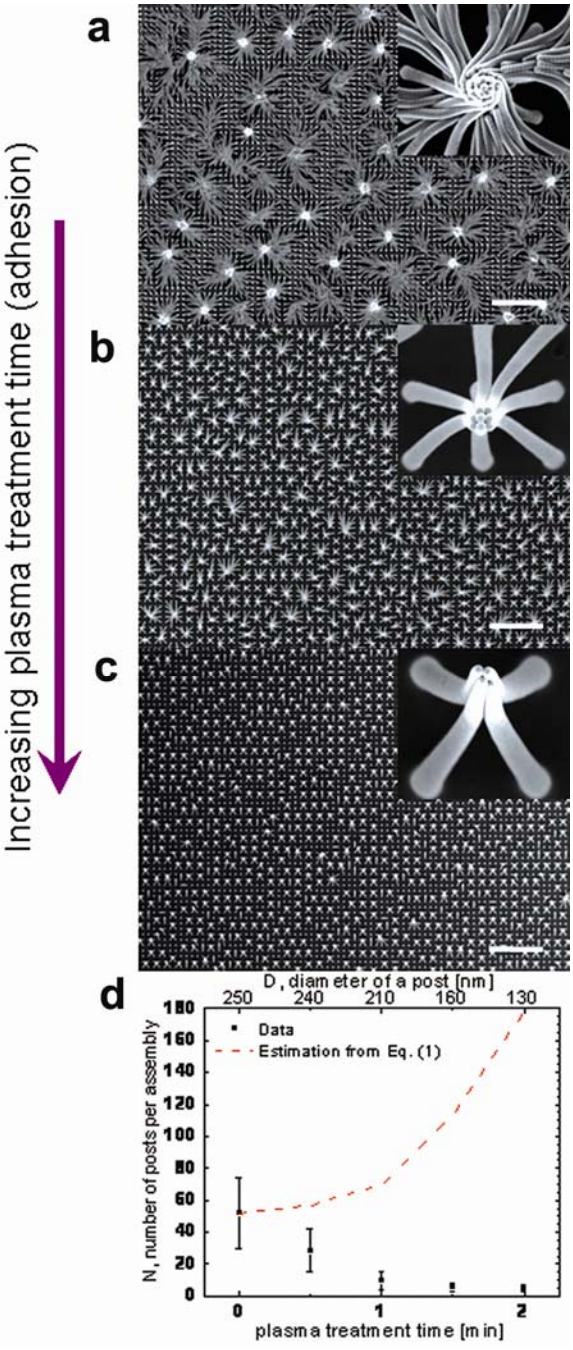


Figure 15. Effect of the plasma treatment on the size and pattern of assembled clusters. (a-c) SEM images of assembly of fiber arrays with different plasma treatment time. The plasma treatment increases adhesion as well as decreases the diameter of the nanofibers. (a) No plasma

treatment (control); (b) 1 min plasma treatment; (c) 2 min plasma treatment. The modulus and the height of the fibers were fixed at 1 GPa and 8 μm, respectively. The scale bars are 20 μm. The insets show the high-magnification images used for determining the shape of individual clusters. (d) Plot of the number of fibers per assembly as a function of plasma treatment time. Because the plasma treatment changes the adhesion and the diameter of the fibers at the same time, the corresponding diameters are shown on the top axis of the graph for a given plasma treatment time. Note that the number of fibers per assembly decreases as the plasma treatment time increases even though the diameter of the fibers decreases. Reprinted with permission from ref. 49. Copyright 2010 American Chemical Society.

It is possible that the plasma treatment may also change the capillary force by increasing surface wetting. However, since the contact angle of ethanol on the as-fabricated nanofiber array is already lower than 10°, its effect on the capillary force is negligible. In contrast, the effects of silanes of different critical surface tension values (Figure 11h) do change the wetting properties substantially; as the surface tension decreases below a critical value, the chirality of the assembly disappears, and its size is significantly reduced (Figure 16).

The surface properties of the fibers were varied by functionalizing the fiber surface with silanes of known critical surface tension values. In general, if the surface tension of a liquid is above the critical surface tension of the solid, the liquid does not fully wet the solid. Silanes with different critical surface tension values (12 mN/m for Heptadecafluoro-1,1,2,2-Tetrahydrodecyl Trichlorosilane and 34 mN/m for p-Tolyltrichlorosilane) were deposited onto the polymer fibers having a fixed modulus ($E$ ~ 1 GPa) and geometry (diameter ~ 250 nm, height ~ 8 μm, pitch ~ 2 μm) and the assembly patterns were compared with untreated epoxy ($\gamma_{critical}$ ~ 46 mN/m)

nanofibers as a control sample. Because the surface tension of ethanol is 22.3 mN/m at room temperature, the ethanol will partially wet the surface treated with Heptadecafluoro-1,1,2,2-Tetrahydrodecyl Trichlorosilane, whereas it will fully wet the surface functionalized with p-Tolyltrichlorosilane or a bare epoxy surface. Consistent with this expectation, we observed that the contact angle of an ethanol drop on a flat epoxy surface functionalized with Heptadecafluoro-1,1,2,2-Tetrahydrodecyl Trichlorosilane is 40.2±2.9° and for the surface functionalized with p-Tolyltrichlorosilane the contact angle is below the detection limit of our setup (the minimum measurable angle ~ 5°). Thus, silane treatments change the capillary force acting on the system. Indeed, as the critical surface tension value decreased, the nanofibers assembled by making contacts only around the tips of the fibers (insets of Figure 16a, b) instead of forming chiral assemblies by twisting of fibers as in the control sample (Figure 16c) and the size of the assembly is significantly reduced, as shown in Figure 16. In addition, the fibers with a silane of the lowest critical surface tension sometimes stand unclustered without forming any assembly, as shown in Figure 16a, because the ethanol only partially wets the surface. However, there is one important factor to consider: when the nanofiber is treated with different kinds of silanes, there is a chance that it can also change the adhesion of the surface and we do not know the quantitative contribution of wetting property change vs. adhesion property change in this case.

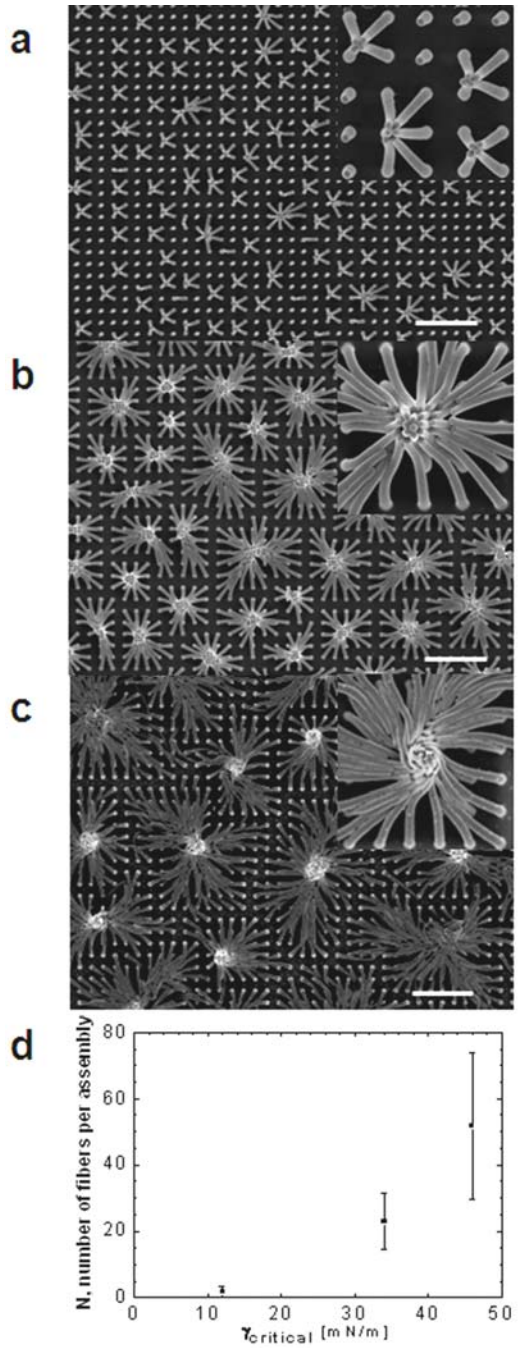


Figure 16. Effect of the wetting property on the size and pattern of assembled clusters. The SEM images of the assembly of fibers with different critical surface tension: (a) epoxy fibers with a silane of $\gamma_{critical}$ = 12 mN/m. (b) epoxy fibers functionalized with a silane of $\gamma_{critical}$ = 34 mN/m, (c) bare epoxy fibers ($\gamma_{critical}$ = 46 mN/m). The modulus, diameter and the height of the nanofibers were fixed at 1 GPa, 250 nm and 8 μm, respectively, The inset shows the high magnification images of the assemblies. The scale bars are 10 μm. Reprinted with permission from ref. 49. Copyright 2010 American Chemical Society.

The sidewall of the nanofibers has different degrees of corrugation due to the scalloping arising from the Bosch fabrication process. The corrugation (or scalloping) can result in differences in meniscus movement compared with a flat surface as illustrated in Figure 17a[41]. Moreover, it can change the contact area between two fibers that affects adhesion. We studied the effect of corrugation by using an epoxy nanofiber sample that has corrugation only at the bottom half (silicon master #3 described in the section 3.2). Interestingly, the fibers assembled with flat parts zipped together while the corrugated half was not assembled in most cases. This result suggests another way of changing the surface adhesion property by controlling the surface morphology of the nanofiber walls.

Finally, increasing the adhesion by using a smoother surface, which has a larger contact area (Figure 17), causes structures to assemble like a zipper with no chirality. Thus, we see that interfiber adhesion has the ability to control the chirality, shape, and size of the final assembly after contacts are made.

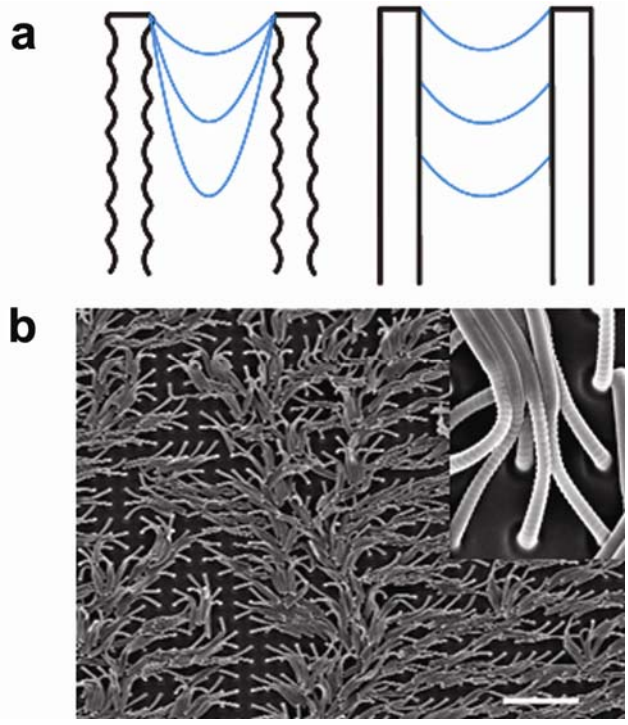


Figure 17. Effect of the wall corrugation on the size and pattern of assembled clusters. (a) Schematic diagrams depicting meniscus movement on the scalloped (left) and versus flat (right) nanofibers. (b) The SEM image of assemblies of epoxy nanofibers that had flat walls at the top half and scalloped at the bottom half. The modulus, diameter and the height of the fibers were fixed at 1 GPa, 250 nm and 8 μm, respectively, The inset shows the high magnification images of the assemblies. The scale bars are 10 μm. Reprinted with permission from ref. 49. Copyright 2010 American Chemical Society.

## 3.7. Proposed model – adhesion mediated elastocapillary interaction

While evaporation-induced self-assembly has been studied and modeled as the result of the competition between capillary and elastic forces[21,22,68-70], our data demonstrate that interfiber adhesion is equally important to determining the final assembly. Our instantaneous and continuous real-time imaging show that assembly is, in fact, biphasic: fibers assemble

hierarchically, as reported in Chapter 2, but can subsequently undergo hierarchical disassembly as outlined in Figure 18a. We observe this second phase most distinctly when the fiber stiffness is relatively high (Figure 12c); a large assembly initially forms under capillary force, but after the liquid dries, it breaks apart into smaller clusters equal to its immediate precursors. Since adhesion alone balances the elastic deformation in the dry system, the most straightforward conclusion is that adhesion is insufficient to maintain the last stage of assembly. Thus, while the balance between capillarity and elasticity determines the *maximum* size the system can achieve[14,69,70,74,76], the balance between adhesion and elasticity determines how many hierarchical stages will be preserved in the final structure[2]. The fact that disassembly follows a reverse hierarchical path, rather than one-step dissociation, suggests that the assembly size is specified by the balance between capillarity, elasticity, and adhesion.

The chirality and shape of the assembly are also strikingly dependent on the delicate balance between adhesion, elasticity, and capillarity. Fibers initially contact each other at their tips, and chirality arises when the contact point slips and the fibers twist around each other (Figure 18b). We have shown that large fiber stiffness can prevent chirality (Figure 12c, Figure 14c), most likely by preventing the fibers from twisting[2], while assemblies are chiral only when the fibers have an intermediate bending modulus (Figure 14b) or diameter (Figure 12b). Similarly, adhesion plays an important role in determining assembly shape and chirality:

significantly increasing surface adhesion but not stiffness produces achiral structures in which fibers “zip” together along their length rather than twist (Figure 15 and Figure 18b). This result suggests that, first, chirality can only arise if the adhesion force is low enough to allow the initial slip, and second, fibers can assemble into an alternate shape (e.g., zipped structures) that has a large fraction of connected surface area but remains achiral if the adhesion is high enough both to prevent slippage and to stabilize extra bending.

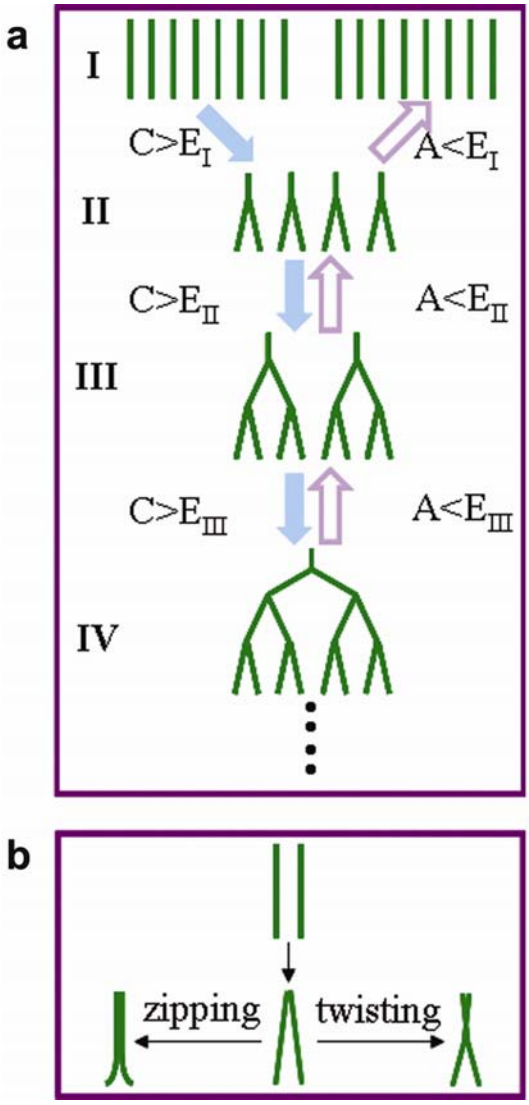


Figure 18. Schematic diagrams depicting the mechanisms of the assembly process. (a) Possible routes of the assembly and disassembly processes that determine the final pattern. C and A indicate the capillary force and the adhesion force, respectively. E is the elastic force, and the subscripts I, II, III, and IV indicate the hierarchy of the assembly. Note that while the interplay between the elastic and capillary force determines the maximum size the assembly can reach while wet, the adhesion force determines stability of the formed clusters and the size and shape of the final product. (b) Different shapes of the assembled clusters. The nanofibers first attached at the tips and, depending on the adhesion force between the fibers, can either undergo a slippage and chiral rearrangement leading to twisted clusters for low adhesion or zip down the nanofibers for high adhesion values. Reprinted with permission from ref. 49. Copyright 2010 American Chemical Society.

Our results further suggest that the effects of the various parameters on size may themselves be mediated by shape and/or chirality of the forming clusters. Most notably, increasing surface adhesion leads not to larger assemblies that can be sustained by the high adhesion but instead to progressively smaller assemblies (Figure 15). The zippered shape of the four-fiber assembly observed at high adhesion (Figure 15c) may effectively behave as a single fiber with a larger diameter and a shorter height, with less flexibility than if the fibers were connected only at their tips, possibly analogous to "collaborative stiffening" described for wet hair bundles[77]. The specific differences between zipped and twisted structures that might make the former less likely to form larger assemblies are unknown, but include differences in effective height or diameter, total contact or exposed area, symmetry, or a more complex liquid-solid contact line, any of which would change the propensity for capillary-induced bending and stability.

For a more quantitative understanding, we have compared our experimental results for the changes in diameter, modulus, adhesion, and wetting of the fibers with theoretical predictions based on the literature[14,69] using equation (1) for various conditions (Figure 19). The experimentally measured average assembly size is consistent with a linear scaling associated with varying modulus and diameter although of the prefactor of 952 is 3-fold higher than the value of 258 reported by Chandra *et al.* [69]. Note that the previous work assumed that the final equilibrium state and the average assembly size is determined by energy minimization that

accounts only for elastic bending energy and capillarity energy[69]. However, as we have shown (Figure 15 and Figure 19), plasma treatment and surface chemistry data point strongly to the importance of adhesion, which has not been considered earlier, and these changes can result in a significant deviation from the expected assembly size based only on elastocapillarity effects.

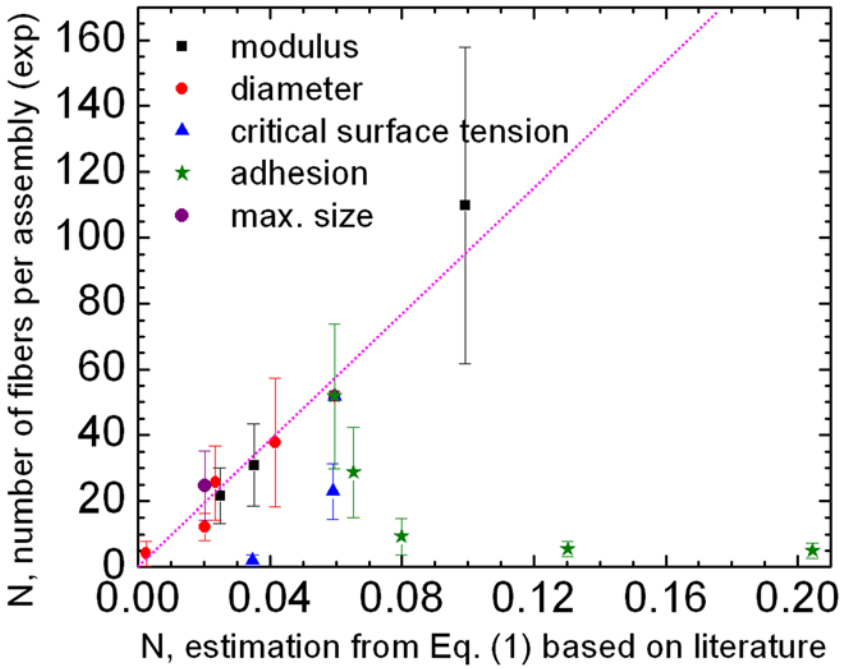


Figure 19. Comparison of the experimental data for the number of fibers per assembly vs. theoretical estimation based on Equation (1) for the modulus, diameter, critical surface tension, and adhesion change. The data point for the maximum size is from the data before complete drying shown in Figure 12d. The slope of the dotted line is 952. Reprinted with permission from ref. 49. Copyright 2010 American Chemical Society.

More generally, the existing static models fail to reflect the dynamic aspect of the process associated with the hierarchical nature of assembly and disassembly (Figure 18a). If the collective forces driving slippage or chiral/achiral increases in surface contact are strong enough relative to those driving higher-level association, the strong local interactions due to adhesion

may effectively modify parameters such as diameter, height, exposed area, or symmetry as discussed. For example, the self-assembly of fibers[2] can lead to the collaborative stiffening and adhesion of the structures[77] and thus a complex evolution of the shape of self-assembled clusters, so that a global minimum energy state[78] may never be reached. Ultimately, any comprehensive model for capillary-induced assembly must account for the dynamic interplay between capillarity, elasticity, and adhesion on different length scales.

Finally, our study shows that manipulating the properties of the building blocks of self-assembly, including geometry, anisotropy, stiffness, and surface chemistry of assembling nanofibers, provides a simple way of fabricating complex hierarchical nanostructures, which can be tailored to have desired tunable functions for applications such as trapping and releasing of nano- and microparticles, controlling wetting properties by changing the surface morphology[79], adhesives based on mechanical interlocking[2,80], and controlling optical properties by structural effects[69,81], to name a few.

## 3.8. Applications – reversible assembly and trapping and release of microparticles

Based on our understanding of the adhesion-mediated elastocapillary assembly process, we

can utilize the assembly process for reversible control of the surface configuration. For example, we can trap microparticles if we add them in an evaporating liquid because fibers like to maximize adhesion contacts by mechanical interlocking of particles as shown in Figure 10 and Figure 20a. Then, how can we release the particles? We can also release particles by reducing adhesion between fibers and particles using a different solvent. For example, if we use sulfonated particles, the particles can be trapped when we use ethanol as an evaporating liquid while they can be released if we use water as a solvent (Figure 20b). This reversible trapping and releasing of particles could be useful for applications such as drug delivery. Besides spherical particles, the assembly process can be also used for capturing objects with different geometries such as a high aspect-ratio rod as shown in Figure 20c.

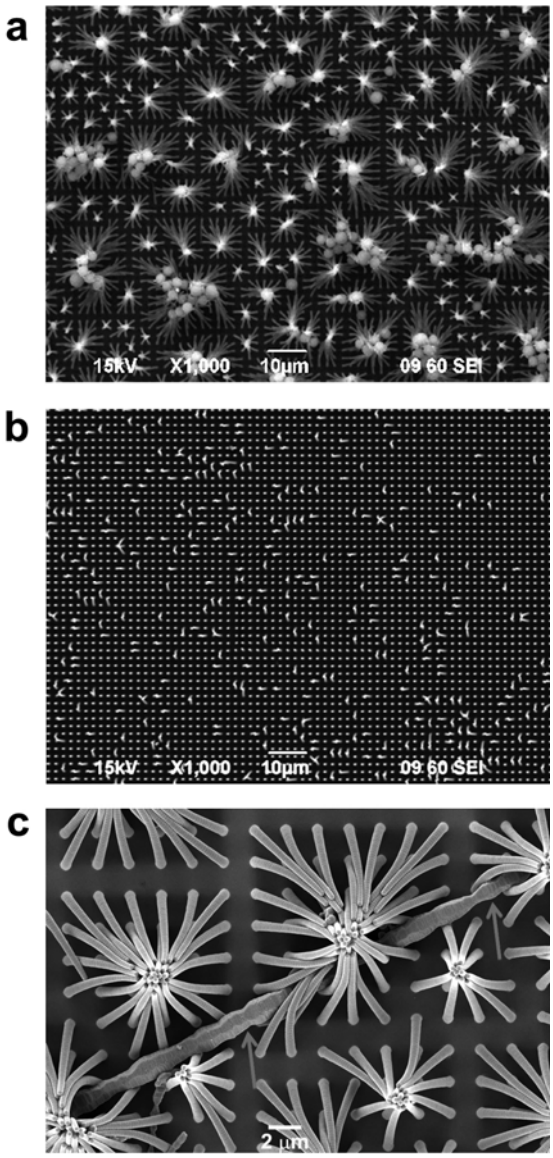


Figure 20. (a) An SEM image of particle trapping by self-assembly. 2.5 μm polystyrene particles were added to ethanol for the trapping experiment. (b) An SEM image of particle release by putting the sample (a) into water and letting it evaporate. (c) An SEM image of trapping a high aspect-ratio rod by self-assembly. An 1 μm diameter silicon carbide rod was added to ethanol for the trapping experiment.

## 3.9. Summary

Using a model self-assembly system with easily tunable parameters, we have demonstrated that varying the mechanical and/or surface properties of the nanofibers provides us with simple routes for fabricating complex structures with control of size, chirality, and anisotropy by capillary-induced self-organization. Our results also showed that it would be necessary to consider adhesion as well as the kinetics of assembly for a more comprehensive understanding and prediction of assembly patterns. By varying the geometry, stiffness, and chemistry of the assembling nanofibers, we observe that chirality can be generated within a small window for each parameter, even though the systems do not involve either chiral building blocks or a chiral environment. Moreover, the use of anisotropic building blocks expands our toolbox for controlling the size, geometry, and chirality of the assembled clusters. This study provides a broader perspective of how a variety of features contribute collectively to capillary-induced self-assembly and demonstrates many options for fine-tuning the assembly to generate diverse structures.

# Chapter 4 Moire Patterns in Liquids

In chapter 4, we will first discuss the origin of random assembly behaviors and explore dynamic feedback between the solid and the liquid as a way of controlling the long-range order of the assembly. This chapter is based on our published paper (ref. 1). The content is used with permission from American Physical Society.

## 4.1. Introduction

Pattern formation has been intensely studied across a wide range of length scales both for the insight it provides into the principles of self-organization and for its potential applications in areas such as data storage[82], sensing[83], and wetting[84]. Among many methods for pattern formation, evaporation-induced patterning has received particular attention[85-87] as a bottom-up, low energy approach to creating patterns across multiple length scales, as well as for the extremely rich spread of fundamental questions it opens. For example, the ‘‘coffee ring’’ effect[88] has been shown to generate a variety of ringed and banded colloidal deposits via evaporation-induced fluid flows that carry particles to the periphery of a droplet.

Beyond simple rings and bands, this strategy has been used to produce complex patterned films by placing a shadow mask over the droplet to create regions of free and hindered

evaporation[89] or by confining the meniscus to control the ‘‘stick and slip’’ motion of capillary flow[90]. In addition to flow-based mechanisms, the capillary forces generated by the menisci between individual particles have attracted interest for their ability to assemble nanofibers[2,49,70,91] and other building blocks[60,92] into intricately patterned structures. Although, in each case, the process is inherently mutual—the solid pins the liquid as the liquid moves the solid—the behavior and potential manipulation of the system have rarely been analyzed from this perspective.

## 4.2. Absence of long-range order - issue of random nucleation and propagation of assembly

While capillary forces can induce local interaction and assembly of individual particles into patterned clusters, in practice, the uniformity of this process over a large area can be difficult to control, and macroscopically ordered, periodic structures assembled by the capillary forces have not been reported. This issue is clearly observed for an array of surface-anchored fibers assembling in an evaporating liquid. As the liquid evaporates, menisci form between the tips of neighboring fibers and generate capillary forces that drive bending and assembly. If the array has uniform spacing, the forces on a given fiber will theoretically be the same in all directions, but in reality, random imperfections and/or instabilities will break the symmetry and cause the fiber to

bend in one direction or another[2] (Figure 21a). This process produces self-assembled bundles whose average size and shape are controlled by the geometric, elastic, and adhesive properties of the fibers, but even a highly periodic array (Figure 21b) produces no long-range order in the symmetry and placement of these bundles, only clusters distributed randomly on the surface (Figure 21c). To program large-scale order, there have been many efforts to manipulate the geometries (shape, pitch, etc.)[49,60,67] and surface properties of the building blocks[49,63], such that their chemical or structural anisotropy would bias the entire system to assemble into a desired pattern. These approaches, however, have the disadvantage of requiring the building blocks to be specifically designed for each new pattern. An alternative approach would be to place a patterned mask above the array of assembling fibers. As has been shown for colloidal film patterning[89], the mask would impose long-range order on the array by creating regions with varying rates of evaporation. While this method would allow various patterns to be formed from the same array of fibers, each pattern would still require a specially designed mask.

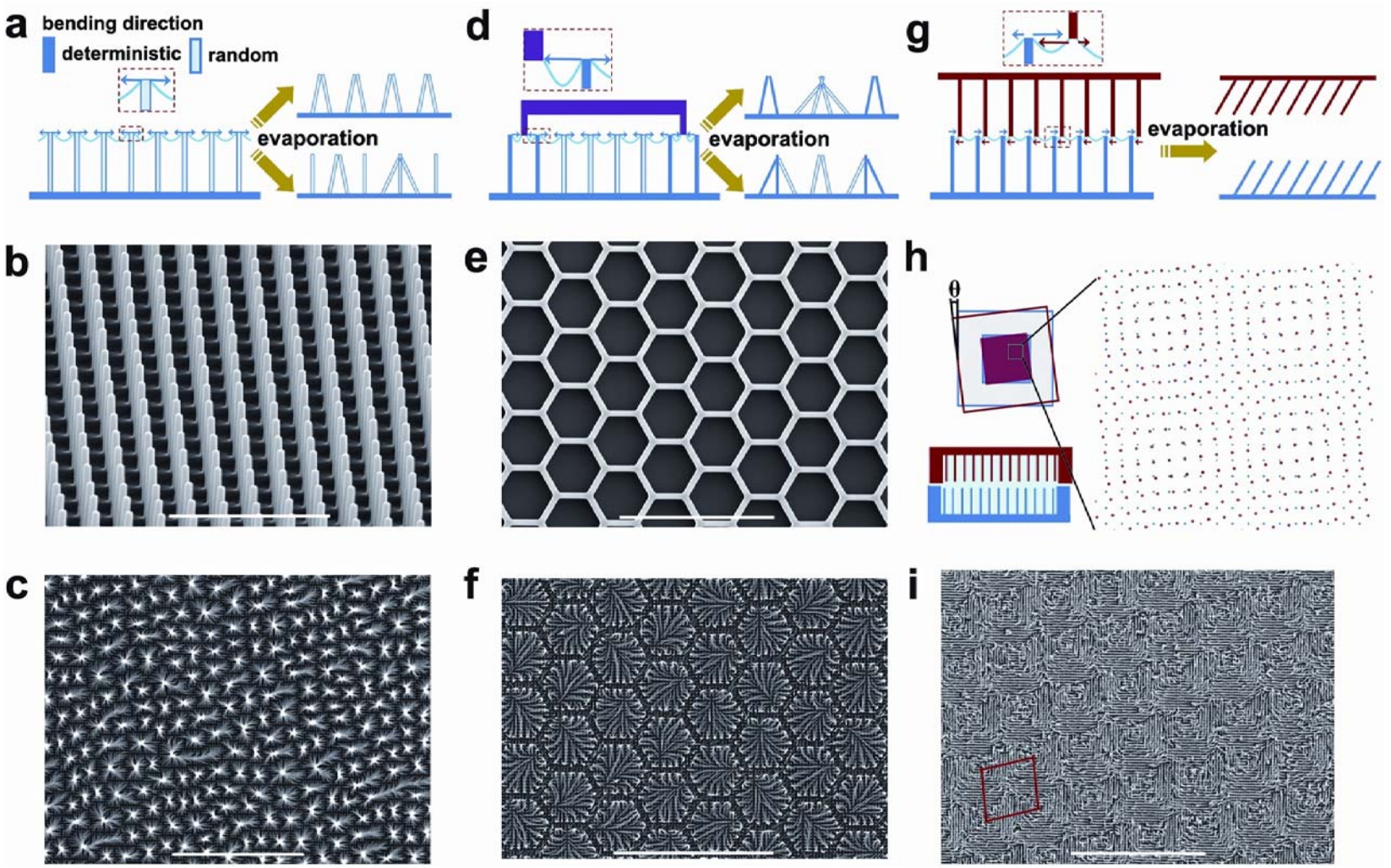
a
bending direction
deterministic
random
evaporation
d
evaporation
g
evaporation
b
e
h
θ
c
f
i

Figure 21. Pattern formation in fiber arrays upon liquid evaporation. (a)–(c) Maskless process: (a) Schematics of the fiber arrays (side view) before (left) and after (right) evaporative assembly. Dark-colored fibers have deterministic bending directions, while light-colored fibers have random bending directions. Curved blue lines indicate menisci formed between fibers. Arrows indicate the direction of the capillary forces, with relative force magnitudes indicated by length. Note that the final assemblies shown represent only a sampling of the possible patterns that can form, since all the bending directions are random. (b) SEM image of the periodic nanofiber array used in all the experiments. (c) SEM image of the assembled fiber array following evaporation in the absence of a mask. Note the absence of any long-range order. (d)–(f) Evaporation under a superimposed mask with feature spacing larger than that of the array: (d) Schematic of the pattern formation; the wetting liquid fills the space between the array and the mask. (e) SEM image of an exemplary honeycomb mask. (f) SEM image of fibers shown in (b) assembled under a honeycomb mask. Note the long-range symmetry determined by the mask, with random patterns within each assembled cell. (g)–(i) Masked evaporation and pattern formation in the sandwich system composed of two identical arrays of fibers: (g) Schematic of the process depicting fully deterministic bending directions in such a system. (h) (Left) Schematic of two superimposed fiber arrays (top and side views) corresponding to the case shown in (g). θ is the mismatch angle between the top and bottom lattice axes. (Right) Schematic of the individual positions of fibers (top view). Red and blue dots correspond to fibers from top and bottom samples, respectively. Note the appearance of the Moire pattern. (i) SEM image showing the pattern generated from the two identical superimposed arrays after evaporation and remaining as a permanent imprint of the Moire interference on the substrates after separation. The red outline shows a unit cell of the generated pattern. The scale bar is 10 μm for (b) and 100 μm for (c), (e), (f), and (i). Reprinted from ref. 1 with permission from American Physical Society.

## 4.3. Long-range order formed using a large-scale shadow mask

Here, we explore a conceptually different approach to masked evaporation that allows a variety of complex patterns to be generated from the same pair of substrate and mask. Instead of using the mask to create a patterned ‘‘shadow’’ over the array, we place the mask directly on top

of the array such that its raised features come face-to-face with the fibers. As a result, when a liquid is placed in the middle, menisci form between the fiber tips and the mask features. The mask and substrate therefore collectively structure the evaporating liquid at the interface and pattern the menisci that drive bending. To illustrate how this approach leads to long-range order, we analyze the capillary-induced movement of fibers under the patterned mask. When the mask periodicity is larger than that of the underlying array, the fibers closest to the raised features will deterministically bend toward the mask feature defining the overall symmetry of the imprint pattern, but fibers located under the large recessed regions of the mask will still bend randomly (Figure 21d). The assembly pattern will show long-range order that corresponds to the symmetry of the mask, with random variations within each assembled cell, as demonstrated in Figure 21e and Figure 21f. As the mask periodicity approaches that of the array, more of the fibers will be adjacent to mask features and will bend in deterministic directions, and fewer fibers will bend randomly.

## 4.4. Long- and short-range order using a mask with a pitch comparable with the fibrous array

### 4.4.1. Deterministic movement of fiber arrays by patterning of menisci

Of particular interest is the situation in which the mask periodicity is the same as that of the

array (Figure 21g). In this case, every fiber will form a meniscus with an adjacent mask feature. Because of the small separation between mask and substrate, each fiber will now be closer to a mask feature than to its neighboring fibers (Figure 21g). Since the capillary force is inversely proportional to the spacing[93], the menisci formed between the fibers and mask features will determine the direction of each fiber's movement. All fibers will therefore bend deterministically, making it possible to create a completely controlled collapse pattern. In fact, the mask need not even be different from the substrate—a second copy of the same fiber array can serve as a ''mask'' with perfect one-to-one feature pairing.

### 4.4.2. Moire effect and control of periodicity and chirality

Moreover, this system has all the characteristics of one that gives rise to the Moire effect, whereby two superimposed motifs create unique interference patterns depending on how they are mismatched or placed relative to each other (Figure 21h). The phenomenon is most commonly observed optically due to the modified behavior of light within the space defined by the new collective pattern. In such cases, there is no feedback: the original motifs are not influenced by the patterned behavior of light, and the Moire pattern disappears when the original motifs are separated. However, for arrays of fibers with a layer of liquid between them, the liquid will not only be patterned through meniscus pinning but will impose force back on both arrays as it

evaporates. The mechanical force will therefore translate the collective pattern from the liquid back to the two solid surfaces, and, if the stiffness of the fibers is below the critical value (see section 4.4.3. for force estimation), fibers on both the top and bottom surfaces will undergo directional bending and collapse. As a result, identical patterns can be preserved on both the top and bottom samples after separation. Since Moire patterns are highly and predictably sensitive to the rotational angle between the superimposed motifs[94], this would imply that, for our system as well, a wide assortment of patterns can be generated from the same starting components.

To test the potential of Moire interference as a way to generate long-range order and tunable patterns, we used two identical arrays of regularly spaced surface-anchored polymeric nanofibers placed face-to-face with a droplet of ethanol sandwiched between them (Figure 21h). The arrays consisted of fibers with a radius of 125 nm, a height of 8 μm, and a pitch of 2 μm and were made of epoxy resin (UVO 114 from Epoxy Technology, modulus 1 GPa) following the procedure described in ref. 5. Upon evaporation, a single control array (Figure 21b) shows no long-range order, preferential bending direction, or periodicity other than the original spacing between the fibers (Figure 21c). In contrast, the superposition of two such substrates creates a complex, periodic collapse pattern across the scale of the entire sample on both the top and bottom surfaces (Figure 21i).

As for conventional Moire phenomena, the periodicity can be varied by small changes in the

rotation angle between the superimposed fiber arrays. We have measured the period of the superlattice obtained with different mismatch angles, as shown in Figure 22, and the experimental results match well with the theoretical prediction based on optical interference[95]. However, unlike optical Moire patterns, which disappear when the superimposed layers are separated, here the pattern remains preserved in both the top and bottom arrays after they are separated. Although the capillary forces that initially drive pattern formation disappear once the liquid dries, the patterns can be stabilized by plastic deformation of fibers as well as by attractive (e.g., van der Waals) interactions among the deformed fibers or between the fibers and the substrate base.

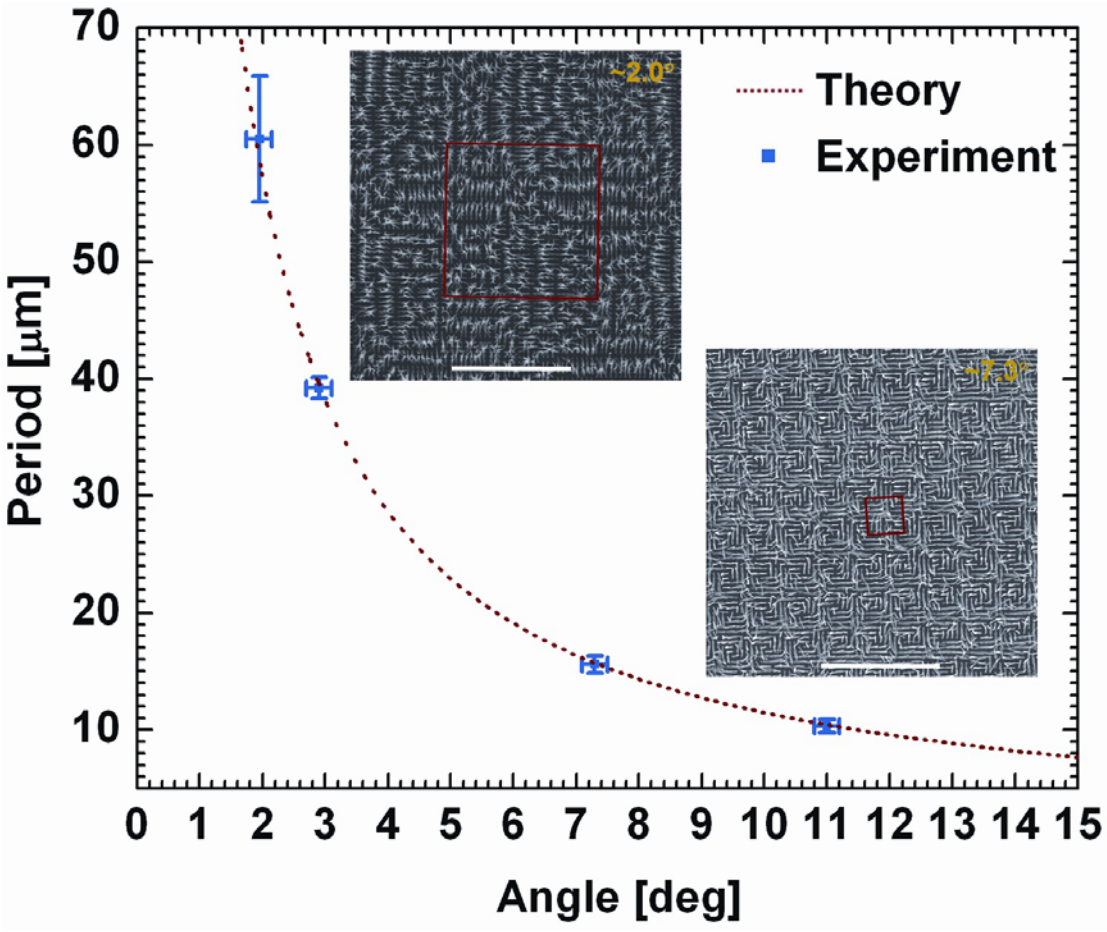


Figure 22. Plot of the period of the pattern vs. the mismatch angle. The dotted line is based on theory[95] and shows good agreement with the experimental results. Error bars indicate standard deviations from at least 5 independent measurements. Representative SEM images of the assembled patterns are shown with their corresponding data points; the number at the upper right indicates the mismatch angle. The red lines indicate unit cells of the generated patterns. The scale bar is 50 μm. Reprinted from ref. 1 with permission from American Physical Society.

Meniscus ‘‘lithography’’ by this method also produces patterns with single chirality, which are not observed in either conventional Moire phenomena or traditional evaporation-induced self-assembly. Starting from achiral, cylindrical fibers positioned in a centrosymmetric square

array, chirality is introduced as the fibers all tilt either clock- or counterclockwise toward their top neighbors and break the rotational symmetry of the array. This tilting and the resulting collapse occur in a spiral manner (Figure 23a). The top and bottom samples always have the same chirality as each other and generate two identical collapse patterns, as schematically illustrated in Figure 23b. The specific handedness of the chirality can be controlled by the sign of the rotational angle between the two arrays. As shown in the schematic in Figure 23c and Figure 23d, for opposite rotation directions, the fibers have opposite preferential bending directions prescribed by the overlap of the two arrays, collectively resulting in an opposite handedness. Thus, by simply changing the sign of the rotation angle (Figure 23c and Figure 23d), we create patterns with opposite chirality. The handedness remains the same for any angle, as long as the rotation direction does not change.

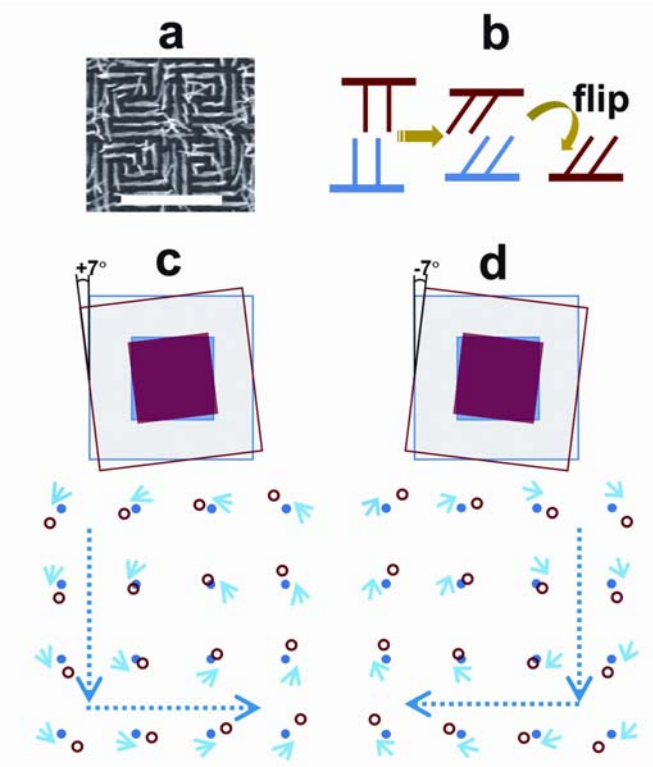


Figure 23. Appearance of chirality in fiber arrays assembled by meniscus lithography. (a) SEM image showing a spiral collapse pattern. The scale bar is 20 μm. (b) Schematic showing that the patterns formed on the top and bottom arrays have the same chirality. (c)-(d) Schematic of the array alignment (top views) and resulting fiber positions depending on the sign of the mismatch angle. A 7° mismatch angle was used as an example. Red hollow circles represent fibers from the top array, while blue solid circles correspond to those from the bottom array. Small arrows indicate the bending directions of the bottom fibers during evaporation, and the large arrows indicate the chirality of the generated patterns. Reprinted from ref. 1 with permission from American Physical Society.

### 4.4.3. Estimation of forces

In this process, both the mechanical (elastic modulus) and the geometric properties of the fiber array are important factors in the pattern formation. A necessary condition is that the capillary force must be strong enough to bend the fibers. Quantitatively, the capillary force ($F_c$) acting on a fiber can be estimated from the following expression[93],

$$F_c = \frac{\pi\gamma R^2 \cos^2\theta}{\sqrt{(x/2)^2 - R^2}} \qquad (2)$$

where $\gamma$ is the surface tension of the liquid, $R$ is the radius of the fiber, $\theta$ is the contact angle of the liquid, and $x$ is the pitch of the fiber array. In our system, $\gamma$ = 22.3 mN/m (ethanol), $R$ = $1.25\times10^{-7}$ m, $\cos\theta \sim 1$ and $x \leq 1\times10^{-6}$ m, so the capillary force is at least $F_c \sim 2.3$ nN for a fiber array with a center to center distance of 1 μm. The capillary force increases significantly as the distance between the top and bottom arrays decreases, becoming an order of magnitude higher when the distance is ~0.27 μm, as in Figure 24.

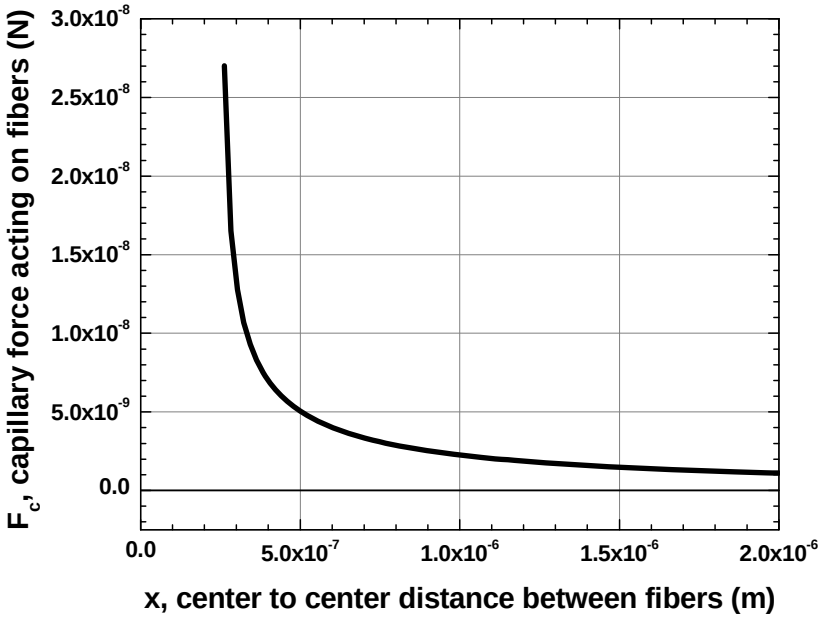


Figure 24. The estimated capillary force acting in the studied system as a function of the distance between fibers.

On the other hand, the elastic force that deflects the fiber with a displacement ($\delta$) of 0.5 μm

(half of the separation between two fibers) can be expressed as

$$F = \frac{3E\pi R^4 \delta}{h^3} = \frac{3\times(10^9\, N/m^2)\pi(1.25\times10^{-7}\, m)^4(0.5\times10^{-6}\, m)}{4(8\times10^{-6}\, m)^3} \sim 5.5\times10^{-10}\, N \qquad (3)$$

where $E$ is the modulus of the fiber, $R$ is the radius of the fiber, $\delta$ is the displacement and $h$ is the height of the fiber. Thus, it is clear that $F_c > F$ in our system, such that the bending of fibers can be induced by the capillary force. The elastic force formula is only approximate (valid only at the initial stage), since the deflection is large at later stages. But, as mentioned above, the capillary force also increases as the spacing between fibers decreases.

In our system, both the height of the fibers and the spacing between the fibers play a role in pattern formation, because increasing the fiber height decreases the effective bending stiffness and decreasing the fiber spacing increases the driving capillary force. In addition, the surface tension and wetting properties can also play a role because they affect the capillary force. For a simplified calculation, if we assume that the capillary force is on the order of 2 nN, our approach would not be applicable if the effective stiffness[5] (force required per unit of displacement) were larger than $4\times10^{-3}$ N/m. Based on the understanding above, we can choose a variety of materials and geometry for patterning the surface by meniscus lithography.

Moreover, while the capillary forces disappear after the liquid dries, there can be various possible mechanisms for preserving the pattern. As there is a large deformation of fibers, the material likely undergoes plastic deformation, resulting in freezing of the patterns. In addition,

attractive interactions (e.g. van der Waals force) between the fibers and the substrate would lead to further directional collapse and can also provide adhesion forces to preserve the pattern.

## 4.5. Real-time monitoring of evaporation and formation of patterns

In order to study the evolution of the pattern formation, we used bright-field microscopy to follow the process of self-assembly in real time as the solvent evaporates between the two superimposed arrays. Figure 25 shows snapshots of the drying process; the bright areas correspond to wet regions, and the dark regions are dry. On a macroscopic scale, as the solvent evaporates, the meniscus recedes from the periphery towards the center of the arrays, with random propagation and generation of pockets of accelerated evaporation due to local imperfections and/or instabilities (Figure 25). The microscopic movement of the meniscus, however, always follows the superlattice of the Moire pattern imposed by the superposition between the top and bottom fiber arrays. Therefore, a long-range order that corresponds to the Moire superlattice appears as the liquid evaporates, irrespective of the randomness of the evaporation front or the instability distribution. The periodicity of the wet region in the optical image matches with that of the patterns observed in an SEM image of the corresponding region after drying (Figure 25).

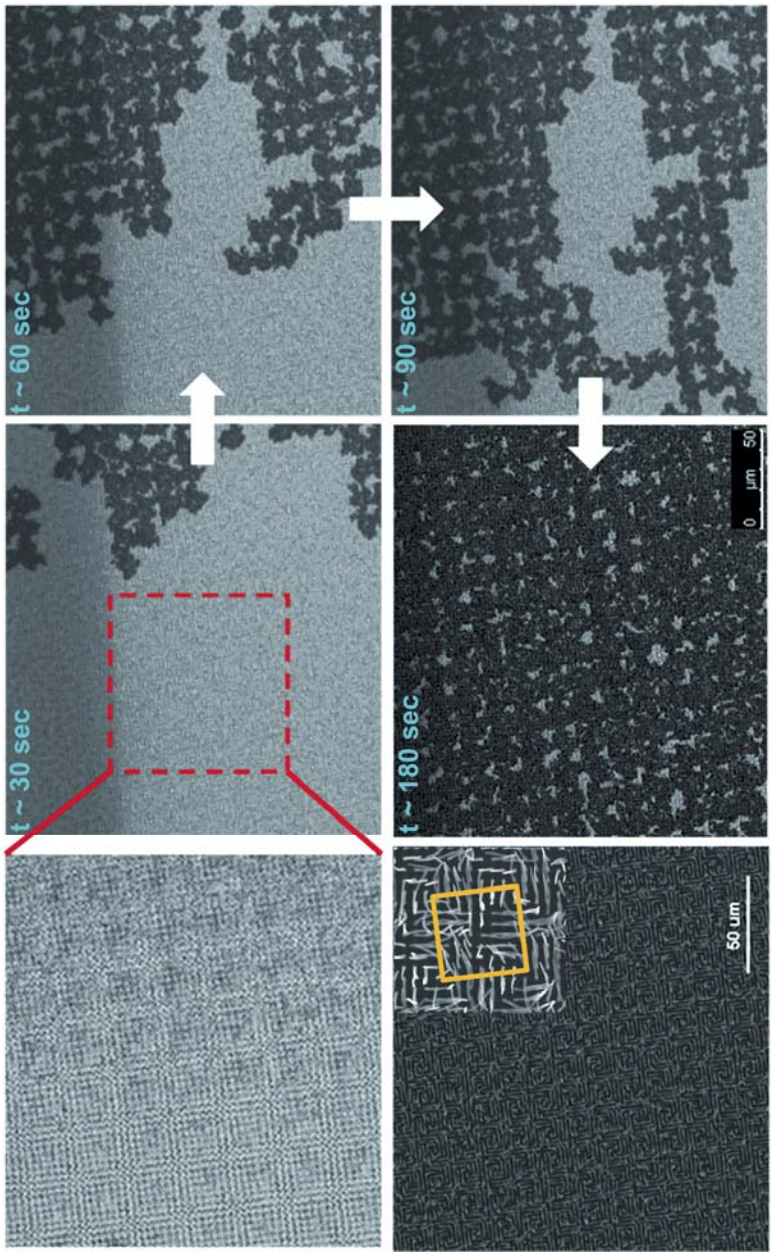


Figure 25. Bright-field snapshots of the drying process (first five panels, clockwise from the top left panel) and an SEM image of the resulting pattern (last panel). Dark regions are dry, and light regions are wet. Snapshots were focused at a height approximately corresponding to the fiber tips from the bottom array. The first panel shows the optical micrograph of the Moire interference pattern due to superposition of the top and bottom fiber arrays before drying. The inset in the SEM panel is a zoom-in of the pattern after evaporation, with the square showing a unit cell of the pattern. Reprinted from ref. 1 with permission from American Physical Society.

## 4.6. Summary

Our results demonstrate that a liquid sandwiched between two periodic surfaces is reshaped by Moire interference and, in turn, mechanically reconfigures the original surface features to create permanent imprints of the pattern. Patterning takes place via a dynamic feedback mechanism: in our system, the interference pattern arising from the two fiber arrays is read out by an intervening liquid, generating a set of patterned menisci that bend the fibers in predetermined directions upon evaporation. This work not only introduces the rich mathematical theory of Moire phenomena to evaporative and other forms of mechanical force-mediated patterning, but also reveals how a new principle, formation of chiral patterns from achiral starting motifs, can arise in the context of a feedback system. Patterning menisci based on these principles provides a simple, scalable approach, ‘‘meniscus lithography,’’ for fabricating a series of complex, long-range-ordered structures from the same starting components. Both periodicity and chirality are easily tuned by small changes in the mismatch angle. While top-down lithography by optical Moire interference has recently been explored[96,97], we show that Moire patterns can evolve spontaneously within a self-assembling system through the direct interplay between solid and liquid components, with no need for specialized optically sensitive materials. Besides two overlapping periodic arrays, this method can also be used to generate controlled assembly patterns from aperiodic structures such as the Glass pattern[98]. Moreover, the idea of

meniscus lithography can be extended to various methods of liquid patterning (e.g., using a surface acoustic wave).

# Chapter 5 Ordering of Assembly Patterns by Manipulating Movement of Evaporation Front

In chapter 5, we have examined the ordering of assembly patterns by investigating the effects of controlling the movement of evaporation front. We will first cover the mechanism of domain formation during assembly and study effects of manipulating movement of evaporation front as a way of mitigating the formation of multiple domains. Based on promising results, we will investigate the effect of the speed of movement and develop a model for the largest domain formation and more quantitative understanding of the phenomena. This chapter is based on our work that we prepare for publication (ref. 99).

## 5.1. Formation of domains during assembly

As mentioned in the previous chapter, the evaporation process tends to generate random nucleation and propagation due to presence of defects on a sample and nonuniformity of the evaporation process. When the first cluster is formed (nucleation of assembly), the assembly tends to propagate to neighboring fibers due to symmetry breaking in the capillary forces acting on the arrays as schematically shown in Figure 7a. Such process creates a “single crystal”

domain with clusters satisfying the crystal symmetry of the underlying fiber array. Because the nucleation tends to appear at random locations on a sample and the generated nuclei propagate to neighboring posts, the assembly tends to form multiple domains (see Figure 26), even though we use well-ordered square array of posts which tend to form tetrameric clusters.

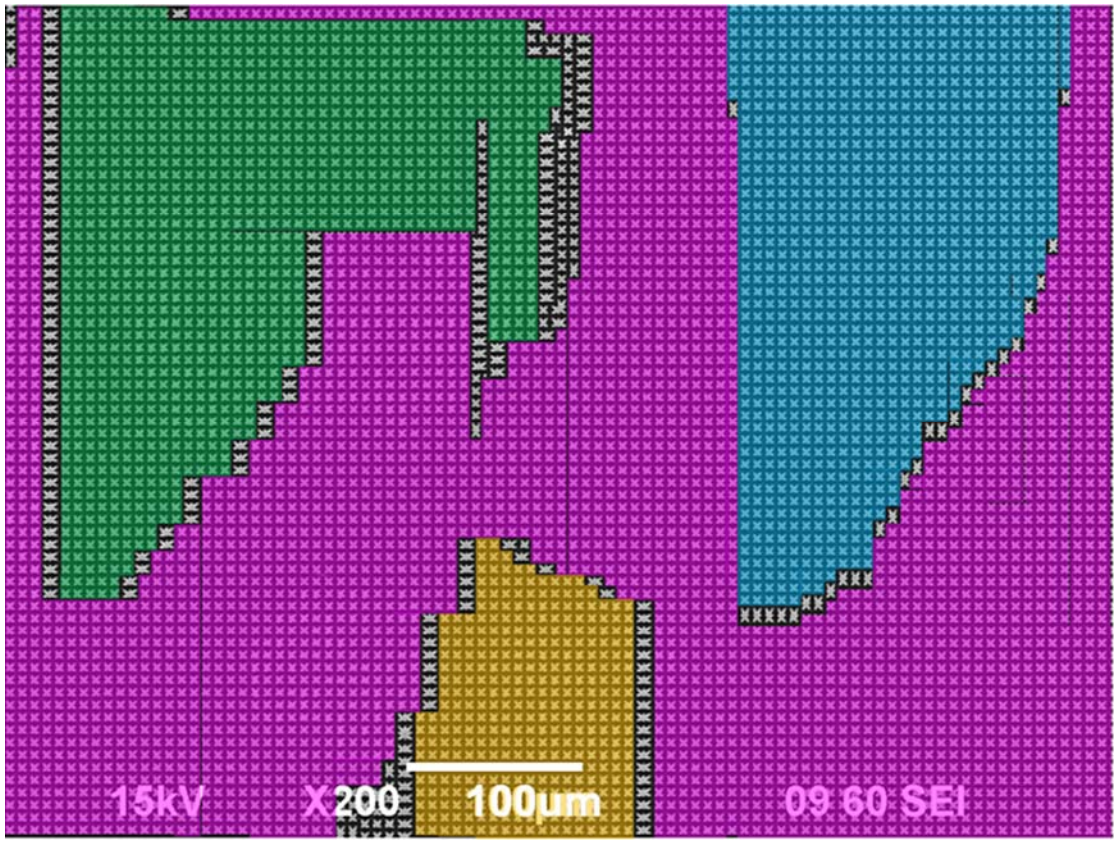


Figure 26. Large area view of the assembled fibers showing multiple domains and domain boundaries represented in color (scale bar = 100 μm). Reprinted from ref. 19, Copyright 2012, with permission from Elsevier.

## 5.2. Studies of the formation of domains during assembly

In literature, Paulose *et al.* studied the parameters of the assembling system contributing to

long-range order by modeling assembly as an irreversible sequential adsorption process on a square lattice[100]. When four-fiber assemblies form on an initially empty lattice as shown in Figure 27, they locally increase the probability of forming nearby clusters, thus generating ordered domains on a local scale. During this process, addition of adjacent fibers to the initial cluster is suppressed, analogously to excluded volume interactions for hard squares, due to the fact that as a fiber initially bends toward one neighbor to form a cluster, the neighbor on the other side experiences a weaker capillary force in that direction and tends to bend away from the forming cluster. However, two choices remain for the location of neighboring clusters. If they form directly next to the original cluster ($\alpha$ site), the long-range order is preserved, but if they form at a diagonal position ($\beta$ site), the order is disrupted and multiple domains are created. Using two parameters, they explained how these parameters control the likelihood of cluster formation at adjacent and diagonal positions[100].

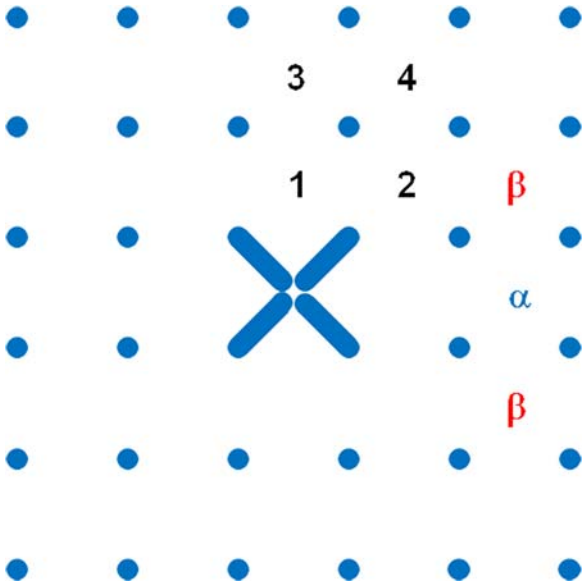


Figure 27. Schematic of formation of tetramers (top view). The numbers in the figure indicate first through fourth neighbor squares. The α site is the location where a tetramer can form a uniform domain whereas the β site is the location where a tetramer will form a domain boundary with the initial tetramer shown in the figure.

## 5.3. Using the controlled movement of an evaporation front to induce formation of a large domain

Based on the above understanding of the assembly formation, we made a hypothesis that controlling the movement of evaporation front might promote long-range order by preventing assembly from nucleating and propagating in a random manner. To test this idea, we used the experimental set up as shown in Figure 28a. To control evaporation front movement, we first immersed a sample in a solution (e.g. ethanol) and moved the sample upward along a lattice direction with a controlled speed using a syringe pump. One of the principal lattices of the fiber

arrays was aligned along the sample movement direction. In this case, we can expect that the meniscus would move row by row as the sample moves, as schematically shown in Figure 28b. We used both vertical and horizontal movement to test whether there is any effect of gravity. For a vertical motion, we used a World Precision Instruments UltraMicroPump with SYS-Micro4 Controller by attaching a sample mounting grip to the pump. For a horizontal movement, we used a KD Scientific KDS 210 syringe pump with a sample mounting grip. In terms of a trend, there was no difference between vertical and horizontal movement presumably due to negligible gravity effect because the liquid thickness covering the sample is smaller than the capillary length.

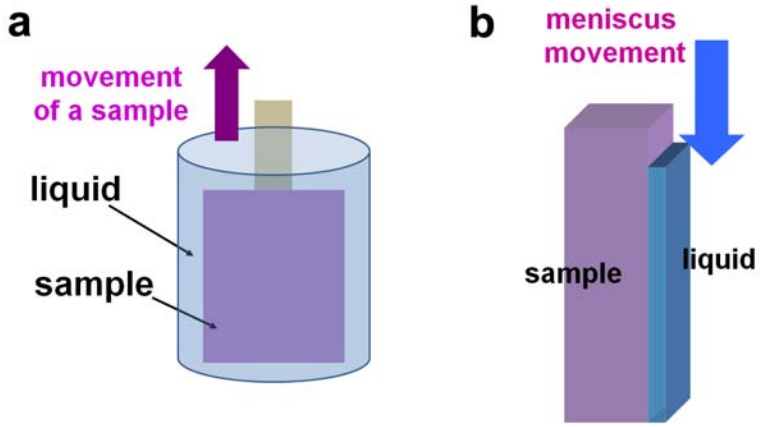


Figure 28. (a) (Front view) Schematic of an experimental set up for controlling movement of an evaporation front by moving a sample from a liquid after immersing the sample. (b) (Side view) Schematic of the meniscus movement for the configuration shown in (a). The detail of the meniscus is not shown in this schematic.

Controlling the evaporation front movement can manipulate the location of the nucleation sites such that the nucleation occurs row by row instead of random locations. Moreover, because

the portion of the sample immersed in the liquid cannot be assembled, we can effectively suppress the propagation of the assembly in other directions and just allow it to propagate along the sample movement direction. To test this idea, we have used microfibers which tend to form tetramers and have conducted experiments with and without the movement of the evaporation front. The fiber geometry was: the diameter of 1.7 μm, height of 10 μm, and spacing of 3.5 μm. The fiber was made of UV curable epoxy using the same procedure described earlier[5]. By doing this, we could form a large area ordered assembly (Figure 29) whereas the sample without any evaporation front movement resulted in small multiple domains, as shown in Figure 30.

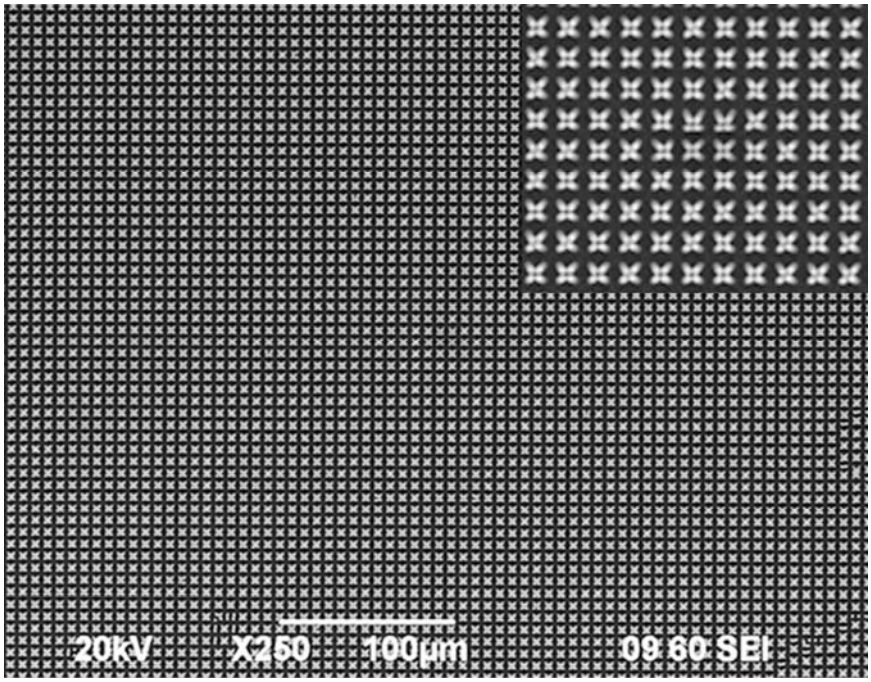


Figure 29. A SEM image of a large area uniform assembly patterns achieved by controlled movement of evaporation front. The inset shows the zoom-in of the assembly image. Reprinted from ref. 19, Copyright 2012, with permission from Elsevier.

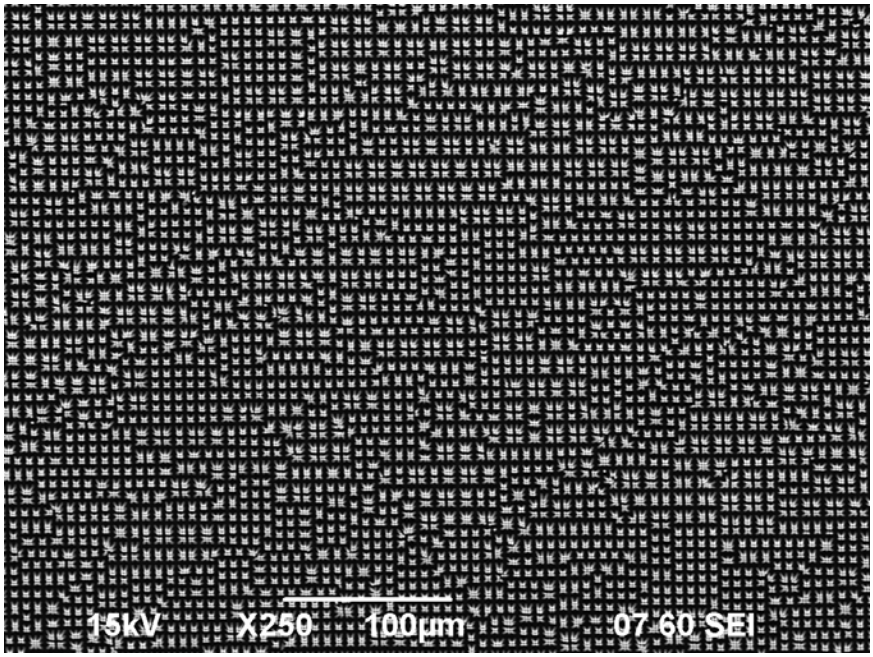


Figure 30. A SEM image of the sample without controlling evaporation front movement.

We then studied the effect of changing the sample movement speed and orientation. When we varied the sample movement speed from 0.3 to 3000 μm/s, we observed that there was an optimum speed for the largest domain formation (Figure 31). From this interesting trend, one may wonder what determines the optimum speed for the largest domain formation.

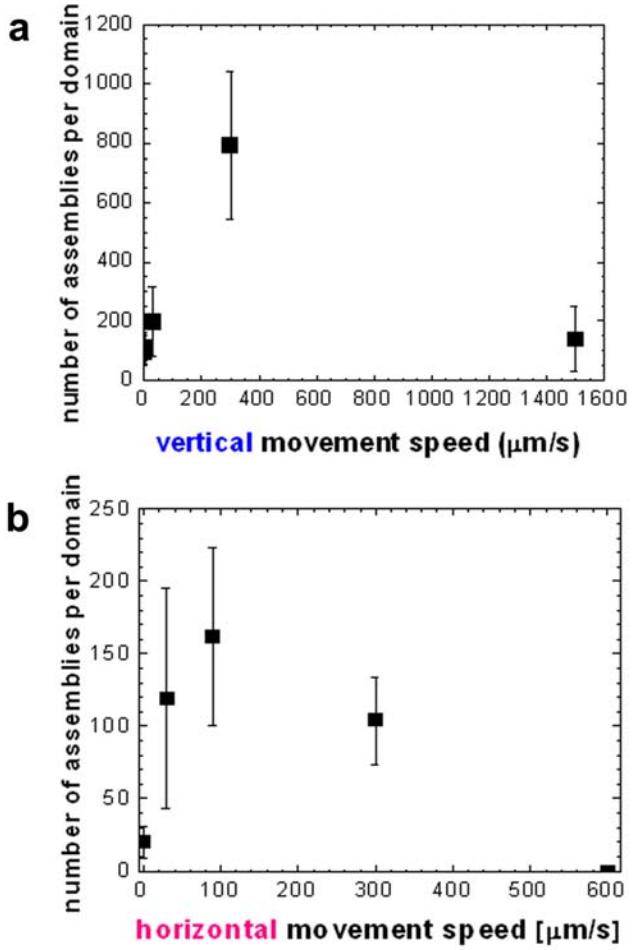


Figure 31. The number of assemblies per domain vs. (a) vertical and (b) horizontal movement speed data show there is an optimum movement speed for formation of the largest domain.

In addition, if we move the evaporation front slightly off the lattice direction, as shown in the inset of Figure 32, assembly patterns and domain boundaries not observed in typical

configuration appeared (see Figure 32 and analysis in Figure 33). Thus, by controlling the direction of the movement of the evaporation front, we can also change the assembly patterns.

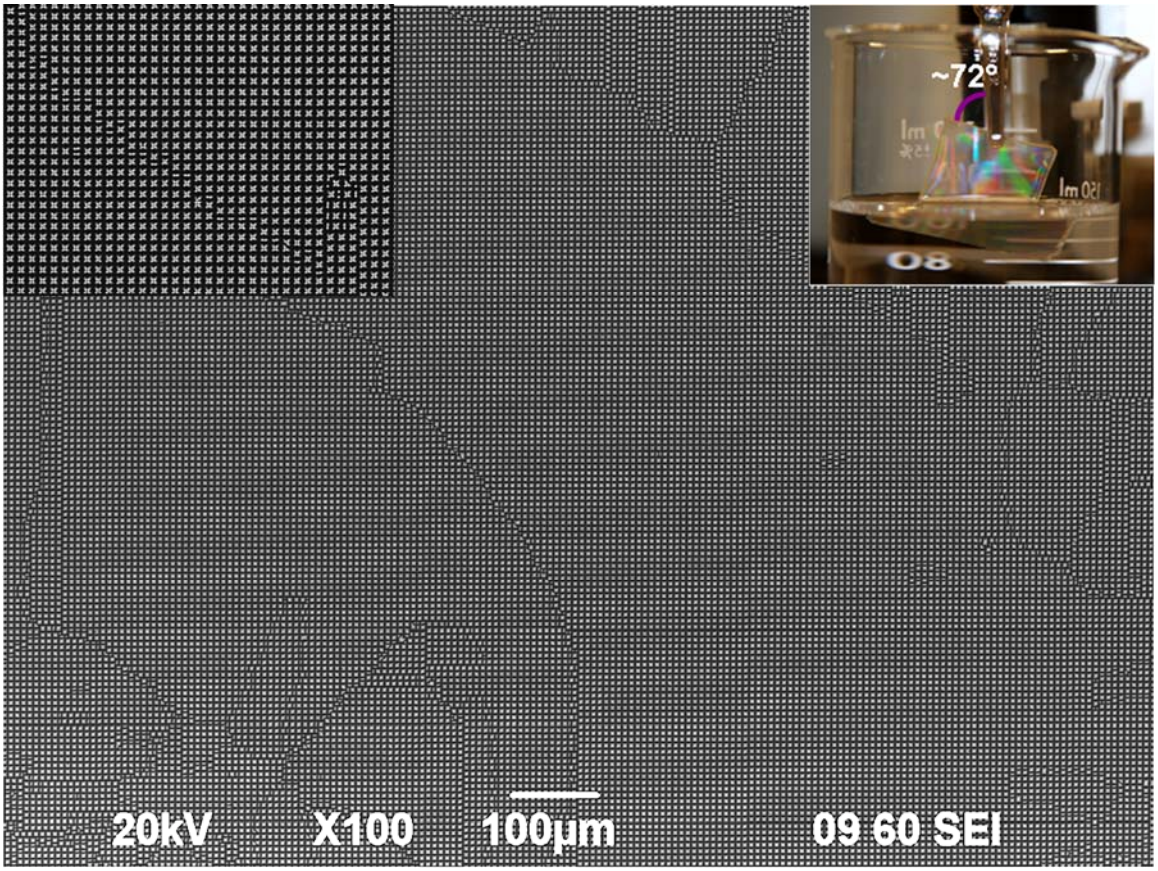


Figure 32. An SEM image of the assembly formed by off-lattice direction movement of the sample from a liquid. The insets show the zoom-in of the assembly pattern and the experimental set-up. 100% ethanol was used as a liquid.

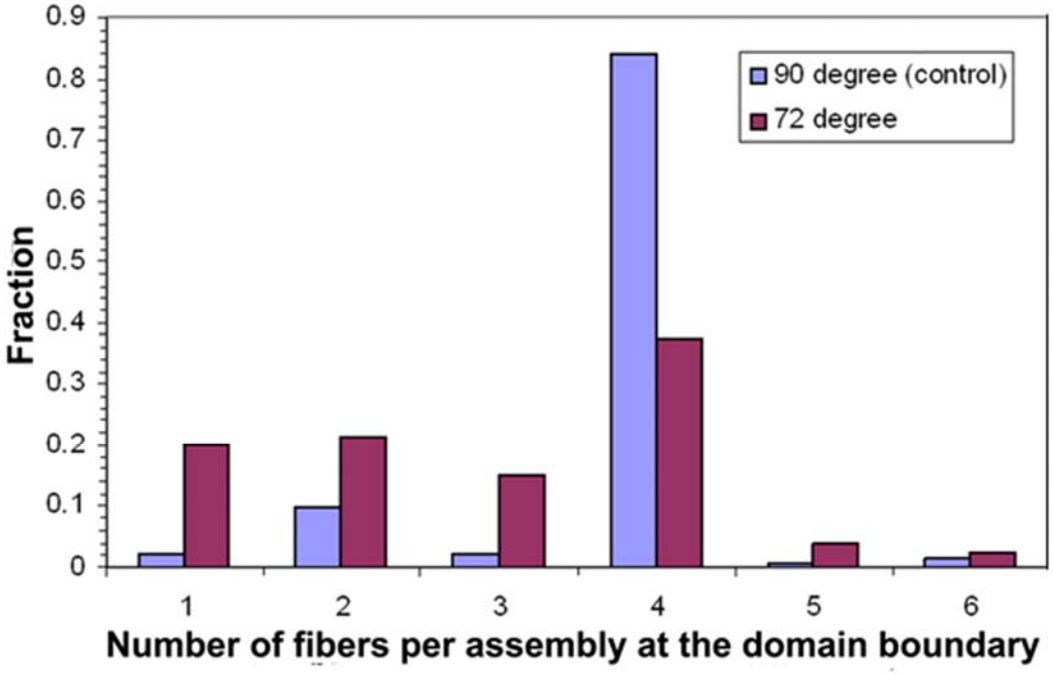


Figure 33. The fraction of the different assemblies at the domain boundary. The number on the x-axis shows the number of fiber arrays per assembly. The angle in the legend shows the angle of the movement direction with respect to the horizontal direction. Tetramers (assembly of four fibers) are dominant for the control sample while the sample moved off lattice direction resulted in clear increase of unusual assembly size for fibers arrays on a square lattice.

We then investigated the factors that affect the assembly process to understand the interesting relation between the size of the domain and the moving speed of a sample. To understand this trend, we have considered time scales involved with the assembly process. On the one hand, we can consider the time scale of evaporation, which is dependent on the liquid and the environment. From Figure 34, we can consider time scale to initiate assembly ($t_n$) and time scale of evaporation when the liquid level is the same or below the fiber height ($t_e$). Both times scales can be estimated using experimental parameters and measurement data as

$t_n = \frac{H_0 - h}{E_{m1}}$ and $t_e = \frac{h}{E_{m2}}$ ($H_0$: the liquid layer thickness, h: the fiber height, $E_{m1}$: the evaporation rate until the liquid thickness is above the fiber height).

On the other hand, we can consider the time scale for the propagation of the assembly, which is determined by the movement speed and the sample size. From Figure 34, we can consider the time scale for propagation of assembly ($t_p$) and the time scale for meniscus to reach the other end of a sample ($t_m$). They can be also described using measurable parameters as $t_p = \frac{L_1}{u_s}$ and $t_m = \frac{L}{u_s}$ ($L_1$: the length scale of the region with the liquid height lower than the fiber height, $u_s$: the sample movement speed, L: the sample size).

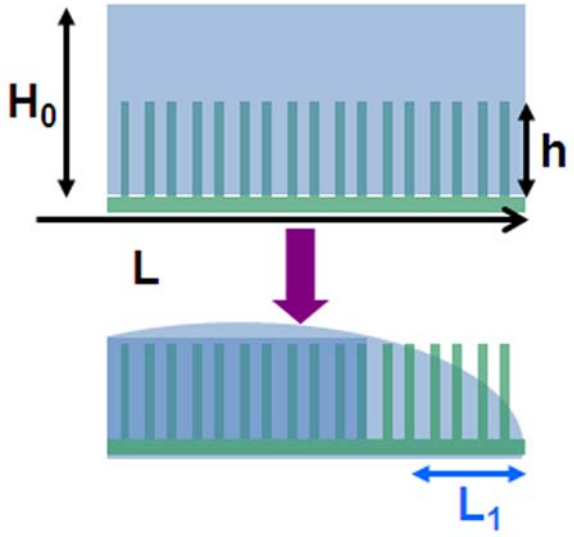


Figure 34. Schematic of the fiber arrays with a moving evaporation front. $H_0$ and h are a liquid layer thickness and a fiber height, respectively. L and $L_1$ are the sample length and the length scale of the region with the liquid height lower than the fiber height, respectively.

We made a hypothesis that the optimum speed of the movement is when the time scale of evaporation ($t_n$) is comparable to that of the movement ($t_m$) while the time scale for propagation

of assembly ($t_p$) is shorter than that of the evaporation time after the liquid level reaches the fiber height ($t_e$). Based on this idea, we have derived an expression for the optimum speed based on experimental parameters as equation (4).

$$u_s \sim \frac{LE_{m1}}{H_0 - h} \qquad (4)$$

To calculate the optimum speed, we then put experimental parameters to the equation (4). For the evaporation rate, we have measured the rate using a high precision balance (Mettler Toledo XP 105 Analytical Balance) by recording the mass change as a function of time (Figure 35). From calculation, we obtained ~ 77 μm/s as the optimum speed. The predicted optimum speed was comparable to the optimum speed of ~ 90 μm/s observed from experiments considering we did not have enough data points to find the optimum speed from experiment.

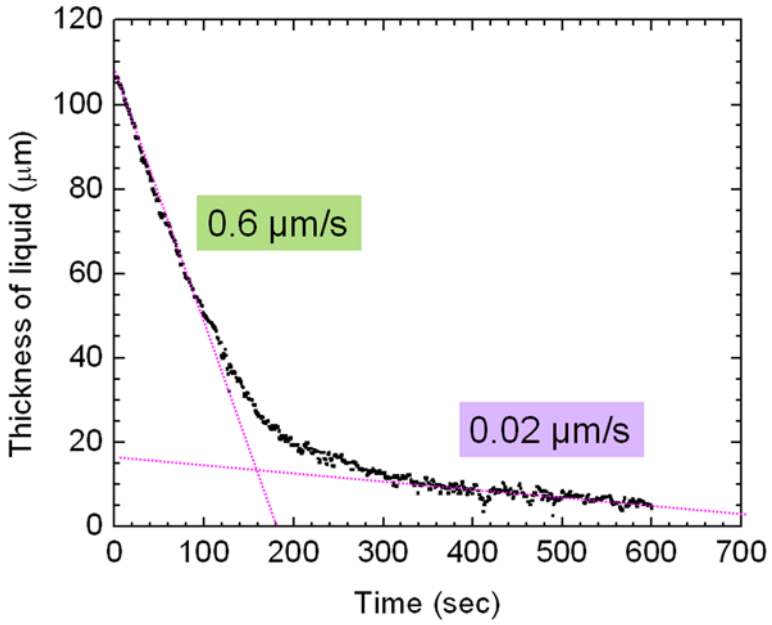

Figure 35. The evaporation rate measurement data. Ethanol was used as a liquid and the thickness of liquid was estimated from the mass of the liquid based on the area of the sample. The sample dimension was 23 mm by 23 mm. The evaporation rate was estimated by linear fitting.

## 5.5. Summary

Our results indicate that controlling nucleation and propagation of the assembly is crucial for a long-range order of the assembled clusters. In this chapter, we have used sample movement as a way to manipulate the nucleation and propagation of the assembly. From our study, there seems to be an optimum speed for the largest domain size and we have shown that the optimum speed is the case when the time scale of evaporation is comparable to that of the sample movement. Besides changing the meniscus movement speed, we can also consider introducing artificial nuclei by using a method such as e-beam assembly (see Chapter 8 for more details) to get a similar effect. Introducing artificial nuclei can be an interesting way to investigate how the interaction among nuclei influences the long range order and domain formation of the assembled system.

# Chapter 6 Modeling of Kinetics of Assembly

In chapter 6, we have studied how to model kinetics of assembly of fiber arrays. In the chapters 2 and 3, we described that the assembly process showed hierarchical kinetics and discussed the importance of considering kinetics to understand the assembly of fiber arrays. For better understanding of the assembly process, we have developed a simple model that simulates the assembly behavior. This chapter is based on our work that we prepare for publication (ref. 101).

## 6.1. Introduction

Nature has many intriguing materials systems with a combination of characteristics absent in current synthetic manufacturing materials such as stimuli-responsive property and multifunctionality. The distinct performance of biological materials attributed to hierarchical organization over different length scales. Natural materials exhibit unique properties from their structure and generative processes at all levels of the structural hierarchy[102,103]. Inspired by examples from nature, there have been many studies to generate synthetic hierarchical structures

by various processes such as photolithography[104], self-assembly[105], and combination of multiple processes[106].

Among many methods, self-assembly is particularly attractive because of its potential to generate complex hierarchical structures without sophisticated equipments and processing steps. As a result, there have been active studies to generate hierarchical structures by self-assembly using diverse building blocks including DNA[105], sol-gel with triblock copolymer[106] and nanoparticle/copolymer mixtures[107]. However, in many cases, the self-assembly process required specially synthesized building blocks[106,107] and/or multi-step control of assembling environment[105] while nature makes complex hierarchical architectures in ambient condition (room temperature and atmospheric pressure) with readily available building blocks. As an alternative approach, evaporation-induced self-organization is an interesting option that can address issues of other self-assembly processes with its simplicity in process, no need of additional energy source, and its potential for assembling structures across length scales[54]. Thus, there have been many studies that utilize evaporation process to induce hierarchical structures with a variety of building blocks such as nanoparticles[108], conjugated polymer solution[109], and arrays of fibers[22].

In particular, there has been a growing interest about evaporative self-organization of fiber arrays to understand intriguing pattern formation mechanism by fluid-solid

interactions[1,2,14,22,49,66-68,70,74,76-78,93,100,110-114] as well as to generate biomimetic (hierarchical) structures for a range of applications including drug delivery[49], sensing[115], structural color[69], and efficient heat transfer[65]. When a liquid is applied to fibrous surfaces, there are attractive capillary forces among fibers as a liquid evaporates while there are counteracting elastic forces due to attachment of fibers to a surface. Moreover, there are adhesion forces among fibers, which are crucial for maintaining assemblies after a system becomes dry. The interplay among different forces provides an opportunity to control shape and size of the fiber assembly patterns[49].

For a better understanding of the pattern formation, there have been works that estimate 1) the average assembly size by minimizing the sum of capillary and elastic energy of an individual assembly[14,69] or the entire system[110] and 2) the assembly size distribution by using a mean field theory[74], a spring-block approach[114], and Brownian dynamics simulation at a coarse-grained level[113]. Still, little has been known about the kinetics of the assembly process. In our previous experimental work described in chapters 2 and 3, we observed that the assembly of nanofibers showed a distinct kinetics with multistep hierarchical process[2], but there has been no model for this intriguing hierarchical kinetics that is crucial to understand the assembly process. In this chapter, we develop a simple model that captures nucleation and hierarchical clustering of fibers during the evaporation of the liquid in which they are immersed.

## 6.2. Background

Experimentally, the surface-attached micro/nanofiber arrays are fabricated by replica molding process[5]. Each fiber is fixed at the bottom end on a predefined lattice (most of cases, square lattice) on the substrate and free at the other end. This array is then immersed into a wetting fluid. When this liquid is evaporated, self-organization of micro/nanostructures occurs because fibers deform and adhere each other. Previous theoretical studies and experimental measurements suggest that the interplay between capillary and elastic forces is mainly responsible for the experimental observations explained above[14,69,76]. During evaporation of a liquid, capillary forces occur in a finite volume of matter with an interface such as liquid-vapor and/or solid-liquid etc., because the molecules at the interface are not surrounded by other molecules on all sides as in the bulk that and this leads to an interfacial energy. Minimization of the interfacial energy is at the origin of capillary forces and their explicit mathematical expression depends on the geometry of the system.

When two cylinders are partially immersed in a liquid, the capillary force between them can be described as equation (5)[93];

$$F_C = -\frac{\pi\gamma R^2 \cos^2\theta}{\sqrt{(x/2)^2 - R^2}} \qquad (5)$$

where $\gamma$ is the surface tension of the liquid, $R$ is the fiber radius, $\theta$ is the contact angle and $x$ is the

distance between two fibers, Notice that for large distances, the force decays as F(x) ~ 1/x. The elastic forces occur when the fibers bend during evaporation process because the bottom of a fiber is fixed on the substrate whereas the free ends may change its location. From the beam bending theory, the elastic force associated with this deformation is given by equation (6)[116];

$$F_B(\delta) = \frac{3\pi R^4 E\delta}{4h^3} \qquad (6)$$

where $\delta$ is the displacement from the initial position, $E$ is a elastic modulus, $h$ is the height of the fiber. In our minimal model, we assumed that all fibers stay together once they touch each other.

## 6.3. Our model for the kinetics of assembly

### 6.3.1. 1D model

For simplicity, we start by considering a one dimensional chain composed of N point particles connected by springs. Each particle interacts with its nearest neighbors (NN) on each side and also with an elastic foundation (substrate). We denote $x_i(t)$ the position of each particle. Then, we can write the sum of kinetic and potential energies of our chain as equation (7);

$$E = \varepsilon \sum_{i=0}^{N-2} [\frac{\rho \dot{x}_i^2}{2} + \phi(\frac{x_{i+1} - x_i}{\varepsilon}) + \frac{\kappa}{2}(x_i - i\varepsilon)^2] \qquad (7)$$

Here, the function ϕ defines NN interactions between particles and it will be specified below, ε is the reference inter-particle distance, ρ is the mass per unit length, μ is an elastic constant, $\kappa$ is a spring constant, and $\dot{x}$ denotes time derivative. The last term of equation (7) describes the

bending elasticity. Note also that the position vector can be re-written as $x_i = i\varepsilon + u_i$, where $u_i$ is the displacement from the equilibrium position.

We use the function $\phi$ to describe attractive capillary forces for large distances and repulsive short range interactions to avoid interpenetration of particles. One can use a Lennard-Jones type potential for this purpose given by

$$\phi(r) = A[(\frac{\sigma}{r})^{12} - 2(\frac{\sigma}{r})^{6}] \qquad (8)$$

where $r_i = x_{i+1} - x_i$ is the distance between sites and A is a constant and defines the depth of the minimum of the potential and $\sigma$ is the equilibrium length of the springs, i.e. $\phi'(r)=0$. For short distances, the first term at the right hand side of equation (8) dominates and forbids the sites to penetrate. The second term at the right hand side of Eq. (8) describes attractive capillary forces. The resulting potential energy is shown in Figure 36. We stress that our choice of Lennard-Jones potential is only phenomenological and a more appropriate quantitative choice for this potential is a subject of a future study.

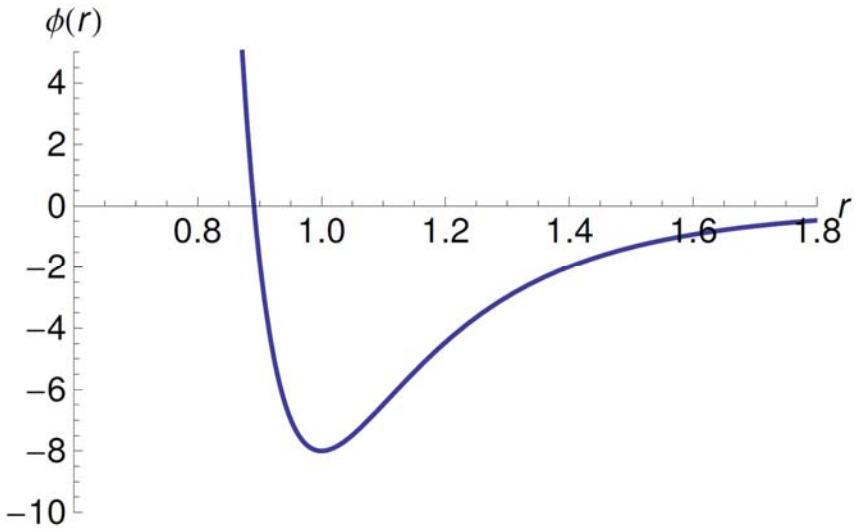


Figure 36. The Lennard-Jones potential used in the model.

To stabilize the dynamics and to make the description more realistic, we also need to include viscous dissipation. The corresponding dynamic equation takes the form of equation (9) as below where γ is viscosity.

$$\rho\varepsilon\ddot{x}_i + \gamma\dot{x}_i = [\phi'(\frac{x_{i+1} - x_i}{\sigma}) - \phi'(\frac{x_i - x_{i-1}}{\sigma}) - \varepsilon\kappa(x_i - i\varepsilon)] \qquad (9)$$

We include the increase of capillary forces between the sites due to the evaporation of a liquid by defining a slowly decaying function in time as equation (10)

$$\sigma(t) = \sigma_0(1 + a(t)) \qquad (10)$$

where $\sigma_0$ is the initial equilibrium length and we choose $a(t)$ as

$$a(t) = 0.5(e^{-t\lambda} - 1) \tag{11}$$

where λ is the decaying rate. The velocity of loading is given by

$$\dot{\sigma}(t) = -ve^{-t\lambda} \tag{12}$$

where $v$=0.5$\sigma_0\lambda$ measures the slowness of the driving, $\sigma_0$ is the initial equilibrium distance and $\lambda$ is the decaying rate of potential. With this choice, we shift the equilibrium distance in favor of smaller distances as shown in Figure 37.

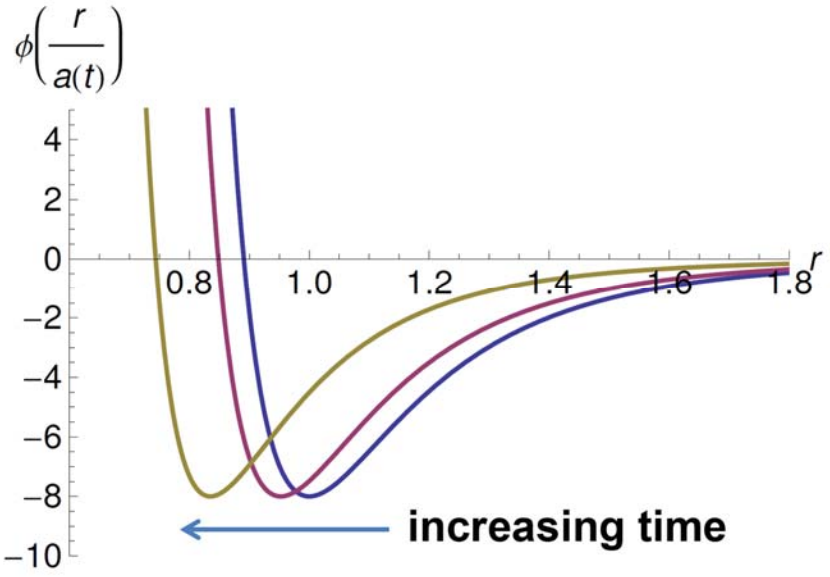


Figure 37. The Lennard-Jones potential with respect to function a(t).

By choosing the non-dimensional parameter as equation (13),

$$\tilde{x} = \frac{x}{\varepsilon}, \tau = \frac{vt}{\varepsilon} \tag{13}$$

then we rewrite the dynamic equation in a dimensionless form

$$M\frac{d^2}{d\tau^2}\tilde{x}_i + W\frac{d}{d\tau}\tilde{x}_i = [\phi'(\frac{\tilde{x}_{i+1}-\tilde{x}_i}{h}) - \phi'(\frac{\tilde{x}_i-\tilde{x}_{i-1}}{h}) - \omega^2(\tilde{x}_i - i) \qquad (14)$$

where $M = \frac{\rho v^2}{\phi''(\varepsilon)}, W = \frac{\gamma v}{\phi''(\varepsilon)}, \omega = \varepsilon\sqrt{\frac{\kappa}{\phi''(\varepsilon)}}, h = \frac{\sigma(t)}{\varepsilon}, \tilde{\phi} = \frac{\phi}{\phi''(\varepsilon)}$ (15)

Notice that the ratio $M/W^2$ is independent of driving force and gives a measure of the ratio of inertial force to viscous force, whereas $\omega^2$ is the ratio of the elastic force to capillary force. The parameter $h$ is the ratio of the initial distance between fibers $\varepsilon$ to the equilibrium distance $\sigma(t)$.

Without the appropriate boundary conditions, the above equation is underdetermined. We use fixed boundary condition for the right end, we have $\tilde{u}_0 = 0$. We slightly oscillate the last particle to perturb the system $\tilde{u}_{N-1} = B\sin(ft)$, where $B$ and $f$ are the amplitude and frequency of oscillations, respectively. In modeling of realistic material response, one cannot neglect disorder due to various chemical and mechanical imperfections. Such disorder can influence the behavior of the system by facilitating nucleation and propagation of assemblies. In our case, the initial separation distance ε between fibers may or may not be same for each pair of fibers. This can be incorporated into the model by randomly distributing the initial equilibrium distance $h_i = 1 + \delta_i$, where $\delta_i$ is a random number distributed according to

$$P(x) = (\sqrt{2\pi\mu^2})^{-1}\exp(-x^2/\sigma^2) \qquad (16)$$

where $\mu$ is a variance. This term allows us to study the influence of different degrees of disorder

on the assembly formation.

We numerically solved the equation (14) using a semi-implicit finite difference method and present the solution of equation (14) using different parameters. The choice of parameters is defined by experimental observations. For example, we observe hierarchical assembly in time when fibers are long that implies their stiffness is small. For this case, we choose a relatively small $w$ that defines the ratio of elastic forces to capillary forces, we have $\omega^2 = 0.1$. Second, we are mostly interested in over damped limit and hence, we use $M = 0.001$ and $W = 1$. The decaying rate has taken as $\lambda = 1$. The degree of disorder will be specified in each case. The amplitude perturbation on the last site is chosen to be $B = 0.0001$.

In our first simulation, we consider a case with a small disorder with $\mu = 0.001$. Figure 38 shows snapshots of the displacement vector $u_i$ in different times. One can see that the position vector has discontinuities in some regions. These correspond to the broken springs, i.e. the force is zero on this springs. This is exactly the regions where assemblies form. Under continuous evaporation controlled by equation (12), assemblies continue to grow (see Figure 38b) and at later times small clusters come together in favor of bigger clusters (see Figure 38c and Figure 38d).

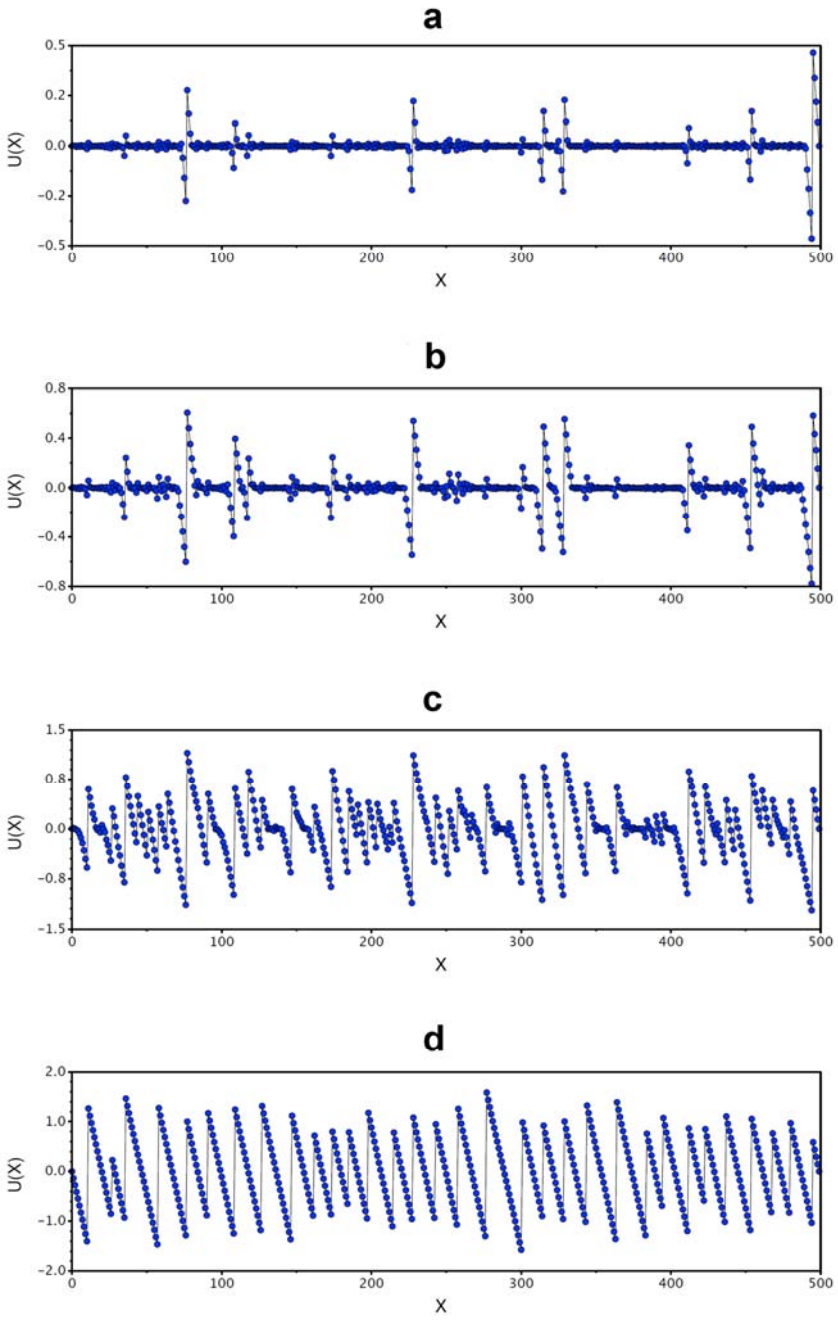


Figure 38. Time evolution of position vector $x_i$ for a system size N = 512.

In order to have a better understanding, we measure the average cluster size shown Figure 39. We observe step-wise increase of average cluster size as a function of time with finite

duration. These steps are meta-stable states and they persist if the driving is stopped.

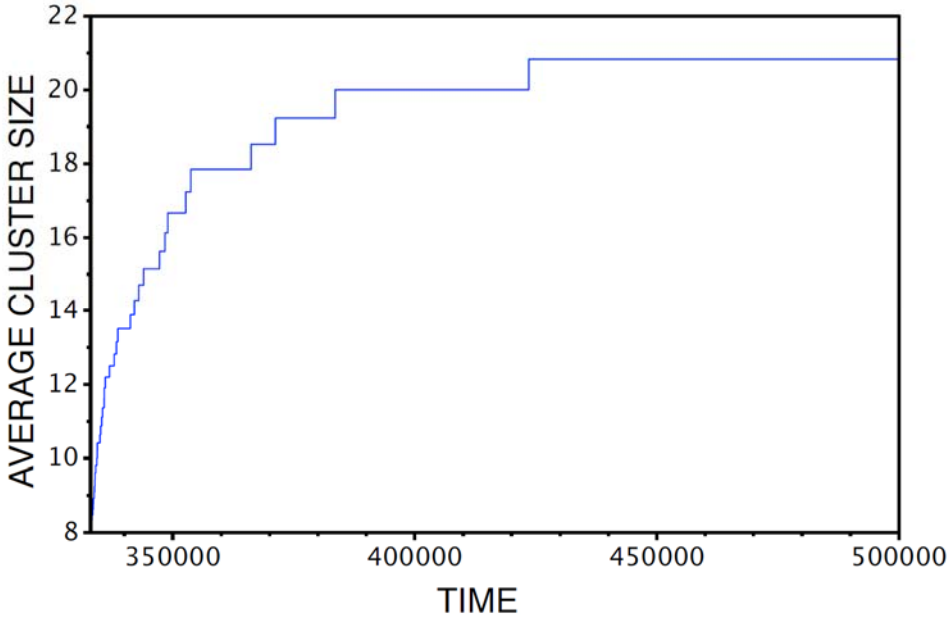


Figure 39. Time evolution of average cluster size.

In the second simulation, we consider a disorder-free fiber array composed of relatively stiff pillars with $\omega^2 = 5$. Time evolution of fiber position for 300 fibers is shown in Figure 40. We observe that the propagation starts at the slightly perturbed right boundary and propagate into the bulk consistent with experiments.

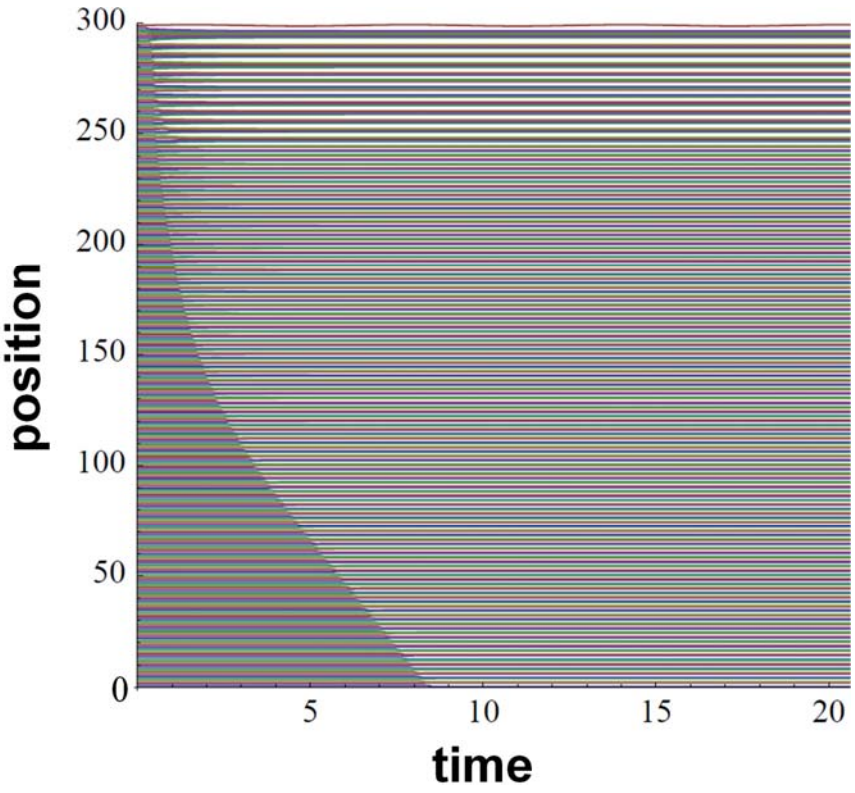


Figure 40. Propagation of assembly front. White space corresponds to the large inter-fiber distances that separate assemblies.

We also repeated this simulation with different values of $\omega^2$. From the simulation results, we plotted the fraction of broken springs as a function of stiffness as Figure 41. We observe that for largest stiffness value, all springs break, and thus, there is no assembly. The general behavior that we observe is that for larger stiffness values, we have smaller clusters, i.e. average cluster size is increasing with decreasing stiffness value as similar to the experimental observation in Chapter 3.

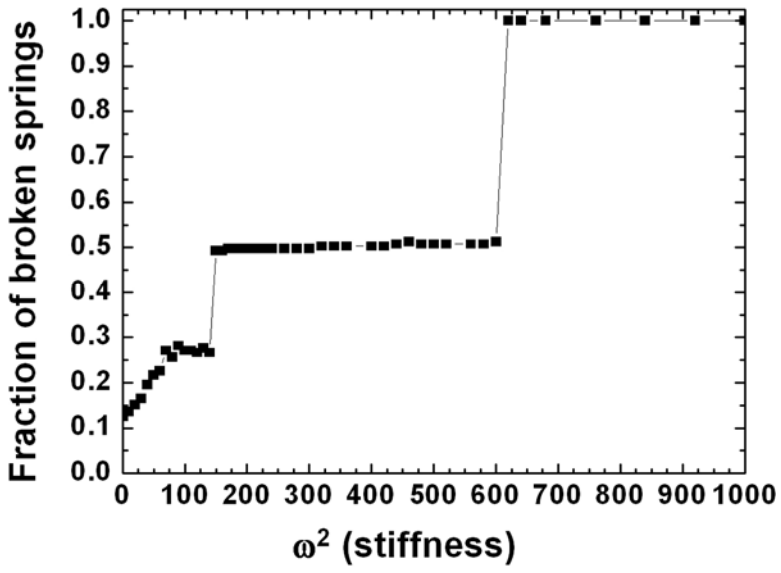


Figure 41. Fraction of broken springs as a function of relative stiffness $\omega^2$.

### 6.3.2. 2D model

Even though the solution obtained in the 1D model are qualitatively in agreement with experiments, some of the experimental observations such as domain boundaries or crack propagation cannot be understood in 1D. Therefore, in this section, we extend our model to the 2D case. In two dimensions, the positions of fibers are defined by a vector $X\mathrm{i} = \{x_i, y_i\}$, where $x_i$ and $y_i$ are the coordinates of a fiber for $i$ = (0, N-1 × N-1). The distance between a pair of fibers $(i, j)$ is then given by

$$r_{ij} = \left|X_{ij}\right| = \sqrt{(x_j - x_i)^2 + (y_j - y_i)^2} \qquad (17)$$

where $r_{ij} = |X_{ij}|$ is the distance between fibers $i$ and $j$. In the following, we will assume a square lattice and therefore the initial inter-fiber spacing ε is same in both directions: we have $x_i = u_i + \varepsilon i$ and $y_i = v_i + \varepsilon i$, where $u_i$ and $v_i$ are horizontal and vertical displacements, respectively.

In two dimensions, we will again use a Lennard-Jones potential given by equation (8). The force acting on each fiber located at $X_i$ due to fiber $j$ is given by

$$f_{ij} = (-\frac{1}{r_{ij}}\phi'(r_{ij}))X_{ij} \qquad (18)$$

We can explicitly write the dynamical equations for $x_i$ and $y_i$. For simplicity, following the dimensional analysis of the 1D model, we directly write dimensionless equations of motion:

$$M\frac{d^2}{d\tau^2}\tilde{x}_i + W\frac{d}{d\tau}\tilde{x}_i = \left[\sum_{j\neq i}^{NN}\tilde{f}_{ij} - \omega^2(\tilde{x}_i - i)\right] \qquad (19)$$

$$M\frac{d^2}{d\tau^2}\tilde{y}_i + W\frac{d}{d\tau}\tilde{y}_i = \left[\sum_{j\neq i}^{NN}\tilde{f}_{ij} - \omega^2(\tilde{y}_i - j)\right] \qquad (20)$$

where the total force acting on fiber $i$ is only due to NN interactions. The dimensionless force is given by $\tilde{f}_{ij} = (-\frac{1}{r_{ij}}\tilde{\phi}'(r_{ij}))X_{ij}$, where $\tilde{\phi}$ is defined in equation (15).

As in the one dimensional model, we realize simulations with different parameters. The boundary conditions in 2D are $\tilde{u}_{N-1,j} = \tilde{v}_{N-1,j} = B\sin(ft)$ at the left boundary for $j$ = 0, *N-1* and $\tilde{u}_{0,j} = \tilde{v}_{N-1,j} = 0$ at the other boundaries. Motivated by experiments and our numerical simulations, we first consider the case with a small stiffness with $\omega^2$ = 0.1 in over-damped

regime with $M = 0.001$ and $W = 1$ and a small disorder $\mu = 0.001$. All of the other simulation parameters are same as in the first example in 1D model.

Time evolution of displacement vectors of fibers is shown in Figure 42. We observe that the assembly starts at the right boundary with assembly of size $2 \times 1$. However, the life time of these assemblies is very short and the system prefers to form $2 \times 2$ clusters, which have much longer life times. Under continuous evaporation, these assemblies transform into bigger assemblies of different sizes as Figure 42c and Figure 42d. For a better visualization, we show the time evolution of a fixed region in the array as Figure 43, where we see the formation of clusters in a hierarchical order.

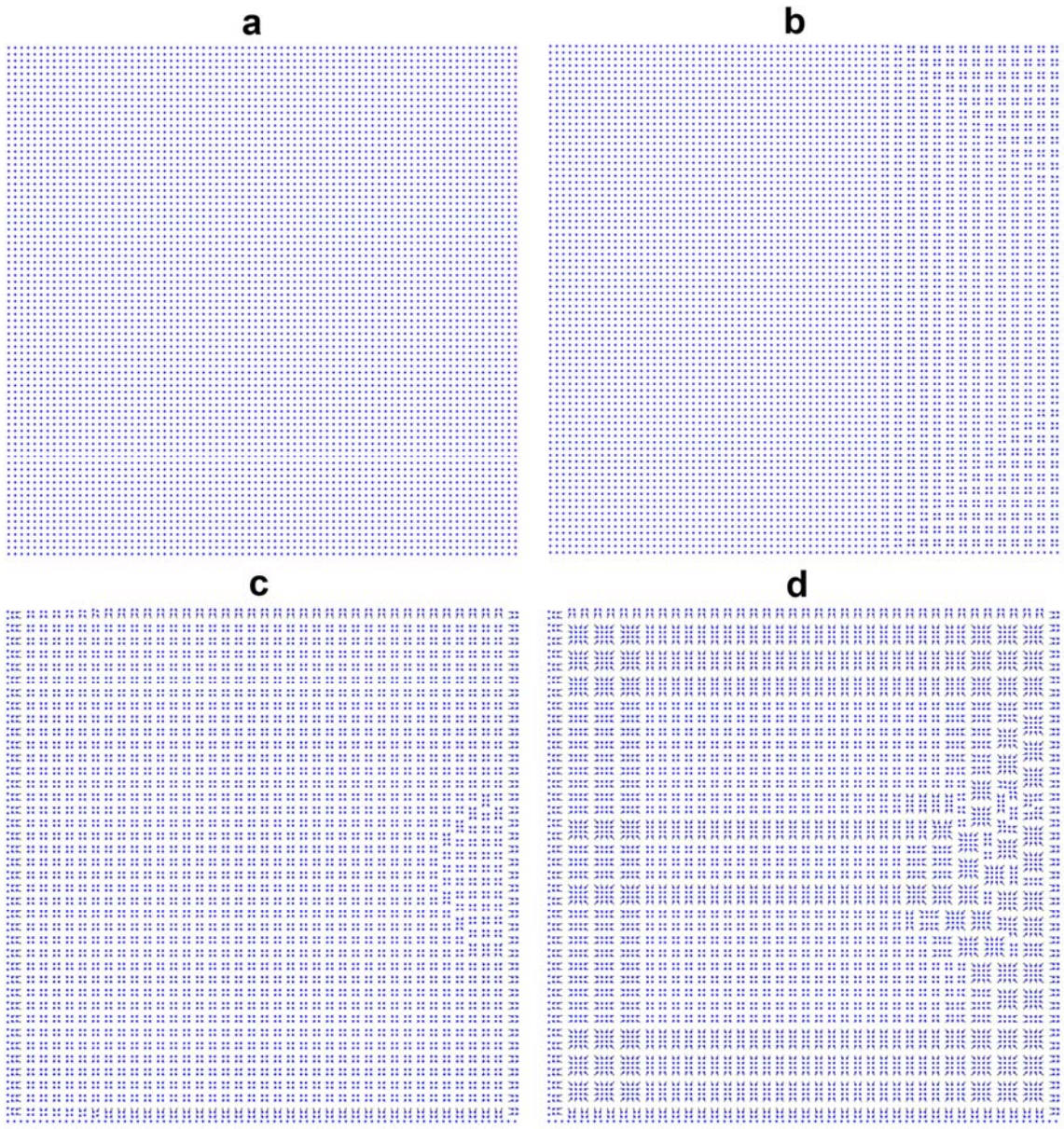


Figure 42. Time evolution of the fiber array during evaporation.

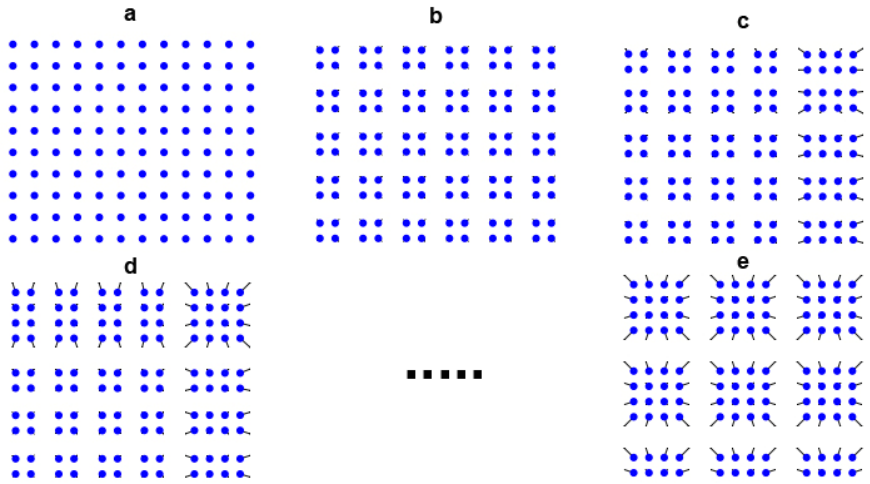


Figure 43. Time evolution of a small region from Figure 42 during evaporation.

## 6.4. Summary

In this chapter, we have described the assembly of fibers using a simplified model that captured important characteristics of assemblies of fiber arrays observed from experimental results. Most notably, our numerical model showed a step-wise kinetics as a spring breaks between particles due to change in the reference state as time goes on, which mimicked the hierarchical kinetics observed from experiments. The Lennard-Jones potential that we used as a phenomenological model describing fiber interaction showed a good agreement with experimental results, but a more appropriate quantitative choice for this potential can be an interesting topic for future study. We believe the ability to model the assembly process can open a new opportunity to program the dynamic assembly behavior and give us new insights to understand the assembly process.

# Chapter 7 Applications of the Wetting-Induced Fiber Clustering as Enhanced Security Features

So far, we have described pattern formation mechanisms of fibrous surfaces by self-organization. Based on our understanding, we can also use the assembly process for various applications such as trapping and releasing of objects[2], structural color[69] and sensing molecules[115]. In this chapter, we will focus on describing how the assembly of fibrous surfaces can be used as enhanced security features for polymer-based security documents, such as banknote. This chapter is based on our patent application (ref. 117).

## 7.1. Introduction

The inception of the first polymer-based banknotes in Australia in 1988 has provided a new perspective to the global economic security[118]. The new polymer banknote material, named Guardian™, was developed jointly by the Reserve Bank of Australia, Commonwealth Scientific and Industrial Research Organization (CSIRO), and the University of Melbourne[118,119]. The key advantages of using polymer as banknote material over the traditional papers are longer life time (i.e., at least 4 times longer than that of the paper), greater tear resistance and durability, liquid

resistance, as well as increased difficulty in counterfeiting compared to the traditional paper-based banknote[120-122]. If we take the United States as an example, its currency is known to be vulnerable to counterfeiting because its design was created in 1920s, and with rapid improvement in printing technology, such as high resolution scanners and printers, there has been a growing number of counterfeiting events. In 1995 only, over 360 million counterfeit notes were confiscated, and it is estimated that more than billion dollars were undetected. This counterfeited money is used for arm purchase, drug trade and terrorist activity, which is a serious threat for homeland security as well as international welfare[123]. This leads to the progressive popularity of the use of polymer-based banknote. At present, there are at least 30 different denominations totaling > 3 billion banknotes that are currently circulating in ~ 30 countries, which accounts for ~15% of the all countries in the world[124,125]. As a result, there is a great demand in developing advanced anti-counterfeiting features specifically for polymer-based banknotes.

Owing to the unique material properties and manufacturing techniques of the polymer thin film, new security features were introduced into the polymer-based banknotes that were not available to the paper-based ones. For instance, Guardian™ banknote employs optical transparent windows with embossed microscale features which are incorporated within the polymer substrate[126-128]. Two-dimensional (2D) optical devices, in the form of diffraction

gratings, iridescent bands, and shadow images, can also be introduced into the optically transparent window through embossing techniques[127-131]. While the introduction of these new anti-counterfeiting features into polymer-based banknotes has greatly increased the currency security, the full potential of anti-counterfeiting methods suitable for polymer substrate has not yet been realized. To further enhance the security features of the polymer-based banknotes, we introduce a suite of novel security features based on our recent developments of nano/micromechanical structure fabrication and self-assembly technologies[2,48,49,112], which utilizes a wet anti-counterfeiting approach that is not currently available in the existing anti-counterfeiting methods for polymer-based banknotes.

## 7.2. Dynamic color switching

The first security feature makes use of the phenomenon of structural color that is commonly observed in nature. Particularly, it is well-known that many creatures, such as butterflies and birds, utilize their surface morphologies to display a variety of optical effects for different functional purposes[132-135]. This unique feature of structural color is attributed to the highly periodic surface features, whose length scales are on the orders of 100 nanometers to a few micrometers [132-135]. Inspired by these natural designs, we have developed a number of nanostructured surfaces that can perform dynamic color switching through surface

topography-induced wetting and drying processes.

We fabricated a highly periodic, clustered surface using epoxy resin, with surface features in the form of high-aspect-ratio cylindrical structures. When the surface is in a dry state, it displays a pearl-like color due to the coherent scattering of light from the periodic, clustered fibrous surfaces (Figure 44a). When liquid, such as alcohol, is applied to the surface, it wets the surface completely due to surface topography-induced wetting[136-138]. The liquid wetting process causes the fibrous surfaces to be unclustered partially, which greatly enhances the structural color effect (Figure 44b). As the liquid evaporates, the structural color disappears as the periodicity of the nanostructures is disrupted by the clustering of the nanostructures into larger-sized assemblies (Figure 44c). Upon the completion of the liquid evaporation process, the fibrous surfaces restore its original configuration due to their structural flexibility, thereby restoring the original structural color (Figure 44d). It is important to note that such a dynamic color switching process cannot be achieved using the current 2D optical grating[129-131,139] or holographic technologies[140,141], which are employed in the current security documents. Additionally, security features in the form of arbitrary graphics at high resolution can be fabricated on the polymer surface with nanomechanical structures.

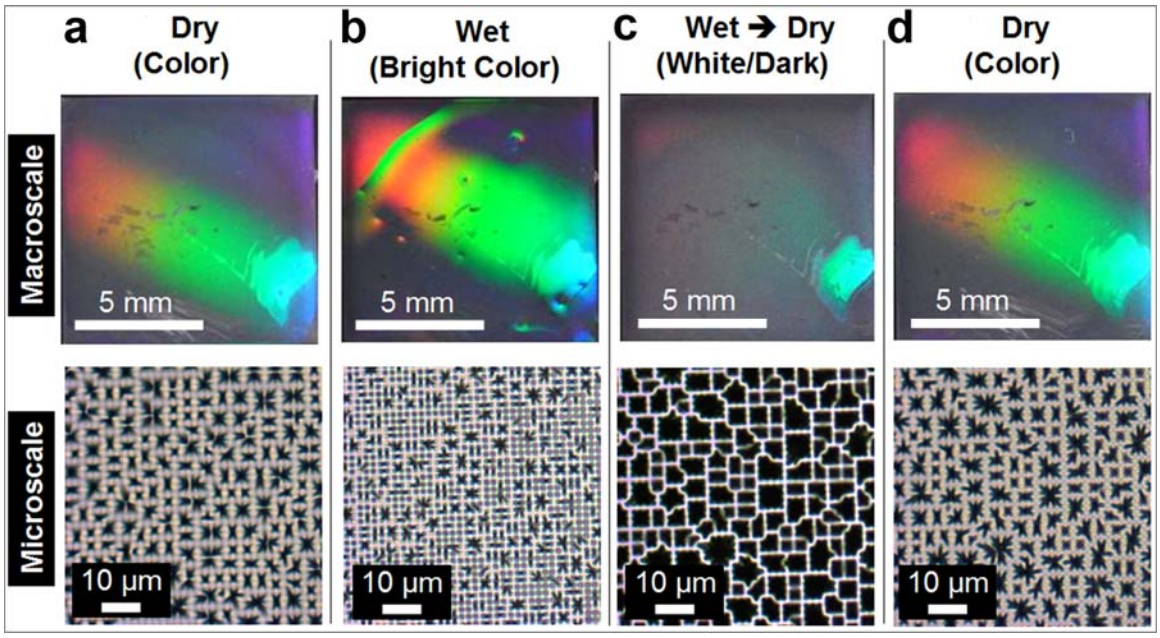


Figure 44. Dynamic color switching. Optical images showing the color switching capability of the reconfigurable fibrous surfaces. (a) When the surface is in the dry state, color fringes are observed due to the optical grating effect. This effect is caused by the length scale matching between the pitch of the clustered nanomechanical structures and the wavelengths of visible light, λ (see the microscopic images). (b) The optical grating effect becomes more pronounced when the surface is wetted due to partial unclustering of the fibrous surfaces, where the pitch of the structures now matches closer to the wavelengths of visible light. (c) When the wetted surface is drying, the fibrous surfaces are clustered into larger assemblies due to elastocapillary effect, which disrupts the optical grating effect and renders the surface to appear dark. (d) When the surface is completely dried, the fibrous surfaces resume to their original structural morphologies, thereby restoring the original optical grating effect.

## 7.3. Nanomechanical structure-induced optical fuzziness

The second security feature utilizes the effect of diffraction to optically distort any embedded characters within the polymer substrate. Specifically, diffraction occurs when an electromagnetic wave, with a wavelength λ, passes through a physical slit with size comparable

to or smaller than λ. By utilizing this physical phenomenon, our surfaces can generate optical fuzziness of embedded images through the collective diffraction effects of the 3D nanomechanical structures. By engineering the distance between the individual nanostructures (i.e., the pitch), we can tune the optical fuzziness of the embedded images from highly fuzzy to negligible fuzziness (Figure 45b). In addition, the optical fuzziness can be further enhanced by adjusting the height of the nanostructures at a pitch size less than 1 μm, which are comparable to the wavelengths of light in the visible spectrum (i.e., λ ~ 300 nm to 700 nm) (Figure 45c). This enhanced security feature can be incorporated into the existing security documents, particularly in polymer-based banknote, where characters can be embedded within the 3D nanomechanical structures with tuned pitch and height to generate the desired optical fuzziness.

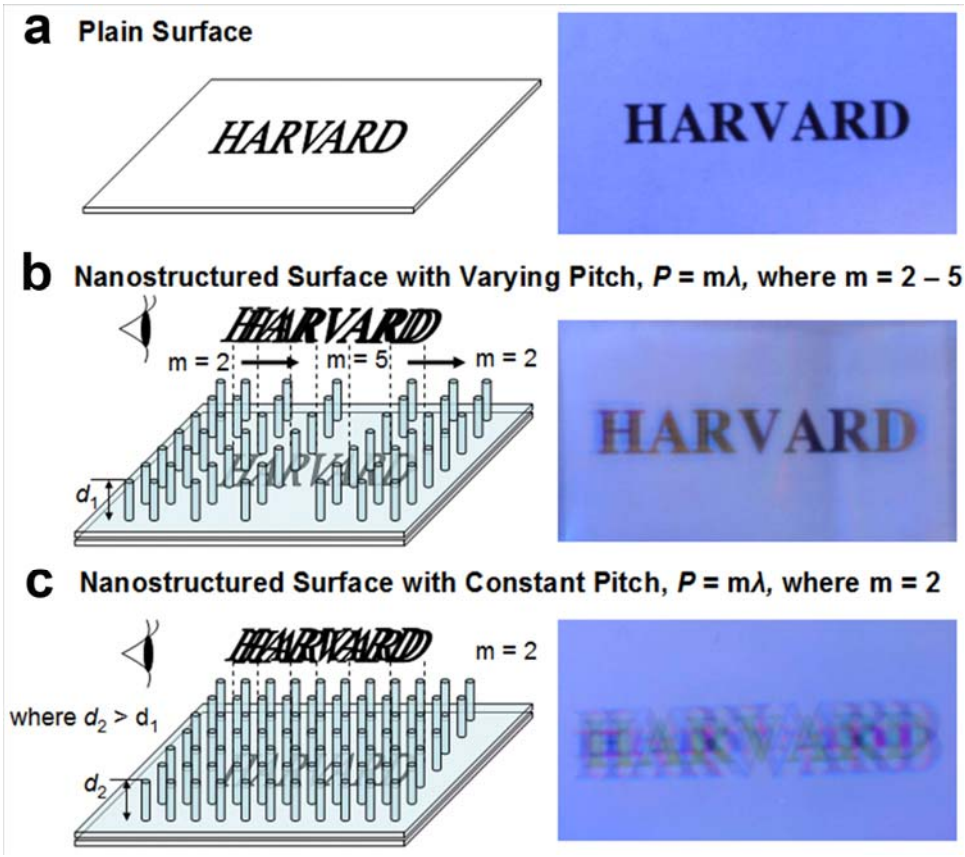


Figure 45. Nanomechanical structure-induced optical fuzziness. Optical images (right) and schematics (left) showing the effect of nanomechanical structures to induce optical fuzziness of embedded characters – "HARVARD". (a) Plane surface without any structure. The optical fuzziness becomes more pronounced when the pitch of the structures approaches the wavelengths of visible lights due to enhanced optical diffraction (b). The degree of optical fuzziness can be further enhanced by varying the height of the nanomechanical structures (c).

## 7.4. Dynamic optical transparency switching

The third security feature makes use of the optical refractive index matching between two different materials in order to create transient optical transparency within the polymer substrate. In particular, when the nanostructured surface shown in Figure 45c is wetted with a liquid whose refractive index, $n_{liquid}$, matches that of the solid polymeric material, $n_{solid}$, the characters that are

embedded within the substrate appear to be sharp due to reduced light diffraction as a result of index matching of the materials (i.e., these two different materials optically appear to be the same, see Figure 46). Upon liquid drying, the surface that stays wet will remain optically transparent, whereas the region that is dried up will appear to be optically fuzzy as illustrated in section 7.3. When the surface is completely dried, the optical fuzziness of the characters recovers the original state (Figure 46). This feature, when incorporated with security documents, provides a very simple way to identify their authenticity by simply wetting the surface with ordinary liquids or simply by breathing on it.

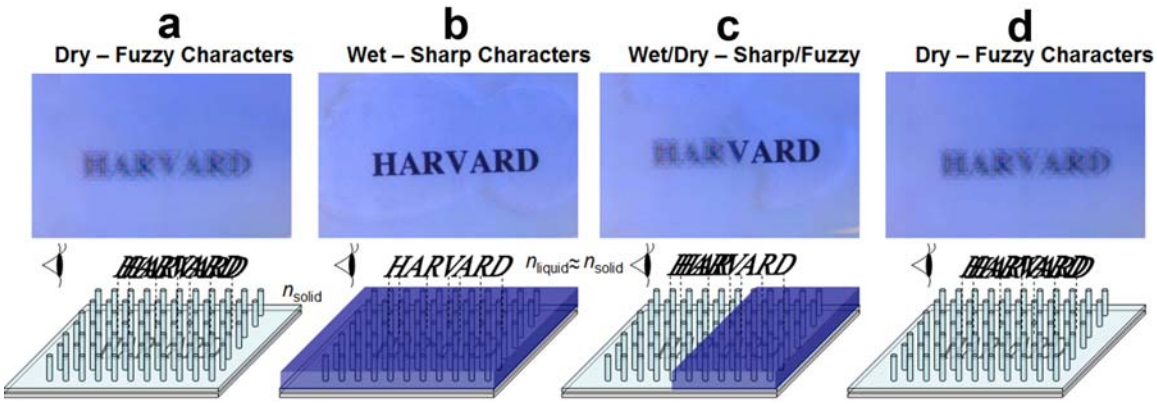


Figure 46. Dynamic optical transparency switching. Optical images (top) and schematics (bottom) showing the dynamic optical transparency switching of the fibrous surfaces with embedded characters – "HARVARD". (a) When the surface is in the dry state, the embedded characters appear to be fuzzy due to the optical diffraction effect. This effect is caused by the length scale matching between the pitch of the fibrous surfaces and the wavelengths of visible light. (b) When the surface is wetted with a liquid whose refractive index, $n_{liquid}$, matches to that of the solid material, $n_{solid}$, the characters appear to be sharp due to the reduced light diffraction as a result of optical refractive index matching of the materials. (c) When the wetted surface is drying, characters remain sharp in the region where the liquid is covered. (d) When the surface is completely dried, the optical fuzziness of the characters resume to the original state.

## 7.5. Summary

We have demonstrated a suite of enhanced security features utilizing 3D nano/micromechanical structures fabricated on polymeric substrates, which are capable of producing dynamic, visually distinctive optical effects in both wet and dry environments. To produce these effects, the geometry, wetting and mechanical properties of the structured surfaces are specifically engineered based on our understanding of fibrous surfaces. For example, the geometries and the materials properties of these structures can be engineered such that they have

strong interactions with visible light to create optical scattering and diffraction effects, as well as tailored structural flexibility for enhanced robustness. The surface chemical property of the structured surface can be tailored to induce complete wetting of a specific liquid. In addition, the structured surfaces can be manufactured through a variety of soft-lithography approaches that are reported in the literature[5,142]. In particular, two novel features of our enhanced security features are the use of three-dimensional flexible nanostructures, as well as the utilization of ordinary liquids, such as alcohols and water (e.g., vapors from breath), for enhanced visualization of the anti-counterfeiting features. The security features we developed can be used either independently or in combinations to maximize the anti-counterfeiting effects.

The unique security features of our development can be broadly applied to general polymer-based security documents, particularly banknotes, credit cards, traveler's checks, and personal identification documents, such as passport and drivers licenses. In addition, these features can be also used in packaging and labeling industries, where anti-counterfeiting for products is necessary. Owing to the simplicity and the multi-functional nature of our approach, we anticipate that our surface can find various applications.

# Chapter 8 Electron-Beam Induced Assembly

In chapter 8, we have studied interaction of fiber arrays with electron-beam. Besides evaporating liquids, the fiber arrays show responsive behaviors when exposed to electron-beam. We studied movement of fiber arrays under electron-beam and developed a model that explains the behavior of fiber arrays when they interact with electron-beam. Based on the model, we demonstrated localized patterning of pseudo three-dimensional structures using electron beam. This chapter is based on our published paper (ref. 4). The content is used with permission from American Physical Society.

## 8.1. Introduction

Electron beams are widely used as a tool for characterizing the microstructure and composition of materials, with techniques ranging from low-energy electron diffraction to reflection high-energy electron diffraction, transmission electron microscopy, scanning electron microscopy (SEM), etc. In this process, the electron beam interacting with the matter results in the emission of backscattered and secondary electrons as well as electromagnetic radiation[143]. In many cases, the major portion of the injected charge remains in the material and yields

undesirable effects: it alters the properties of materials, causes movement of the specimen, and leads to artifacts. An e-beam-induced feature displacement has been reported for decades and has been considered as a limiting factor both for obtaining high-resolution images[144] as well as in e-beam writing. There have been only a few studies attempting to investigate the mechanism of the movement; these include photolytically initiated solid-state chemical reactions generating pressures inside the structures[145], shrinkage of surfaces[146], and surface charging on thin films with one conducting layer[147]. In this chapter, we propose an electrostatic model that explains feature movement and provides the basis for an unconventional, dynamic patterning technique.

## 8.2. Experimental observations

To systematically study e-beam-induced motion of surface nanofeatures, we fabricated arrays of cylindrical nanofiber of height H and radius r (see Figure 47a) from epoxy resin using soft lithography[5]. The nanofibers are attached to a supporting surface made of the same material. The samples were then sputter-coated with a 5–10-nm layer of gold or carbon, placed in a SEM and grounded. A Cressington 208 HR sputter coater and a Baltech CED 030 carbon arc coater were used for gold and carbon coating. Imaging was performed with a Zeiss Ultra 55 field-emission scanning electron microscope at Harvard Center for Nanoscale Systems. We chose high-aspect-ratio polymeric nanofibers because relatively low forces are needed to move these

structures[148]. When the nanotextured surface was imaged for a few seconds in the SEM at high magnification, we observed bending of the nanofibers, as shown in Figure 47b. The movement pattern presents three characteristic features: (i) nanofibers near the center of the scanned region show negligible movement; (ii) maximum bending occurs at the perimeter of the scanning window; (iii) all nanofibers are bent toward the center of the scanning window. The pattern is reproducible and persists over several seconds before the nanofibers relax back to the original position, as shown by imaging a larger area. We repeated the experiment at different beam energies (1–30 KeV) and beam currents (10–150 pA). Lateral movement increases with increasing current, but surprisingly, it does not increase monotonically with beam energy: maximum bending is recorded at 5 KeV, after which the displacement decreases.

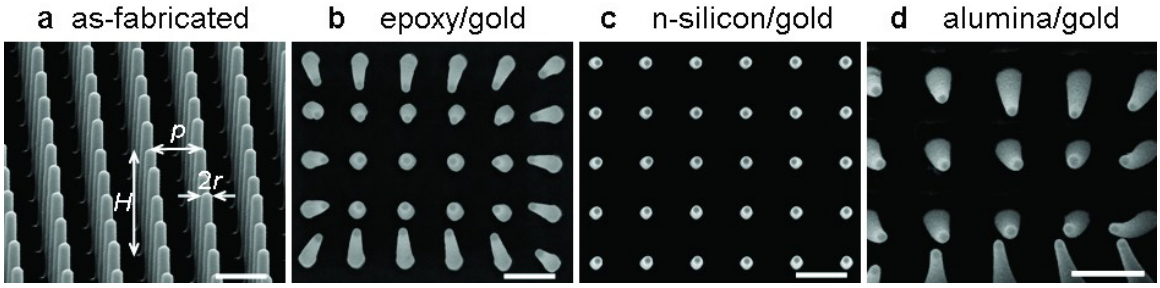


Figure 47. Scanning electron microscope (SEM) images of samples show a reproducible movement pattern. (a) As-fabricated nanofiber array with $H$ = 8 μm, $r$ = 0.125 μm, $p$ = 2 μm. (b) Gold-coated epoxy nanofiber arrays after ~1 to 5 s scanning. (c) Gold-coated silicon nanoposts arrays after ~10 to 15 s scanning. (d) Gold-coated alumina nanofiber arrays after ~10 to 15 s scanning. Scale bars 2 μm. Reprinted from ref. 4 with permission from American Physical Society.

Nanofiber bending strongly depends on the properties of the material, as summarized in

Table 1. Doped n-type silicon nanofiber arrays with identical geometries showed no movement (Figure 47c). To determine whether the arrested movement results from the 20-fold increase in the bending stiffness of silicon over epoxy, we fabricated the same structures in alumina using atomic layer deposition. Although the bending stiffness of alumina is even higher than that of silicon, under the e-beam, alumina nanofibers underwent pronounced bending (Figure 47d). This rules out the hypothesis that silicon is too stiff to bend. Instead, because alumina is an electrical insulator, the experiments suggest that electrostatic interaction is responsible for bending.

Table 1. Material properties and the result of the experiment for different materials. Reprinted from ref. 4 with permission from American Physical Society.

| Material | Relative permittivity $\varepsilon_r$ | Bending modulus E (GPa) | Conductivity K ($\Omega^{-1}m^{-1}$) | Relaxation time scale $\tau$ (s) | Bending |
|---|---|---|---|---|---|
| epoxy | 2.3 | 2 | $\leq 10^{-11}$ | $\geq 2$ | Yes |
| silicon | 11.7 | 100 | $10^{-4}$ | $10^{-8}$ | No |
| alumina | 9.6 | 300 | $\leq 10^{-12}$ | 80 | Yes |

## 8.3. Theoretical model for the implanted charge

We thus propose an electrostatic model of nanofiber bending based on a two-step process: first, electrons from the e-beam are implanted in the nanofibers as a result of backscattering; second, charging and induction produce an electric field inside the specimen, and the ensuing electrostatic forces and torques deflect the nanofibers. With this simple model, we obtain a

deflection of the nanofiber consistent with the experiments

performed on isolated nanofibers in spot mode, and we can simply extend the prediction to nanofiber arrays in scanning mode. We first compute the magnitude of the implanted charge with a combination of theoretical arguments and Monte Carlo simulations. Simple considerations backed up by numerical simulations suggest that this implanted charge is not distributed homogeneously in the nanofiber. The detailed charge distribution cannot be found by current experiments or simulations, so the theory we present has one free parameter, the center of the charge distribution. We then solve the electrostatic equilibrium problem coupled to the mechanical bending to obtain nanofiber deflections in the same range as experiments.

Whenever the electron beam scans the sample, a portion of the electrons is implanted in the nearby nanofibers. For simplicity, let us consider the case of a single nanofiber, with the electron beam in spot mode at a distance $a$ from the nanofiber, as sketched in Figure 48a. After the electron beam (with incoming current $i$) impacts the specimen, electrons are backscattered, with a backscattering coefficient $\eta$. Electrons backscatter at an angle $\theta$ relative to the beam direction with probability $P(\theta) = \cos\theta$ (see, e.g., Ref. 143). For a nanofiber radius $r$ and nanofiber-beam distance $a$, a fraction $r/(\pi a)$ of these electrons impact the nanofiber. Of these, a fraction $\eta_n$ are further backscattered and only $1 - \eta_n$ are implanted in the nanofiber, where $\eta_n$ is the backscattering coefficient at the nanofiber that depends on the angle of impact $\theta$, as discussed

below. The total current in per unit height impinging on the nanofiber at a distance $z$ from the substrate is, therefore,

$$i_n = \eta(1-\eta_n)\frac{r}{\pi a}P(z)i \tag{21}$$

where $P(z) = P(\theta)|d\theta/dz| = az/(a^2 + z^2)^{3/2}$. If $\lambda(z,t)$ is the charge per unit height deposited at a distance z from the substrate, the charge builds up according to $\dot{\lambda} = i_n - \lambda/\tau$, where $\tau \sim \varepsilon/K$ is the charge relaxation time (K is the conductivity and $\varepsilon = \varepsilon_0\varepsilon_r$ is the permittivity; see Table 1). In conditions of steady state, this yields

$$\lambda(z) = i_n(z)\tau \tag{22}$$

with $i_n$ given by equation (21). The contribution to forces and torques coming from longitudinal currents is estimated below and found to be largely negligible.

Note that the magnitude of $\lambda$ and the time scale over which this steady-state charge is set up vary dramatically with material properties (see Table 1). Note also that the escape depth of secondary electrons is a few nanometers, so that they are only emitted from the coating[149,150]. If the coating is grounded, charge induced by secondary emission flows rapidly to and from the ground until it reaches electrostatic equilibrium. At equilibrium, charge in the coating is determined solely by $\lambda$ through electrostatic induction, and secondary emission plays no role.

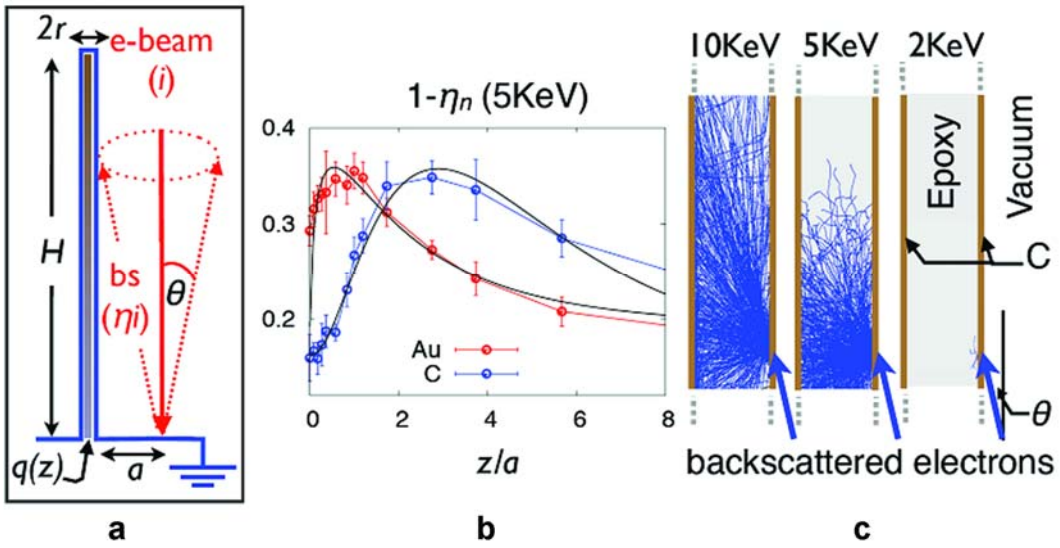


Figure 48. Monte Carlo simulations showing charge implanted in the nanofibers after backscattering. (a) Schematic geometry of the nanofiber: after the electron beam (current $i$) impacts the specimen, electrons are backscattered, with backscattering coefficient $\eta$ and backscattering angles $\theta$. (b) Implanted charge coefficient $1 - \eta_n$ in the nanofiber as a function of $z$ at $E_B = 5$ KeV obtained through Monte Carlo simulations of electron trajectories using an electron flight simulator available from Ted Pella, Inc. The black lines show phenomenological fits for gold-coated samples and for carbon-coated samples, used in the simulations of nanofiber bending. Error bars represent the standard deviation calculated from six different realizations of 3000 trajectories. (c) Simulated trajectories of electrons impacting the nanofiber at $\theta = 30°$ for different energies (2 KeV right, 10 KeV left). The trajectories of high-energy electrons are straight lines indicating that they travel through the nanofiber and leave the sample (left panel). Electrons at 2 KeV do not have enough energy to penetrate the nanofiber (right panel). Optimal implant energy is intermediate. We have no access to the details of the charge distribution. Reprinted from ref. 4 with permission from American Physical Society.

## 8.4. Monte Carlo simulations

To quantitatively evaluate $\lambda(z)$, we obtain the backscattering coefficients $\eta$, $\eta_n$ through Monte Carlo simulations of electron trajectories using an electron flight simulator available from Ted Pella, Inc. (see Figure 48b). The simulations directly provide the probability of

backscattering as the fraction of electrons that backscatter and penetrate. We obtain the backscattering coefficient at primary impact $\eta$ by averaging over six simulations, and we repeat the same operation at each angle of impact $\theta$ to obtain the backscattering coefficient at impact with the nanofiber $\eta_n$. Note that we include in $\eta_n$ the total number of electrons that either backscatter at the impact with the nanofiber or travel through the nanofiber and leave the sample from the other side.

We investigate why maximum bending occurs at an intermediate energy by repeating the simulation at different energies of the beam. In fact, depending on their energy, the electrons travel different depths in the nanofiber: at energies below ~2 KeV, the electrons do not even make it inside the nanofiber (Figure 48c, right), whereas at energies higher than ~10 KeV, electrons travel through the nanofibers and escape the sample, as suggested by the fact that most trajectories are straight lines in the left panel of Figure 48c. Maximum charge deposits in the nanofibers when electrons have enough energy to penetrate the nanofiber but not to escape it, which explains the presence of an intermediate optimal energy for nanofibers bending.

The simulations are not designed to provide detailed information on the trajectories of the electrons. However, the fact that there is an energy barrier $\Delta E \sim 2$ KeV associated with the interfaces suggests that the distribution of electrons is not uniform. Electrons that reach the outer interface with energy $< \Delta E$ are decelerated to rest before leaving the sample. We then

qualitatively expect that the charge distribution is biased toward the side of the nanofiber opposite to electron impact (the outer side). We parameterize these nonuniform distributions of $\lambda(z)$ by assuming that the charge is centered at a distance $x_c$ from the axis of the nanofiber. The detailed spatial distribution of the implanted electrons is beyond the scope of the present thesis, so $x_c$ is a free parameter of the model. We allow $x_c$ to be either positive or negative, corresponding to charge accumulating toward the inner or outer side of the nanofiber, i.e., the side of the nanofiber exposed or opposite to the e-beam. From the above arguments, we expect $x_c < 0$: the output of the model confirms this expectation, as discussed below. We remark that although charge is also implanted underneath the point of primary impact, our simulations show that its contribution to the bending forces acting on the nanofiber is negligible. (To make this point, we performed the complete numerical simulation adding a volume charge of $\eta i \tau$ at a depth of 1 μm underneath the point of primary impact in a spherical interaction volume of 0.5 $\mu m^3$. We obtained these values from Monte Carlo simulations.)

## 8.5. Theoretical model of electrostatically driven bending

We can now solve the electrostatic problem and obtain the force and torque inside the nanofiber produced by the uneven charge density $\lambda$ from equation (22) and $\eta$, $\eta_n$ from Monte

Carlo simulations. The equilibrium electrostatic potential φ is obtained by solving the Poisson equation,

$$\nabla^2\varphi = -\frac{\rho}{\varepsilon} \tag{23}$$

on the domain shown in Figure 49a. The implanted charge density $\rho(z)$ is distributed in a cylinder of cross section $l^2$ centered at a distance $x_c$ from the axis of the nanofiber (shaded area B in Figure 49b), so that $\rho = \lambda/l^2$. The electrostatic force (**w**) and torque (**N**) per unit length of the nanofiber can be computed from the action of the electric field $\mathbf{E} = -\nabla\varphi$ on the static charge $\rho$ and the induced surface charge $\sigma = \varepsilon E \cdot \hat{n}$, where $\hat{n}$ is the unit vector perpendicular to the coating:

$$N = \int_S \rho E \times x d^2x \tag{24}$$

$$w = \int_S \rho E d^2x + r(\sigma^{-1}E^{-1} + \sigma^{+1}E^{+1}) \tag{25}$$

*S* is the surface area of the nanofiber, *x* the distance from the center of the nanofiber, and the superscript + (−) denotes the side of the nanofiber exposed (opposite) to the e-beam. Given the force and torque acting on the nanofiber, we obtain nanofiber bending by solving the equation for small bending of a thin rod:[151]

$$\frac{\mathrm{dM}}{\mathrm{dz}} = -N - \hat{z} \times F \tag{26}$$

$$\frac{dF}{dz} = -w \tag{27}$$

where **F** is the shear force and **M** is the bending moment defined as $\mathbf{M} = -EI\partial_z^2\mathbf{u}$, $\mathbf{u} = \mathrm{u}\,\hat{x}$

is the displacement of the centerline, $I = \pi r^4/4$ is the area moment of inertia, and $E$ is Young's modulus.

The electrostatic force and torque computed through equations (24) and (25) are sufficient to bend epoxy nanofibers. Figure 49c and Figure 49d show the shape of a carbon-coated nanofiber at maximum bending and the maximum tip displacement as a function of $x_c$ for both carbon- and gold-coated samples, computed through finite-element simulations. The calculations predict that the nanofibers bend inward when $x_c < 0$, i.e., when charge accumulates toward the outer side of the nanofiber. We only observed inward bending for grounded samples, which implies that charge does, in fact, accumulate toward the side of the nanofiber opposite to the e-beam. This prediction accords well with the intuition exposed above that the energy barrier associated with the outer interface may serve as a bias of electron distribution.

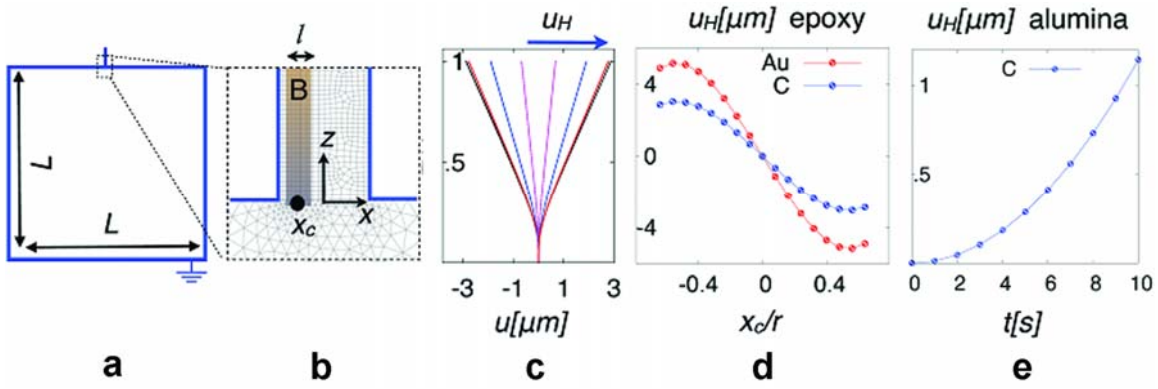


Figure 49. Finite-element simulations of equations (23)-(27) are carried out with COMSOL multiphysics on the two-dimensional domain shown in panel (a) [$\eta = 0.98$; beam current $i = 150$ pA; elastic modulus $E = 5$ GPa; beam energy $E_B = 5$ KeV; nanofiber-beam distance $a = 1$ μm; results do not depend sensibly on $L$ and $l$; we use $L = 0.1$ mm and $l = 0.05$ μm; $1 - \eta n$ is given by

the functions represented with black lines in Figure 48b]. Since the metal coating is grounded, the potential at all external boundaries is zero. (b) Magnification of the base of the nanofiber showing the variable triangular mesh in the substrate and square mesh on the nanofiber. The shaded area is charged with $\rho(z) = \lambda(z)/l^2$, where $\lambda$ is given by equation (22). We impose $u_{z=0} = u'_{z=0} = 0$ (the base of the nanofiber is clamped) and $M_{z=H} = -EIu''_{z=H} = \int_S \sigma E \times x d^2x$; $F_{z=H} = \int_S E\sigma d^2x$ at the tip. (c) Shape of a carbon-coated nanofibers at maximum bending for different values of $x_c$ between $-r$ (right) and $r$ (left). (d) Maximum displacement of the tip of the nanofiber as a function of $x_c$ for an epoxy specimen coated with carbon (blue) and gold (red).When charge accumulates in the outer part of the nanofiber, the nanofiber bends inward. (e) Tip displacement for alumina samples coated with carbon, for $x_c = -0.08$ μm, as a function of time. Reprinted from ref. 4 with permission from American Physical Society.

To help visualize the forces and torques bending the nanofiber, we show the electrostatic potential $\varphi$ for $x_c = -0.08$ μm in Figure 50a. The main contribution to nanofibers bending is provided by the vertical component of the electric field, whose average intensity in the charged portion of the nanofiber is shown in Figure 50b. The resulting force per unit length $F_z = \lambda E_z$, torque per unit length $N = x_c F_z$, and bending moment $\boldsymbol{M}$ from equation (26) are shown in Figure 50c–e. (Note that the interaction with the surface to which the nanofiber is attached provides the external forces needed for the center of mass to shift.)

Note that to reach the steady-state charge[144], current must flow to the ground until the amount of charge that is implanted in each portion of the nanofiber $i_n$ equals the amount of charge $\lambda/\tau$ that flows to the ground through the coating. We neglect the contribution to forces and torques originating from these longitudinal currents because they are largely smaller than the

static components. This is easily seen by estimating the current density flowing to the ground $J \leq i_n/\xi^2$, where $\xi$ is the thickness of the coating, generating an electric field $E_{||} \sim J/K$, where K is the conductivity of the coating. $E_{||}$ acts on the static charge $\lambda_{ind} \sim \lambda$ induced in the coating by the implanted charge $\lambda$, yielding a torque per unit height $T \sim \lambda_{ind} E_{||} r \approx 10^{-18}$ nN, where we have used the values of $r$, $a$, and $H$ in the caption of Figure 47; $K \approx 10^7 \Omega^{-1}$ m$^{-1}$, $\tau \approx 1$ s, and $i \approx 150$ pA. In fact, the torque originating from the static charge ranges from $N \sim 400$ nN close to the base of the nanofiber to about 1 nN at the tip (see Figure 50d), with an average of about 0.1 nN, so that we can largely neglect the contribution coming from these nonequilibrium effects.

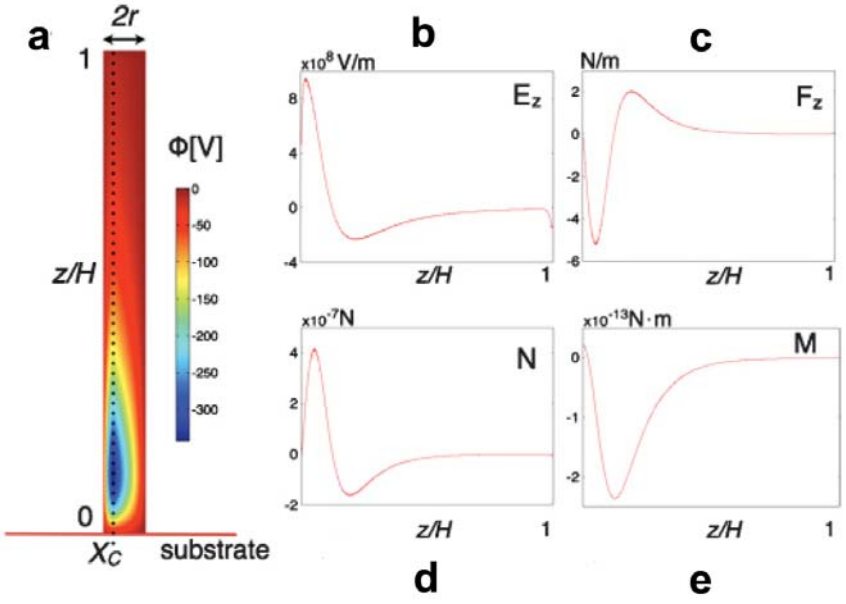


Figure 50. (a) Electrostatic potential $\varphi$ obtained by finite element simulations of equation (23) as described in the caption of Figure 49 for $x_c = -0.08$ μm. (b) Vertical electric field as a function of height, averaged over the charged portion of the nanofiber [region B in Figure 49b]: $E_z = -\langle \partial_z \phi \rangle$. (c) Resulting vertical force per unit height $F_z = E_z \lambda$. (d) Torque per unit height $N = x_c F_z$. (e) Bending moment resulting from equation (26). These electrostatic forces result from the presence of both implanted charge in the nanofiber and induced charge in the coating, and they

yield nanofiber bending, as shown in Figure 50c-Figure 50e. Reprinted from ref. 4 with permission from American Physical Society.

## 8.6. Comparison with experiments and application in patterning

The theory for the bending of a single nanofiber is sufficient to explain the patterns observed in scanning mode actuation shown in Figure 47b. Here the scanning is so rapid that charge distributes simultaneously over many nanofibers. Nanofibers on the edges are only exposed to the electron beam from the inside of the scanned area. Similar to the case of an isolated nanofiber, these electrons accumulate toward the outside of the nanofibers yielding maximum inward bending. Maximum displacement at the tip of these nanofibers is of ~1 μm, as seen from Figure 47b, which agrees well with our prediction for $x_c \sim 0.2$ μm (see Figure 49d). In contrast, symmetry breaking is washed out for nanofibers located near the center of the scanned region, since these receive about the same number of backscattered electrons from all directions. Here we expect $x_c \sim 0$ and no bending. The measured time scale of bending is a few seconds (see the caption of Figure 47), consistent with our theoretical estimate for $\tau = 2$ s.

The model also explains the behavior of silicon and alumina samples. Since the implanted charge is proportional to $\tau$ (equation (22)), and $\tau$ for doped-silicon is eight orders of magnitude smaller than for epoxy (Table 1), we predict negligible bending for silicon nanoposts, consistent

with the experimental observation shown in Figure 47c. For alumina, because of the long time scale for charge equilibration, $\tau \approx 80$ s, we assume that charge builds up linearly in time, and we perform a quasistatic analysis as a function of time. Figure 49e shows that the electrostatic force is strong enough to even bend alumina nanofibers. We predict that a 1 μm deflection of the tip, equivalent to deflection of epoxy nanofibers, is reached upon waiting for ≈10 s (see Figure 49e). This was experimentally verified, as shown in Figure 47d.

Further experiments corroborate the theoretical expectations. The theory shows that nanofiber actuation does not require interaction between nanofibers and an isolated nanofiber is expected to be deflected by the electron beam. In fact, we verify experimentally that if we focus the e-beam near an isolated nanofiber, the nanofiber bends toward the e-beam (Figure 51a). We can further validate this prediction by focusing the e-beam in the center of a nanofiber: in this case, where there is no symmetry breaking in electron distribution, we observe no bending (Figure 51b). Moreover, we expect that the direction of nanofiber deflection may be reversed. In all of the above arguments, we considered grounded samples for which charge in the coating is determined solely by electrostatic induction, as discussed above. However, if the ground is removed, the magnitude and sign of the charge in the coating should depend on secondary emission (SE)[152]. A switch in the sign of the charge in the coating may reverse the electric field inside the nanofiber, thus yielding outward bending. Direct numerical simulations of the

ungrounded case are not possible because they couple length scales that range from the nanometer to the millimeter. (Note that in the grounded case, the coating is simply modeled as a $V = 0$ surface, and because the electric field outside the sample vanishes, there is no need to resolve the details of electric-field variation inside the coating.) Although we have no access to the detailed charge distribution, we expect that materials with very different secondary yields may behave in opposite ways. In fact, upon removing the ground, the gold-coated samples (SE coefficient 0.7) show inward bending whereas carbon-coated samples (SE coefficient 0.05) show outward bending (Figure 51c and Figure 51d). Note that these results rule out the possibility that thermal expansion or electromagnetic forces are the mechanism causing bending.

In light of our findings and modeling, we believe that e-beam-induced nanofiber bending can be used as a powerful patterning technique. To demonstrate this technique, we fix the e-beam at one position between two or four nanofibers. Our model predicts that the backscattered electrons accumulate in the external part of each nanofiber and they all move independently toward the e-beam. (Grounding eliminates the electrostatic field outside the sample, so that the nanofibers only interact inside the material. Because of screening, this interaction is negligible, as confirmed by simulations.) Experiments confirm this prediction and additionally show that when the nanofiber tips come into contact, they ultimately stick to each other. (The mechanism for adhesion between the nanofiber is beyond the framework of the present study, but it is most

probably due to van der Waals interaction[2].)

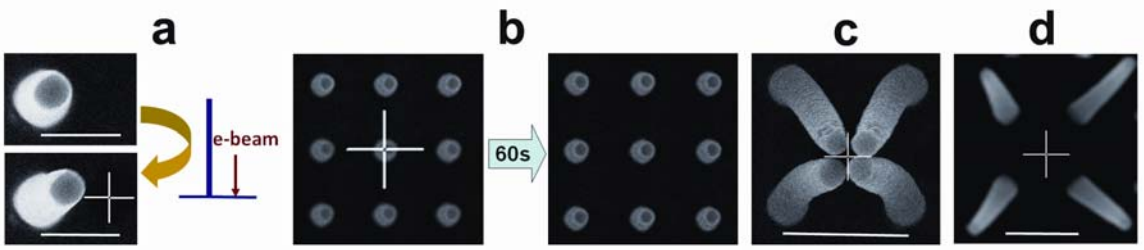


Figure 51. SEM images showing experimental tests of the proposed model. All samples are made of epoxy coated with gold and grounded (unless otherwise specified). (a) Position of a single nanofiber before (top) and after (bottom) exposure to the e-beam in spot mode. The position of the e-beam is marked with a white cross, and a schematic for the edge-on view is shown to the right. (b) Image of a sample before (left) and after (right) 60 s exposure to the e-beam in spot mode focused on the center of a single nanofiber. The position of the e-beam is marked with a cross. (c) Inward bending and tetramer formation upon focusing the e-beam in the center of four nanofibers coated with gold and disconnected from the ground. (d) Outward bending of four nanofibers coated with carbon and disconnected from the ground. Scale bars are 1 μm for (a), 2 μm for (c) and (d). Reprinted from ref. 4 with permission from American Physical Society.

Based on this result, we are able to perform larger-scale patterning or "writing" of clusters by repeated point (Figure 52a) or line (Figure 52b) scans. The strength of the proposed technique is that it can be done in any SEM, with no need or a special apparatus that, e.g., standard e-beam writing requires. Additionally, the minimum required voltage is about 4 KeV, which is a standard value, while e-beam writing techniques may require voltage as high as 90KeV. This minimum value can be further lowered by engineering properly the coating thickness and the material.

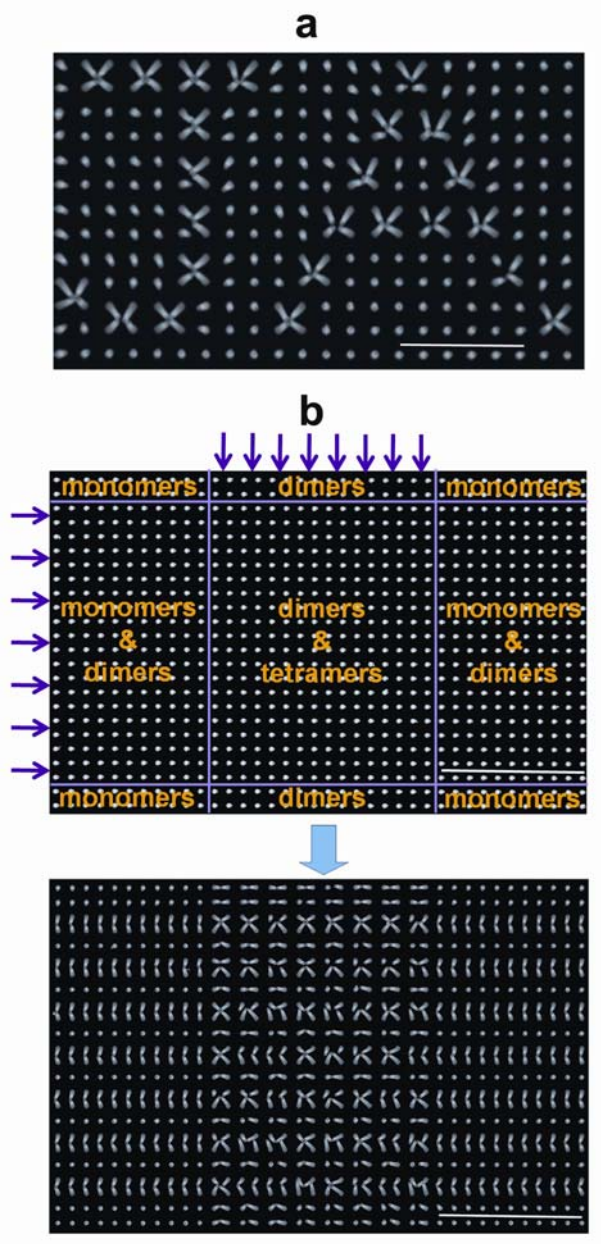


Figure 52. SEM images showing applications for patterning. The samples are made of epoxy coated with gold and grounded. (a) Writing of letters in nanofiber arrays through repeated exposure to the e-beam in spot mode. (b) Controlled patterning of the nanofiber array by seven horizontal line scans (skipping one row in between scans) and eight consecutive vertical scans, shown on the left micrograph. The first scan always produces dimers; an additional scan perpendicular to the existing dimers produces tetramers, shown in the micrograph on the right. Scale bars are 10 μm for (a) and 20 μm for (b). Reprinted from ref. 4 with permission from American Physical Society.

## 8.7. Summary

In summary, this work presents a study of the physical mechanism of e-beam-induced specimen movement and demonstrates how this process can be controlled to yield arbitrary arrays of surface clusters. Beyond fundamental physical insight, this new dynamic e-beam writing technique can prove useful for nanomechanical memories. By producing the arrays of nano- or micron-sized mechanical cantilevers[153] resilient to electromagnetic fields[154], one can potentially achieve data storage beyond superparamagnetic limits (100 $Gb/in^2$) with low-level power consumption.

# Chapter 9 Swelling-Induced Pattern Formation

In chapter 9, we studied pattern formation by swelling of structures. In previous chapters, we have demonstrated various ways of controlling pattern formation from fibrous surfaces. As discussed in chapters 4 and 5, isolated fiber arrays tend to generate patterns with no long-range order by interaction with evaporating liquids unless we control the shape or movement of the liquid-vapor interface. Moreover, the pattern formation is not reversible for many cases while reversibility is desirable for some applications so that one can dynamically control the properties of surfaces by manipulating pattern formation on surfaces. To address these issues, we have investigated swelling-induced pattern formation from interconnected cellular structures using rational design. This chapter is based on our work that we prepare for publication (ref. 155).

## 9.1. Introduction

Ever since Louis Pasteur discovered chirality by finding molecules whose mirror image are non-superimposable on their original configuration[156,157], this topic has been studied across many disciplines including mathematics[158], physics[159], chemistry[160], and biology[161]. This tremendous interest in chirality originates not only from its crucial role in controlling the behavior of living

and non-living systems, but is also spurred by the potential technological applications for chiral molecules and larger mesoscale chiral structures of single handedness[162]. Formation of chiral structures with uniform handedness typically requires either chiral induction[163] or spontaneous symmetry breaking. So far, spontaneous symmetry breaking has been reported only for a limited number of systems: at the molecular scale in autocatalytic chemical reactions[164] and crystallization systems[165] and at the mesoscale in centrosymmetric nanofiber arrays by evaporation-induced self-assembly as we described in chapter 2. Although at the molecular scale uniform handedness has been observed, the self-assembly at the mesoscale resulted in the formation of chiral clusters of randomly distributed left and right handedness[2]. The synthesis of mesoscale chiral structures of uniform handedness is thus still a fundamental challenge. In this chapter, by rational design based on modeling, we investigate a new phenomenon of controlled reversible switching between achiral and chiral configurations at multiple length scales using swelling/de-swelling of surface-attached cellular structures. We will show that the buckling pattern and the associated symmetry reduction of the initially achiral centrosymmetric structures could be tuned, simply by adjusting the aspect ratio of the individual plates. In the case of chiral transformations, spontaneous symmetry breaking can result in the formation of large uniform areas of structures of single handedness. This approach opens the way to select the appearance of either non-chiral, or chiral phases. The fundamental understanding of this process provides a

general route to designing deterministically deformable structures with dynamically switchable mechanical and/or optical properties.

## 9.2. Our approach

We exploit the use of mechanical instabilities to design a new class of structures that can be spontaneously switched between achiral and chiral configurations over large areas. Different from the previously mentioned systems[2,164,165], the underlying principle is scalable, so that it can be applied to generate patterns over a wide range of length-scales with potentially profound implications for many applications including optical filters[166] and sensors[167] and morphing airfoils[168]. We investigated the interconnectivity provided by periodic cellular structures consisting of 2D arrays of plates patched to fill a planar area and chose hexagonal cells as model systems. It is well-established that in these free-standing cellular structures buckling may occur[169], leading to dramatic changes of the structural geometry (see Figure 53). The generated deformations can be effectively transmitted through the system, yielding uniform patterns over large areas. However, these free-standing cellular structures cannot generate chiral configurations since the deformation induced by buckling is uniform in the direction perpendicular to the cells (see Figure 53) resulting in only the first mode buckling with non-chiral configuration.

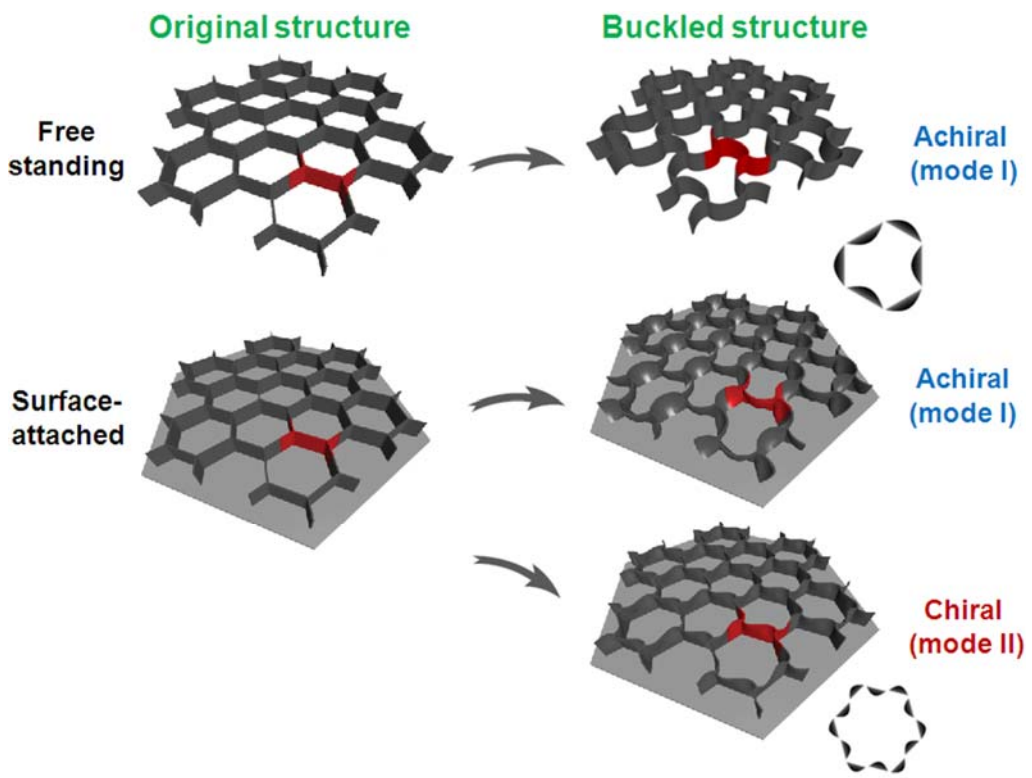


Figure 53. Schematic of our approach of generating chiral pattern from an achiral structure. The parts colored as red indicate the representative volume element of the structure, which is the minimum repeating unit to generate the structure.

To ensure an asymmetric deformation with respect to a plane parallel to the cells, we then proceeded by attaching one side of the structure to a plate. In the resulting surface-attached cellular structures, the pattern induced by buckling is clearly not uniform anymore in the direction perpendicular to the cells, but close inspection on the rotation of the vertices reveals that an equal mixture of clockwise and anti-clockwise rotations is formed, generating achiral configuration (planar group: p31m) if we consider the unit cell of the structure (see surface-attached, mode I in Figure 53). However, in clear contrast with the case of free-standing

cellular structures where buckling solely results in the emergence of a wavy pattern characterized by half wavelength per plate, at this point we can further take advantage of the constraint provided by the plate and trigger buckling modes characterized by shorter wavelengths. Surprisingly, a geometrical construction revealed that when the wavelength of the buckling mode is an integer number, all vertices in the structure rotate in the same direction, leading to the formation of a chiral pattern (planar group: p6) (see surface-attached, mode II in Figure 53).

Although the observation above clearly indicates that surface-attached cellular structures are promising systems to achieve spontaneous formation of chiral pattern of single handedness, the experimental proof of principle requires a careful geometrical design to fully control the formation of either achiral or chiral patterns. Therefore, we started by identifying the essential mechanical ingredients and then use a combination of analytical predictions, finite element (FE) simulations, and experiments to control switching between achiral and chiral configurations using initially centrosymmetric surface-attached lattice structures.

Among many mechanisms of triggering the instability, we chose swelling as actuation mechanism for its stimuli-responsive behavior and experimental convenience. We will first use analytical model for thin walls to construct a diagram that predicts the buckling pattern from initial cellular structures. Then, we will use numerical methods to consider thickness effects and to get design parameters for experimental verification. Because our model is independent of

scales, we will fabricate structures at both micro and macroscales and compare swelling patterns with our models. From our experiments, we also observed the effects of kinetics and will describe how we can manipulate the swelling kinetics to induce desired patterns.

## 9.3. Analytical model and buckling pattern diagram

To gain more insight into the response of surface-attached cellular structures, we start by investigating buckling of the individual cell edges consisting of rectangular plates of length $l$, height $h$ and thickness $t$ (see Figure 54a) subjected to isotropic swelling. For the sake of simplicity, we focus on thin plates, so that shear deformations through the thickness of the plate can be neglected, and consider a deformation that takes a point on the center-surface with coordinates ($x, y, 0$) to its deformed state $(x+u_x(x,y), y+u_y(x,y), w(x,y))$. Assuming that the thin plate may be described as a linear elastic material with Young's modulus $E$, Poisson's ratio ν, and bending stiffness $D= Et^3/[12(1-\nu^2)]$, then balance of forces in the plane and out of the plane leads to the Foppl-von Karman equations[170-172]

$$\sigma_{,ij} = 0\,, \quad \nabla^4 w - t w_{,ij}\sigma_{,ij} = 0\,, \; i,j = x,y, \qquad (28)$$

where $A_{,x} = \partial A / \partial x$ and $\nabla^4 A = A_{,xxxx} + A_{,yyyy} + 2A_{,xxyy}$. Assuming isotropic swelling, the in-plane stresses are given by

$$\sigma_{ij} = \frac{E}{1+\nu}(\varepsilon_{ij} + \frac{\nu}{1-\nu}\varepsilon_{\gamma\gamma}\delta_{ij}) - \frac{E}{1-\nu}\varepsilon_{sw}\delta_{ij} \qquad (29)$$

where $\delta_{ij}$ is the Kronecker delta, $\varepsilon_{ij} = \frac{1}{2}(u_{i,j} + u_{j,i}) + \frac{1}{2}w_{,i}w_{,j}$ is the in-plane strain tensor and $\varepsilon_{sw}$ denotes the strain caused by swelling of the material.

### 9.3.1. Boundary conditions

In a 2D cellular structure attached to a substrate that is very stiff and swells by a negligible amount, clamped conditions can be assumed for each individual cell edge at *y=0*,

$$u_x(x,0) = u_y(x,0) = w(x,0) = w_{,y}(x,0) = 0 \qquad (30)$$

while the condition that the boundary at *y=h* is free of torques and forces implies that

$$\sigma_{yy}(x,h) = \sigma_{xy}(x,h) = 0, w_{,yy}(x,h) + \nu w_{,xx}(x,h) = w_{,yyy}(x,h) + (2-\nu)w_{,xxy}(x,h) = 0 \qquad (31)$$

Finally, in a lattice where the junctions cannot move but are free to rotate for each plate the boundary conditions at *x=0, l* read

$$u_x(x,y) = w(x,y) = w_{,x}(x,y) = 0, w_{,xx}(x,y) + \nu w_{,yy}(x,h) = 0 \qquad (32)$$

### 9.3.2. Buckling

We start by noting that equations (28)-(32) are satisfied when

$$u_x^0(x,y) = w(x,y) = 0, u_y^0(x,y) = \varepsilon_{SW}(1+\nu)y \qquad (33)$$

resulting in uniform strain and stresses and zero deflection. However, this solution is not always stable and above a critical value of swelling $\varepsilon_{sw}^{cr}$ non-planar solutions appear. To test the stability of the solution of equation (33), we introduce incremental deformations as follows

$$u_i(x,y) = u_i^0(x,y) + \varepsilon u_i^1(x,y), w(x,y) = w^0(x,y) + \varepsilon w^1(x,y) \qquad (34)$$

where $\varepsilon$ is a small parameter that characterizes the size of the perturbation superimposed on the finite deformation. Inserting equation (34) into equation (28) and retaining only the first order terms in $\varepsilon$, a single non-trivial incremental equilibrium equation is obtained

$$w_{,xxxx}^{(1)} + 2w_{,xxyy}^{(1)} + w_{,yyyy}^{(1)} - \frac{Et\varepsilon_{SW}}{D} w_{.xx}^{(1)} = 0 \qquad (35)$$

Assuming the out-of-plane deflection is of the form $w^{(1)}(x,y) = f(y)\sin\frac{m\pi x}{l}$ ($m$ being an integer) on substituting it into equation (35) and using the boundary conditions (30)-(32), an eigenvalue problem is obtained. We solve this boundary value problem numerically and study the normalized critical load $k_m^{cr} = \frac{Et^2\varepsilon_{sw}^{cr}}{\pi^2 D}$ and corresponding buckling modes as a function of the plate aspect ratio *l/h*, as shown in Figure 54a. It is interesting to observe that higher buckling modes (i.e. *m*>1) can be achieved for increasing values of *l/h*. By contrast, we notice that for a plate with free edges both at y=0 and y=*h* only modes with half wavelength (i.e. *m*=1) are

possible.

### 9.3.3. Buckled pattern of surface-attached cellular structures

The results obtained for the individual cell walls can be now used to predict the buckled pattern of surface-attached cellular structures constructed by an assembly of these walls. The buckling pattern for a hexagonal lattice can be easily reconstructed from the individual cell walls as shown in Figure 54a, by preserving the angle at the vertices of the connected plates. Remarkably, by simply changing the aspect ratio of the individual cell walls, the reconstruction leads to either achiral or chiral configurations. For $l/h<2.32$, a surface-attached honeycomb underwent spontaneous symmetry reduction resulting in an achiral structure (Figure 54b). By contrast, a chiral structure appears by symmetry breaking when $2.32<l/h<4.02$ (Figure 54b).

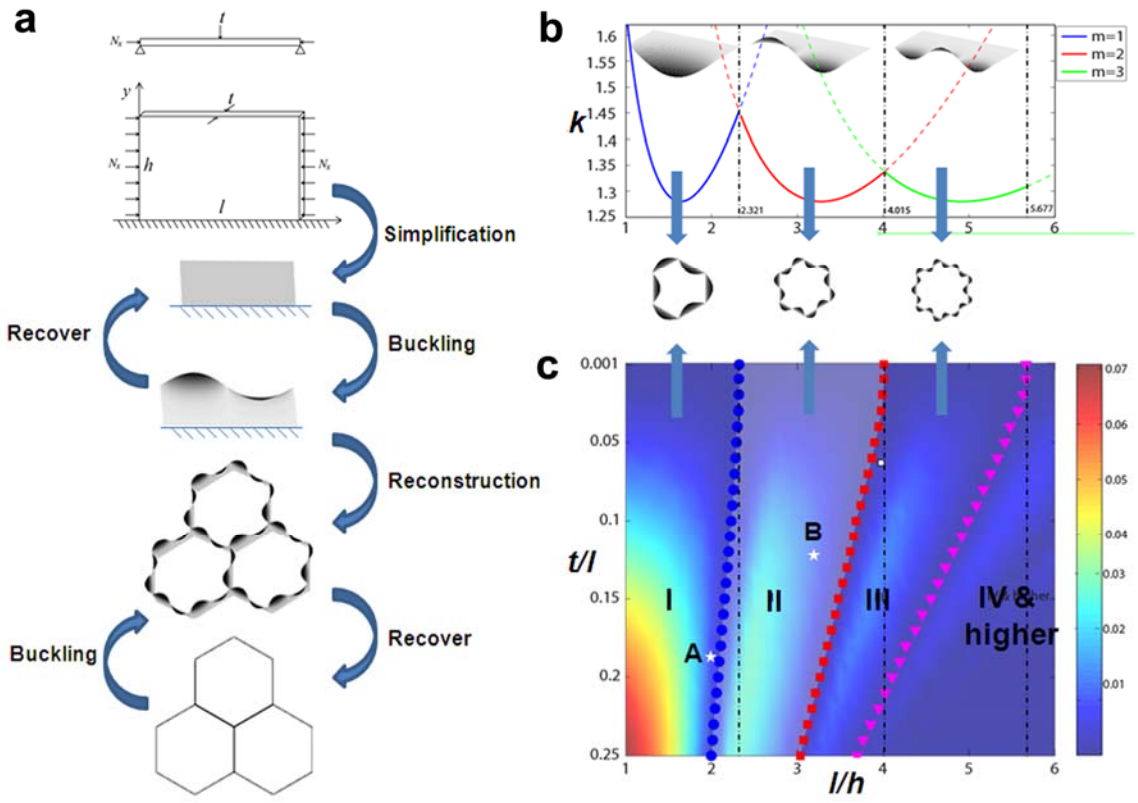


Figure 54. (a) Schematic of a single cell wall used for reconstructing the buckled honeycomb structures. (b) Analytical solution showing different buckling modes can appear by changing the dimensions of the honeycomb. (c) A contour diagram showing the difference in eigenvalues between neighboring modes based on the geometry of the wall. The "phase" diagram shows different buckling modes we can have depending on the geometry of the wall.

## 9.4. Numerical model for optimization of the dimension

To fully define the design space for experiments, we then proceed by incorporating the effect of thickness and further investigate the buckling of surface-attached lattice structures using non-linear finite element (FE) analyses. Buckling of structures of infinite planar extent perfectly bonded to a rigid substrate was simulated, assuming isotropic swelling. Although instabilities might alter the periodicity of the infinite solid, here they can still be investigated on the same

primitive cell through a Bloch wave analysis, a staple of physics long used to examine electronic, photonic and phononic band structures in periodic lattices[173,174]. For surface-attached honeycomb structures, we performed a series of FE simulations on the design parameters <*l/h, t/l*> and the corresponding results are presented in Figure 54c as a contour "phase" diagram. In this diagram, the color represents the difference in eigenvalues of two neighboring states. The larger the difference, the better to get the desired buckling pattern. Otherwise, different buckling modes can coexist due to small difference in energy. As predicted by our analytical model, alternating achiral and chiral domains were found along the *l/h* axis by buckling. For structures with thin walls (i.e. $t/l \to 0$), the transition between chiral and achiral domains was found to be in excellent agreement with the analytical model. Moreover, an increase in *t/l* affected only moderately the boundary of the domains. The numerical simulations thus confirm that by simply controlling the aspect ratio of surface-attached cellular structure in initially achiral honeycomb structure, either achiral or chiral configurations can be formed. Importantly, these buckling-induced patterns are independent of the material properties and have no characteristic length scale, indicating that this phenomenon may be applicable across a wide range of length scales and materials. We could therefore straightforwardly test our theory in any scale within the regime of continuum mechanics.

## 9.5. Experimental demonstration of a large area chiral structure with uniform handedness

To verify the predictions of our analytical and numerical models, we fabricated surface-attached macro honeycombs characterized by $<l_A/h_A,\ t_A/l_A>$ = <2, 0.185> and $<l_B/h_B,\ t_B/l_B>$ = <3.17, 0.125>, as indicated by the star shape markers in Figure 54c. According to the phase diagram presented in Figure 54c, we expect the formation of achiral pattern for structure A and a chiral one for structure B. The macroscopic honeycomb structures were fabricated by first printing a negative mold using a 3D printer (available from Objet) and replicate the positive structure in silicone (Elite 32 from Zhermack). The swelling experiment can be conducted using various solvents. In our case, we used hexane (available from Sigma Aldrich) considering its swelling capability and the evaporation rate.

Starting from the original honeycomb structure shown in Figure 55a, we observed formation of achiral structure (Figure 55b) by buckling for the structure A as we applied hexane onto the original structure. The experiment thus demonstrated that the constrained interconnected walls indeed buckled upon applying of stress in a configuration that was predicted from the modeling. Next, we tested structure B and, as predicted by the model, we found that the initial centrosymmetric honeycomb structure spontaneously transformed to large areas of the second mode buckled chiral structures upon swelling. The simple swelling induced-buckling not only

forced the formation of chiral structures, but also spontaneously yielded large areas of single chirality. For both structures, if we subsequently deswelled the buckled structure by drying of the solvent, it reconverted into the original honeycomb, which shows that the pattern formation can be reversible. In addition, we found that more uniform pattern was formed as the difference in the eigenvalues increases. For example, for the geometry in the region II of the Figure 55c, if the eigenvalue difference was small, achiral and chiral structures coexisted in one sample, which is in agreement with the trend predicted from the simulation result.

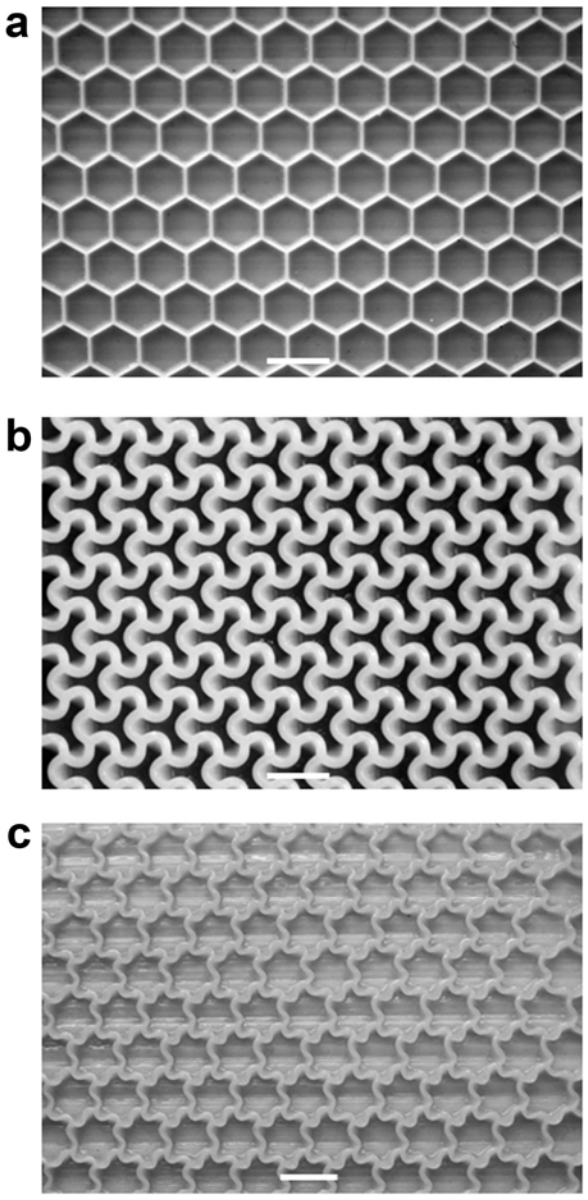


Figure 55. Images of the honeycomb structures (a) before swelling, (b) with the first mode buckling, and (c) with the second mode buckling. The second mode buckling case is chiral. The scale bars are 1 cm.

## 9.6. Expansion of the model to different lattices and length scales

Our model can be also extended to different lattices because we can reconstruct lattices by connecting walls. We have fabricated macroscale square (four connections) and triangular (six connections) lattices using the same method described above and conducted swelling experiments. The results showed good agreement with the prediction from the Figure 54 as shown in Figure 56. We could get both achiral (Figure 56c and Figure 56d) and chiral (Figure 56e and Figure 56f) structures from the initial square (Figure 56a) and triangular (Figure 56b) structures. Among the generated patterns, the first mode buckling pattern of the triangular lattice showed a complex pattern with no long range order because of geometric frustration[175]. In this case, the unique nature of the triangular lattice does not allow all three half waves form antiparallel to its neighbors so they become frustrated and generate many degenerate states as shown in Figure 57. The Fast Fourier Transformation of the original frustrated pattern shows an interesting six fold pattern different from the triangular lattice before swelling.

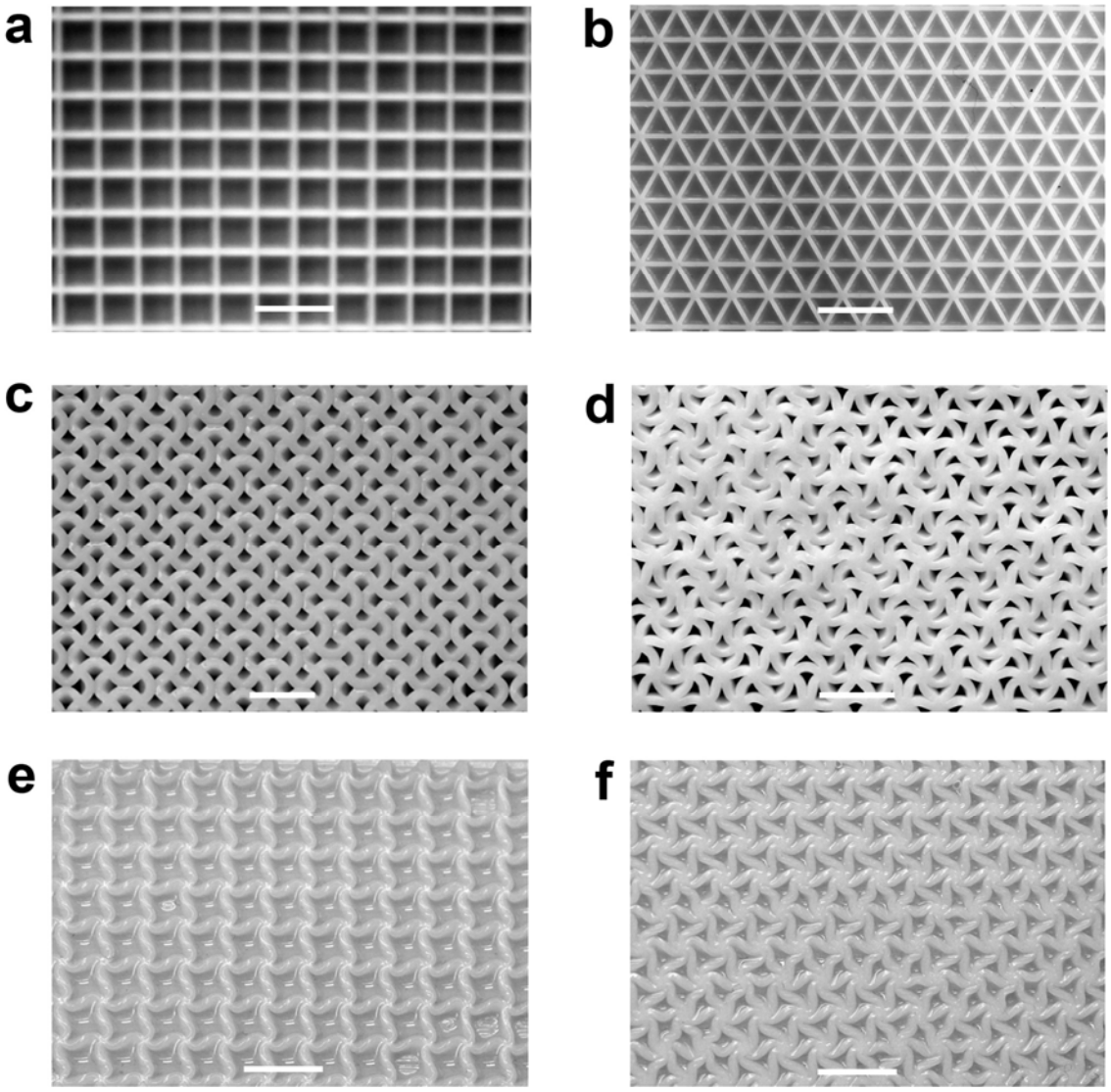


Figure 56. The initial (a, b), the first mode (c, d), and the second mode (e, f) buckling images of the square (a, c, e) and the triangular (b, d, f) lattices. The scale bars are 1 cm for all images.

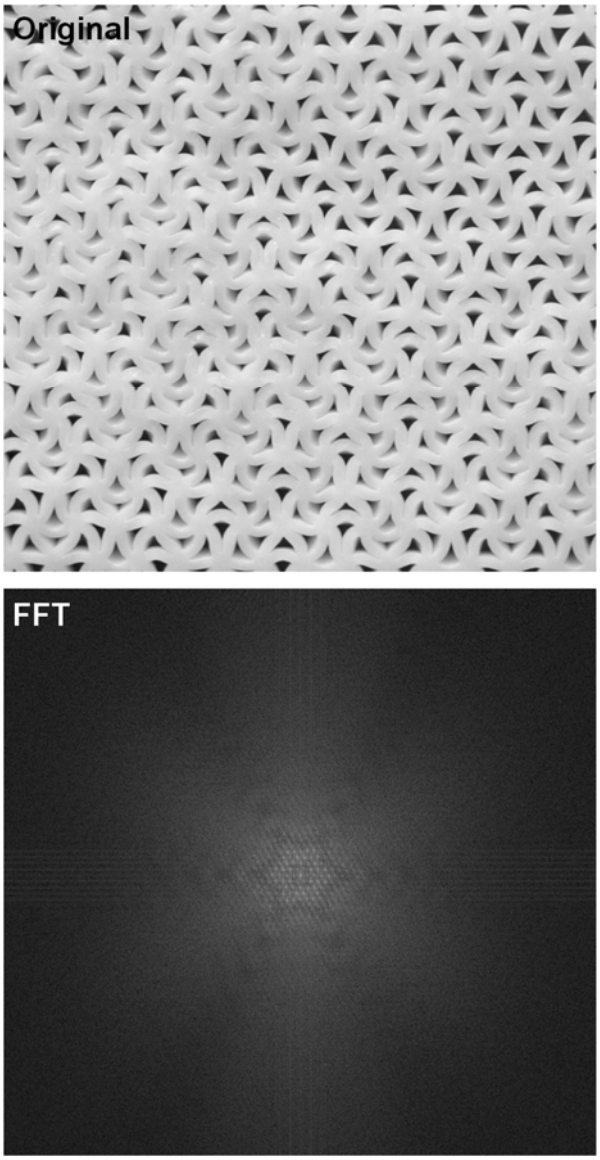


Figure 57. The original (top) and Fast Fourier-Transformed (FFT) image (bottom) of a geometrically frustrated buckling pattern for the triangular lattice case.

Moreover, we tested the scale independence of our model by fabricating silicon micro honeycomb structures using photolithography and replicating in UV curable epoxy for swelling experiments. We performed swelling experiments by immersing epoxy structures in a *N*-Methyl-2-pyrrolidone (NMP) solution, which is known to induce swelling of epoxy[176]. As

shown in Figure 58, the generated structures showed good agreement with the predicted buckling patterns from a numerical simulation (Figure 54). The above results thus demonstrate that we can precisely tune the appearance of achiral versus chiral patterns simply by tailoring the dimensions of the initial structures based on our model. Depending on the applications, we can choose a variety of scales for inducing patterns with controlled buckling modes. For example, we can consider further scale down the system so that the generated chiral structure shows different responses depending on the circular polarization of light.

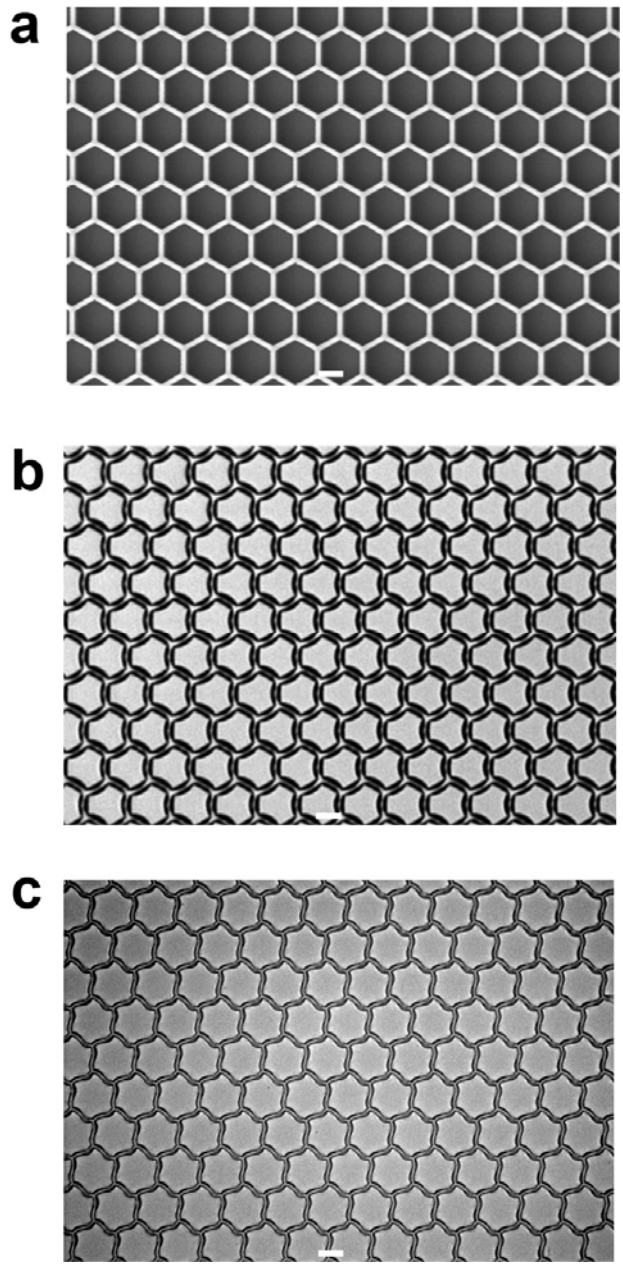


Figure 58. The initial (a), the first mode (b), and the second mode (c) buckling images of microhoneycombs. The scale bars are 20 μm.

## 9.7. Kinetics of pattern formation and chiral amplification

Besides equilibrium patterns, we also observed effects of kinetics. Due to the ease of manipulating the swelling process, we have used macroscale samples to understand the effects of kinetics in the swelling-induced pattern formation. In chapter 5, we discussed the importance of controlling the nucleation and propagation of the fiber assembly. Similarly, controlling the nucleation and propagation of the swelling-induced buckling is also important to form patterns with a long-range order. We did swelling experiments for two different cases. One was a fast swelling case, where an enough solvent covered the entire surface at the beginning. The other was a slow swelling case, where swelling happened at one unit cell and propagated in a coordinated manner by flowing a solvent with a controlled speed so that buckling could appear step by step. To control the flow rate, we used a syringe pump (Harvard Apparatus PHD 2000). The flow rate that we used was 0.1 mL/min – 0.4 mL/min, which corresponds to 15 sec/unit cell - 60 sec/unit cell for a hexagon with an empty volume of ~ 0.1 $cm^3$. In the case of a slow swelling, we made sure there was a single swelling site.

Interestingly, a uniform domain of single chirality was formed for slow swelling, but multiple domains of different chirality (Figure 59) for fast swelling in the case of the structures in the regime II. For the slow swelling case, we tried different locations on a substrate (corner,

center, etc.) as the starting point and found that a uniform domain can be formed as long as there is a single starting point for swelling and it propagates slowly.

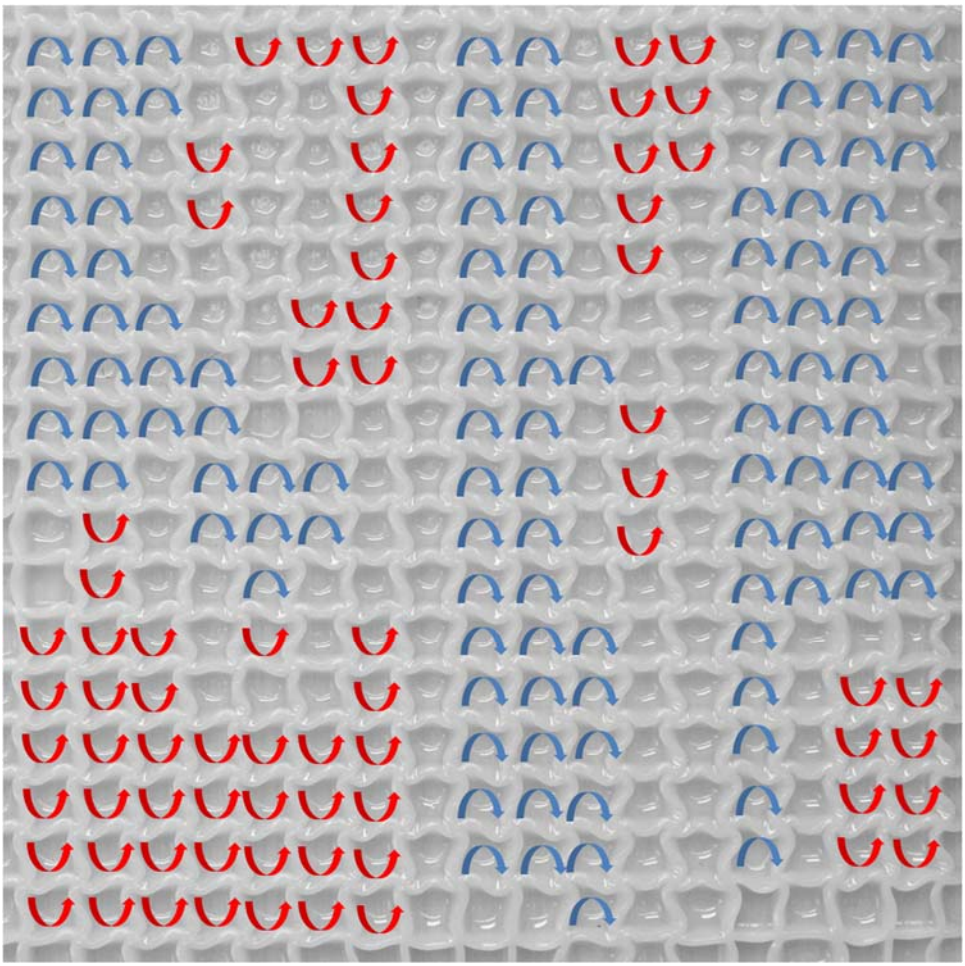

Figure 59. The buckling pattern generated from fast swelling of initially square structures. The arrows indicate the handedness of each unit cell. The unmarked regions correspond to domain boundaries where different buckling patterns were observed to accommodate domains with opposite handedness.

Moreover, we observed chiral amplification from slow swelling cases. We first obtained domains of different chirality from fast swelling for example, as Figure 59. Then, we started

swelling from one unit cell and observed whether the chirality of the seeding cell can guide the chirality of other parts of the sample. We found that the chiral seed can indeed lead to a large domain with a single chirality as a single crystal seed is used for growing a large single crystal. Interestingly, we also observed self-correction during the pattern formation process. As swelling patterns propagate, sometimes patterns of opposite chirality appear at the early stage of the swelling process then they switch the chirality as the neighboring cells swell and buckle.

In addition, we found that there is interesting memory effect. The structure has a memory of patterns formed during the swelling cycle. So, even though the drying of the swelled sample recovers the original honeycomb shape, if we apply a solvent again, it shows the same buckling pattern regardless of the swelling speed. Thus, by "writing" patterns using slow swelling, we can have the same pattern for repeating cycles. We can also erase the memory by using heat treatment. For example, if we put the dry sample in an oven at 70ºC for an hour, we can generate new buckling pattern from a swelling experiment followed by the erasing cycle. The observed phenomena are summarized as schematic in Figure 60. More study is needed to understand the molecular origin of this memory behavior, but we think it is probably related to the reorganization of polymer chains during swelling or erasing cycle.

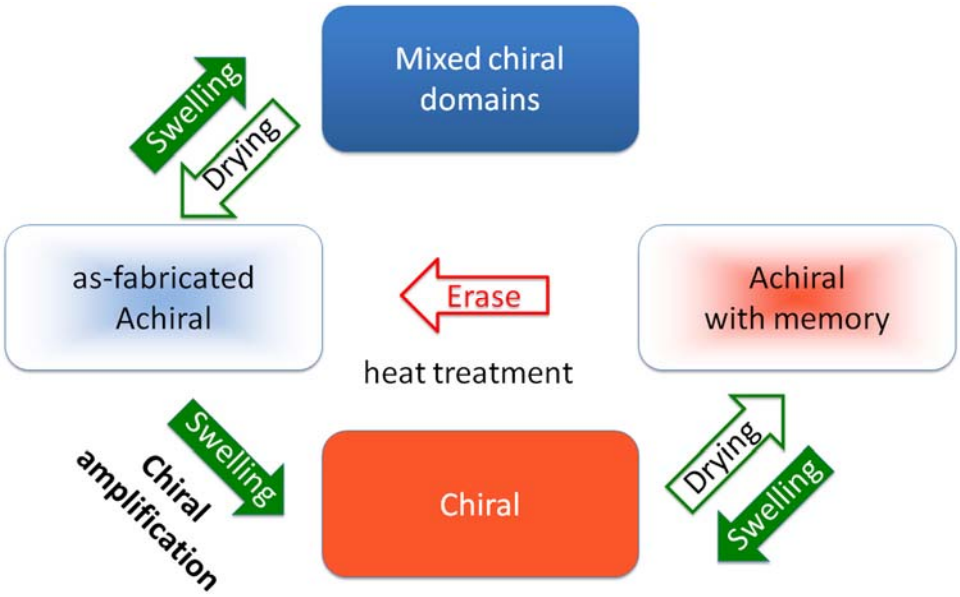


Figure 60. Possible routes of pattern formation.

## 9.8. Discussion

Our experiments demonstrate the emergence of single chirality at multiple length scales by symmetry breaking of carefully designed achiral architectures. While mechanical instabilities have been traditionally viewed as an undesirable phenomenon so most research focuses on avoiding them, we deliberately induce buckling to deterministically create structures of single handedness. Furthermore, the potential of chiral pattern formation in cellular structures has been unexplored though cellular structures have gained large scientific attention[169] as light-weight structures[177], novel electrode materials for lithium-ion batteries[178], fuel cell membranes[179], energy absorbers[180,181] and acoustic dampers[182]. Besides the fundamental relevance in the field of chirality, our results may also hold profound implications for practical applications due to

tunability of the system. We can control the appearance of achiral or chiral configuration by changing the aspect ratio of walls and the pattern formation can be reversible because we utilize elastic buckling. Therefore, our study provides opportunities for reversible switching over a wide range of length scales and opens avenues for the design of switchable optical devices. As we have demonstrated for three different lattices, a wealth of buckling patterns can be created by varying the number of walls that connect at the vertices. Additionally, to fix the cellular structure we hitherto used rigid solid substrates, but they can be substituted by perforated or flexible materials. The toolbox can be even further expanded since a wide range of construction materials and stimuli may be used to generate buckled architectures. For instance, polymeric gels are excellent candidates as construction materials since they are known to undergo large volume changes in response to stimuli such as variations in temperature[183], pH[184], osmotic pressure[185,186], electric field[187] or light[188]. The scalability of the dimensions, various geometrical designs and choice of construction materials can provide a versatile route to precisely tailor the architectures for practical applications ranging from controlled wetting[184,185] to phononic switching[183] and tunable optical gratings[186].

## 9.9. Summary

Processes that spontaneously break symmetry are of fundamental interest in the field of chirality. Although the emergence of asymmetry was demonstrated for molecules, this has remained a challenge in mesoscale systems and there has been no mechanism that works across multiple length scales. We have identified buckling of constrained cellular structures as a strategy for spontaneous symmetry breaking from our analytical calculations and numerical simulations. From our theoretical study, we found that the appearance of achiral or chiral patterns can be controlled by adjusting the aspect ratio of the cell walls. These fundamental insights guided an experimental demonstration using rationally designed structures. By swelling initially centrosymmetric structures, we observed that a cooperative buckling cascade resulted in configurations that were either achiral or chiral. In the latter case, buckling induced the transformation of the initially centrosymmetric architecture into chiral configurations of single handedness. Thus, our findings demonstrate spontaneous symmetry breaking at the multiple length scales. Moreover, we also report a new scale-independent chiral amplification mechanism based on buckling by controlling the kinetics of the buckling. Finally, we have outlined a general strategy in which the judicious customization of dimensions, materials, stimuli and architectonic designs unlocks the potential for a realm of practical applications ranging from switchable optics to controllable wetting.

# Chapter 10 Liquid-Infused Fibrous Surfaces

In chapter 10, we have studied exceptional liquid-repellent properties of liquid-infiltrated fibrous surfaces. When fibrous surfaces are infused with a lubricating liquid, the surfaces become slippery so that they can repel wide range of immiscible liquids and even solids. This chapter is based on our published paper (ref. 3) and the content is used with permission from Nature Publishing Group.

## 10.1. Challenges of current liquid-repellency technology

The cutting edge in development of synthetic liquid-repellent surfaces is currently inspired by the lotus effect[189]: water droplets are supported by surface textures on a composite solid–air interface that enables them to roll off easily[190,191]. However, this approach, while promising, suffers from inherent limitations that severely restrict its applicability. First, trapped air is a largely ineffective cushion against organic liquids or complex mixtures that, unlike water, have low surface tension, which strongly destabilizes suspended droplets[192]. Moreover, the air trapped within the texture cannot stand up to pressure, so that liquids, particularly those with low surface tension, can easily penetrate the texture under even slightly increased pressures or upon impact[193],

conditions commonly encountered with driving rain or in underground transport pipes. Furthermore, synthetic textured solids are prone to irreversible defects arising from mechanical damage and fabrication imperfections[194,195]: because each defect enhances the likelihood of the droplet pinning and sticking in place, textured surfaces are not only difficult to optimize for liquid mobility but inevitably stop working over time as irreparable damage accumulates. Recent progress in pushing these limits with increasingly complex structures and chemistries remains outweighed by substantial trade-offs in physical stability, optical properties, large-scale feasibility, and/or difficulty and expense of fabrication[41,42,196,197].

## 10.2. Synthetic slippery surfaces inspired by the Nepenthes pitcher plant

### 10.2.1. Inspiration from the Nepenthes pitcher plant

Nature, however, offers a remarkably simple alternative idea that is different from the lotus effect yet again capitalizes on microtextures: instead of using the structures to repel impinging liquids directly, systems such as the Nepenthes pitcher plant use them to lock-in an intermediary liquid that then acts by itself as the repellent surface[198]. Well-matched solid and liquid surface energies, combined with the microtextural roughness, create a highly stable state in which the

liquid fills the spaces within the texture and forms a continuous overlying film[199]. In pitcher plants, this film is aqueous and effective enough to cause insects that step on it to slide from the rim into the digestive juices at the bottom by repelling the oils on their feet[200].

### 10.2.2. Design principles of slippery surfaces

Inspired by this idea, we have developed synthetic liquid-repellent surfaces—which we name 'slippery liquid-infused porous surface(s)' (SLIPS)—that each consist of a film of lubricating liquid locked in place by a micro/nanoporous substrate (Figure 61). The premise for our design is that a liquid surface is intrinsically smooth and defect-free down to the molecular scale; provides immediate self-repair by wicking into damaged sites in the underlying substrate; is largely incompressible; and can be chosen to repel immiscible liquids of virtually any surface tension. We show that our SLIPS creates a smooth, stable interface that nearly eliminates pinning of the liquid contact line for both high- and low-surface-tension liquids, minimizes pressure-induced impalement into the porous structures, self-heals and retains its function following mechanical damage, and can be made optically transparent.

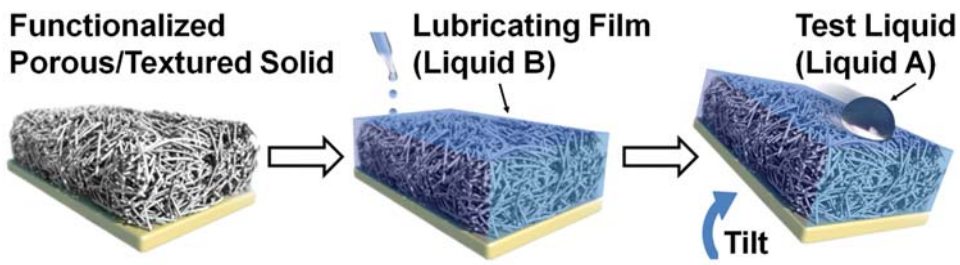


Figure 61. Schematics showing the fabrication of a SLIPS by infiltrating a functionalized porous/textured solid with a low-surface energy, chemically inert liquid to form a physically smooth and chemically homogeneous lubricating film on the surface of the substrate. Reprinted from ref. 3 with permission from Nature Publishing Group.

We designed the SLIPS based on three criteria: (1) the lubricating liquid must wick into, wet and stably adhere within the substrate, (2) the solid must be preferentially wetted by the lubricating liquid rather than by the liquid one wants to repel, and (3) the lubricating and impinging test liquids must be immiscible. The first requirement is satisfied by using micro/nanotextured, rough substrates whose large surface area, combined with chemical affinity for the liquid, facilitates complete wetting by, and adhesion of, the lubricating fluid (Figure 62)[136,201]. To satisfy the second criterion—the formation of a stable lubricating film that is not displaced by the test liquid (Figure 62 and Figure 63)—we determine the chemical and physical properties required for working combinations of substrates and lubricants as below.

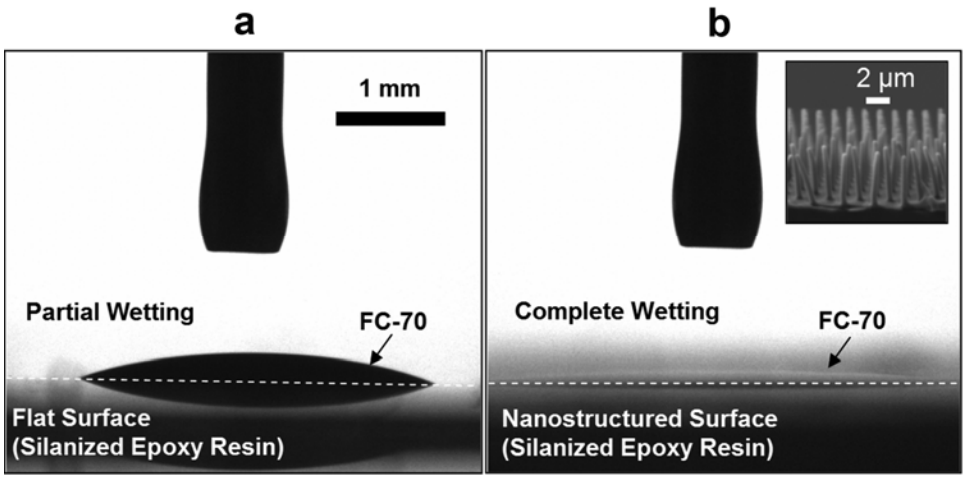


Figure 62. Wetting of perfluorinated fluids on flat and roughened surfaces. Optical images showing the wetting behaviors of a perfluorinated lubricating fluid, FC-70, on (a) a flat surface and (b) a nanostructured porous solid (inset shows an electron micrograph of the nanostructured surface). It is evident that the presence of the nanostructures greatly enhances wetting by the lubricating fluid, thereby forming a uniform and homogeneous coating on the porous solid. Reprinted from ref. 3 with permission from Nature Publishing Group.

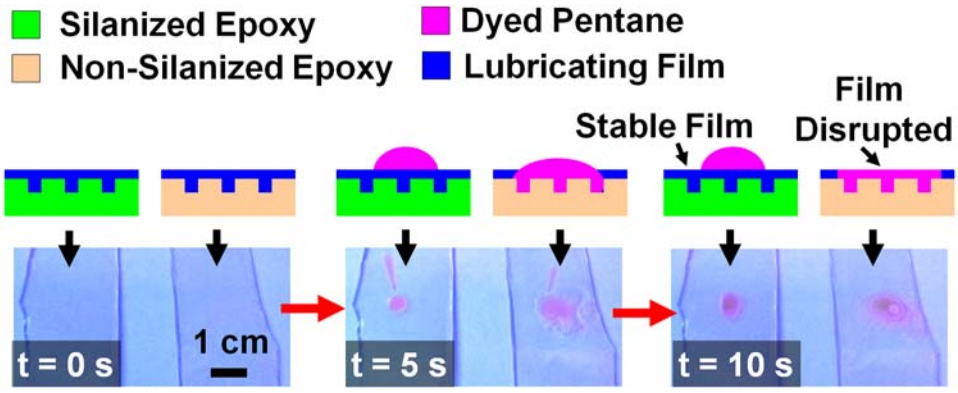


Figure 63. Comparison of the stability and displacement of lubricating films on silanized and non-silanized textured epoxy substrates. Top panels show schematic side views; bottom panels show time-lapse optical images of top views. Dyed pentane was used to enhance visibility. Reprinted from ref. 3 with permission from Nature Publishing Group.

An essential criterion for a functional SLIPS is that the solid must be preferentially wetted by the lubricating fluid (Liquid B) rather than by the liquid one wants to repel (Liquid A). This

ensures that Liquid A floats on top of a lubricating film of Liquid B. To determine whether a solid will be wetted preferentially by a Liquid A or Liquid B, we compare the total interfacial energy of the individual wetting configurations (Figure 64). Specifically, Configuration A refers to the state where the textured solid is completely wetted by Liquid A. Configurations 1 and 2 refer to the states where textured solids are completely wetted by Liquid B with and without a fully wetted Liquid A floating on top of it, respectively. The idea here is to find conditions such that Configuration A is always at a higher energy state than the other two configurations. By comparing the energy states of Configuration 1 and 2 with that of the Configuration A, one can determine the required solid/liquid combinations to form a stable film of Liquid B (i.e., the configuration with a lower total energy is the preferred wetting state).

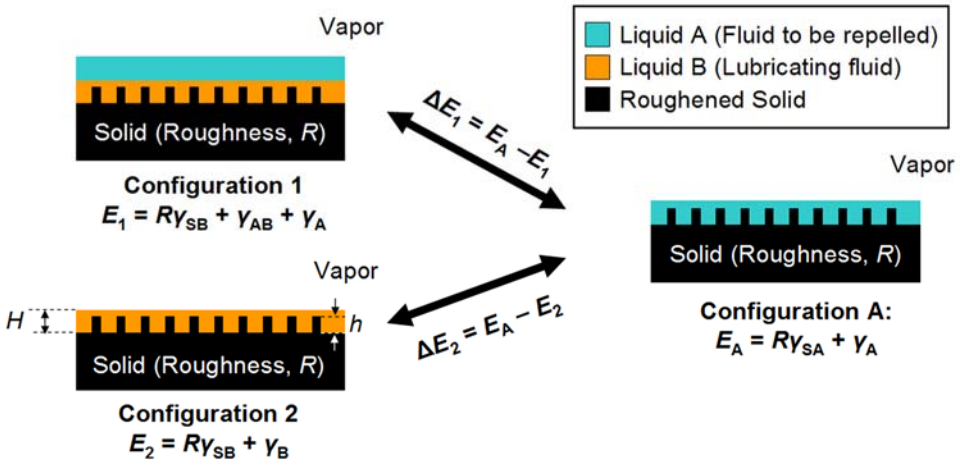


Figure 64. Derivation of the working conditions for maintaining a stable lubricating film. $E_1$, $E_2$, and $E_A$ represent the total interfacial energies per unit area of the wetting configurations 1, 2, and A, respectively. In addition, $\gamma_{AB}$, $\gamma_{SA}$, $\gamma_{SB}$, $\gamma_A$, and $\gamma_B$ represent the surface energies of the Liquid A-Liquid B interface, solid-Liquid A interface, solid-Liquid B interface, Liquid A-vapor interface, and Liquid B-vapor interface, respectively. H and h represent the thickness of the fluid layer and

the height of the surface textures, respectively. Also, R represents the roughness factor of the textured solid, which is defined as the ratio between the actual and projected areas of the surface. Reprinted from ref. 3 with permission from Nature Publishing Group.

To derive a working condition, the following assumptions are made: 1) the fluid layer covers the surface features (i.e., $H > h$); 2) the thickness of the fluid layer is much less than the capillary length of the fluid; 3) surface roughness is uniformly distributed for each configuration; 4) Liquid A and Liquid B are chemically non-reactive with the solid.

To find the conditions such that Configuration A is always at a higher energy state than Configuration 1, we have $E_A - E_1 > 0$, which can be further expressed as,

$$R(\gamma_{SA} - \gamma_{SB}) - \gamma_{AB} > 0 \qquad (36)$$

In particular, equation (36) is reduced to measurable quantities with the use of the Young-Dupré equation[20], where we have,

$$R[(\gamma_{SV} - \gamma_A \cos\theta_A) - (\gamma_{SV} - \gamma_B \cos\theta_B)] - \gamma_{AB} > 0 \qquad (37)$$

where $\gamma_{SV}$, $\theta_A$, and $\theta_B$ are the surface energy of the solid-vapor interface and the equilibrium contact angles of Liquid A and Liquid B on a flat solid surface, respectively.

By further reducing equation (37) into a more compact form, we have,

$$R(\gamma_B \cos\theta_B - \gamma_A \cos\theta_A) - \gamma_{AB} > 0 \qquad (38)$$

where we define $\Delta E_1 = R(\gamma_B \cos\theta_B - \gamma_A \cos\theta_A) - \gamma_{AB}$.

Similarly, to find the conditions such that Configuration A is always at a higher energy state than the Configuration 2, we have $E_A - E_2 > 0$, which can be further expressed as,

$$R(\gamma_B \cos\theta_B - \gamma_A \cos\theta_A) + \gamma_A - \gamma_B > 0 \qquad (39)$$

where we define $\Delta E_2 = R(\gamma_B \cos\theta_B - \gamma_A \cos\theta_A) + \gamma_A - \gamma_B$.

Satisfying both equations (38) and (39) will ensure a stable lubricated film formation. In contrast, when neither equations (38) and (39) are satisfied, Liquid B will be displaced by Liquid A. In the case where only one of the conditions is satisfied, Liquid B may or may not be displaced by Liquid A. To verify these design criteria, we explored a number of different solid/Liquid-A/Liquid-B combinations and compared these results with the governing relationships. We show that these relationships agree favorably with all of the experimental conditions in different scenarios (see Table 2).

Table 2. Comparison of the governing relationships with experimental observations for various solid-liquid-A-liquid-B combinations. "Y" indicates that Liquid B forms a stable lubricating film, and does not get displaced by Liquid A; whereas "N" indicates that Liquid B is displaced by Liquid A. The equilibrium angles, $\theta_A$ and $\theta_B$, are estimated from the respective averages of the measured advancing and receding angles on flat substrates from at least three individual measurements. $R$, $\gamma_A$, $\gamma_B$ represent the roughness factor of the substrate and the surface tensions of Liquid A and B, respectively. $\gamma_{AB}$ is estimated from the formulation: $\gamma_{AB} = \gamma_A + \gamma_B - 2(\gamma_A^d \gamma_B^d)^{1/2}$, where $\gamma_A^d$ and $\gamma_B^d$ are the dispersion force contributions of the liquid surface tensions[202,203]. The dispersion force contribution of water surface tension is 21.8 mN/m[202]. S. Epoxy represents silanized epoxy resin substrate. Alkanes are represented in $C_nH_{2n+2}$ where n = 5, 6, 8, 10, 13, and 16. Reprinted from ref. 3 with permission from Nature Publishing Group.

| Solid | Liquid A | Liquid B | R | $\gamma_A$ | $\gamma_B$ | $\gamma_{AB}$ | $\theta_A$ | $\theta_B$ | $\Delta E_1$ | $\Delta E_2$ | Stable Film? | |
|---|---|---|---|---|---|---|---|---|---|---|---|---|
| | | | | | | | | | | | Theory | Exp. |
| S. Epoxy | $H_2O$ | FC-70 | 2 | 72.6 | 17.1 | 51.0 | 104.9 | 11.8 | 19.6 | 126.1 | Y | Y |
| S. Epoxy | $C_{16}H_{34}$ | FC-70 | 2 | 27.2 | 17.1 | 1.2 | 63.1 | 11.8 | 7.8 | 19.0 | Y | Y |
| S. Epoxy | $C_{13}H_{28}$ | FC-70 | 2 | 25.9 | 17.1 | 0.9 | 60.5 | 11.8 | 7.0 | 16.7 | Y | Y |
| S. Epoxy | $C_{10}H_{22}$ | FC-70 | 2 | 23.6 | 17.1 | 0.5 | 52.3 | 11.8 | 4.1 | 11.1 | Y | Y |
| S. Epoxy | $C_8H_{18}$ | FC-70 | 2 | 21.4 | 17.1 | 0.2 | 40.8 | 11.8 | 0.8 | 5.4 | Y | Y |
| S. Epoxy | $C_6H_{14}$ | FC-70 | 2 | 18.6 | 17.1 | 0.0 | 37.7 | 11.8 | 4.0 | 5.5 | Y | Y |
| S. Epoxy | $C_5H_{12}$ | FC-70 | 2 | 17.2 | 17.1 | 0.0 | 26.7 | 11.8 | 2.8 | 2.9 | Y | Y |
| | | | | | | | | | | | | |
| Epoxy | $H_2O$ | FC-70 | 2 | 72.6 | 17.1 | 51.0 | 83.7 | 28.1 | -36.9 | 69.6 | Y/N | Y |
| Epoxy | $C_{16}H_{34}$ | FC-70 | 2 | 27.2 | 17.1 | 1.2 | 29.3 | 28.1 | -18.4 | -7.1 | N | N |
| Epoxy | $C_{13}H_{28}$ | FC-70 | 2 | 25.9 | 17.1 | 0.9 | 26.9 | 28.1 | -16.9 | -7.2 | N | N |
| Epoxy | $C_{10}H_{22}$ | FC-70 | 2 | 23.6 | 17.1 | 0.5 | 14.4 | 28.1 | -16.0 | -9.0 | N | N |
| Epoxy | $C_8H_{18}$ | FC-70 | 2 | 21.4 | 17.1 | 0.3 | <5 | 28.1 | -12.7 | -8.1 | N | N |
| Epoxy | $C_6H_{14}$ | FC-70 | 2 | 18.6 | 17.1 | 0.0 | 0 | 28.1 | -7.0 | -5.5 | N | N |

Table 2, Continued.

| | | | | | | | | | | | | |
|---|---|---|---|---|---|---|---|---|---|---|---|---|
| Epoxy | $C_5H_{12}$ | FC-70 | 2 | 17.2 | 17.1 | 0.0 | 0 | 28.1 | -4.2 | -4.1 | N | N |
| | | | | | | | | | | | | |
| Epoxy | $H_2O$ | FC-70 | 1 | 72.6 | 17.1 | 51.1 | 83.7 | 28.1 | -44.0 | 62.6 | Y/N | N |
| Epoxy | $C_{16}H_{34}$ | FC-70 | 1 | 27.2 | 17.1 | 1.2 | 29.3 | 28.1 | -9.8 | 1.5 | Y/N | N |
| Epoxy | $C_{13}H_{28}$ | FC-70 | 1 | 25.9 | 17.1 | 0.9 | 26.9 | 28.1 | -8.9 | 0.8 | Y/N | N |
| Epoxy | $C_{10}H_{22}$ | FC-70 | 1 | 23.6 | 17.1 | 0.5 | 14.4 | 28.1 | -8.3 | -1.3 | N | N |
| | | | | | | | | | | | | |
| Silicon | $C_{16}H_{34}$ | $H_2O$ | 1 | 27.2 | 72.6 | 51.1 | 9.8 | 7.2 | -5.8 | -0.2 | N | N |
| Silicon | $C_{10}H_{22}$ | $H_2O$ | 1 | 23.6 | 72.6 | 50.8 | 4.2 | 7.2 | -2.3 | -0.5 | N | N |
| Silicon | $C_8H_{18}$ | $H_2O$ | 1 | 21.4 | 72.6 | 50.8 | 0 | 7.2 | -0.2 | -0.6 | N | N |
| Silicon | $C_6H_{14}$ | $H_2O$ | 1 | 18.6 | 72.6 | 50.9 | 0 | 7.2 | 2.5 | -0.6 | Y/N | N |
| Silicon | $C_5H_{12}$ | $H_2O$ | 1 | 17.2 | 72.6 | 51.0 | 0 | 7.2 | 3.9 | -0.6 | Y/N | N |

### 10.2.3. Fabrication of slippery surfaces

From these principles, we fabricated a set of SLIPS designed to repel liquids spanning a broad range of surface tensions. To generate roughness, we tested two types of porous solids, periodically ordered and random: arrays of nanofibers functionalized with a low-surface energy polyfluoroalkyl silane[5], and a random network of Teflon nanofibers distributed throughout the bulk substrate, respectively (Figure 65). Teflon membranes with average pore size of ≥ 200 nm and thickness of ~ 60–80 μm were purchased from Sterlitech Corporation, WA, USA. These membranes were used as received without further modification (SLIPS 1 sample). The polymer

nanofiber arrays were made from silicon masters following the procedure described in ref. 5. The resulting dimensions of the nanostructures in epoxy replica were diameter of ~300 nm, height of 5 μm and pitch of 2 μm for the SLIPS 2 sample mentioned in the text and diameter of ~ 300 nm, height of ~ 500 nm to 2 μm and pitch of 0.9 μm for the SLIPS 3 sample, respectively. The epoxy replicas were further rendered hydrophobic by putting the samples in a vacuum desiccator overnight with a glass vial having 0.2 mL heptadecafluoro-1,1,2,2-tetrahydrodecyltrichlorosilane (available from Gelest, Inc.).

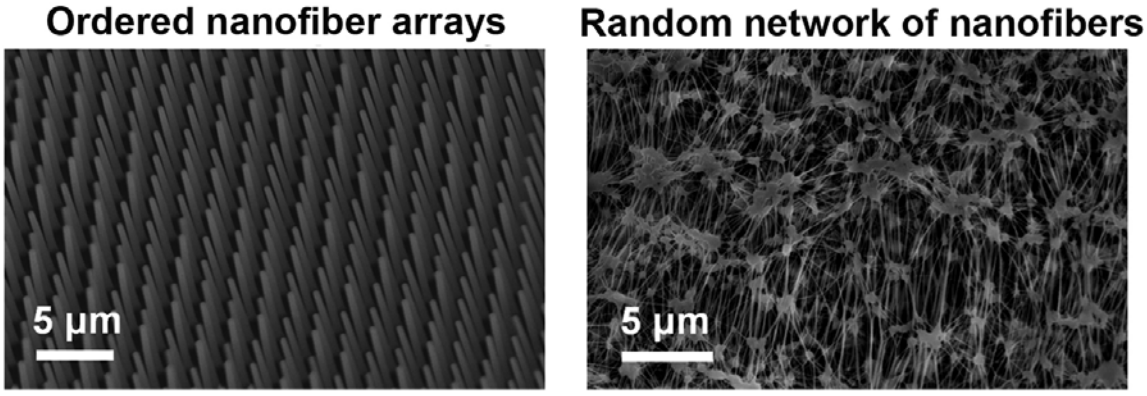


Figure 65. SEM images showing the morphologies of porous/textured substrate materials: epoxy-based nanofiber arrays (left) and Teflon-based porous nanofiber networks (right). Reprinted from ref. 3 with permission from Nature Publishing Group.

For the lubricating film, we chose low-surface-tension perfluorinated liquids (for example, 3M Fluorinert FC-70 ($\gamma_B$ =17.1 mN/m; or DuPont Krytox oils) that are non-volatile and are immiscible with both aqueous and hydrocarbon phases and therefore able to form a stable, slippery interface with our solid substrates (that is, $\Delta E_1 > 0$ and $\Delta E_2 > 0$) for a variety of polar

and non-polar liquids including water, acids and bases, alkanes, alcohols and ketones (Figure 66). The SLIPS were generated through liquid imbibition into the porous materials[201], resulting in a homogeneous and smooth surface. Lubricating fluid was added onto the surfaces by pipette to form an over-coated layer. The fluid spreads spontaneously onto the whole substrate through capillary wicking. The thickness of the over-coated layer can be controlled by the fluid volume given a known surface area of the sample.

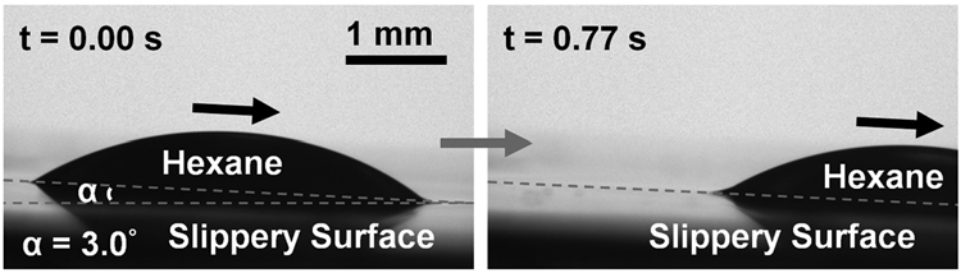


Figure 66. Optical micrographs demonstrating the mobility of a low-surface-tension liquid hydrocarbon—hexane ($\gamma_A$ = 18.6±0.5mN/m, volume 3.6 μL)—sliding on a SLIPS at a low angle ($\alpha$ = 3.0°). Reprinted from ref. 3 with permission from Nature Publishing Group.

As briefly mentioned above, the lubricating fluids used for the experiment are perfluorinated fluids (e.g., 3M fluorinert™ FC-70, Dupont™ Krytox® 100 and 103). Unless otherwise specified, FC-70 was used throughout the experiments. Specifically, the density, kinematic viscosity, and optical refractive index of FC-70 at 25 °C are 1940 kg/m$^3$, 0.12 cm$^2$/s, and 1.303, respectively (see Table 3). The test liquids were obtained from Sigma Aldrich which include pentane (reagent grade, 98%), hexane (puriss, absolute, ≥ 99.0%), heptane (biotech. grade, ≥ 99.0%), octane (puriss, ≥ 99.0%), nonane (ReagentPlus®, 99%), decane (ReagentPlus®,

≥ 99.0%), undecane (≥ 99.0%), dodecane (ReagentPlus®, ≥ 99.0%), tridecane (≥ 99.0%), hexadecane (ReagentPlus®, 99%), dipropylene glycol (99%, mixture of isomers), ethylene glycol (anhydrous, 99.8%), glycerol (99%). Deionized water with a resistivity of 18.3 MΩ·cm was used for the measurements. Ethanol (Pharmco-Aaper, 200 proof, absolute) was used for self-cleaning experiments. Crude oil samples were purchased from ONTA, Inc (Ontario, Canada), which are paraffinic, sweet (i.e., sulfur level ≤ 0.5%), extra-light and light crude oils originated from Appalachian Basin and Louisiana, USA, respectively. Surface tensions of the test liquids were measured by the pendant drop method.

Table 3. Physical and chemical properties of the perfluorinated fluids provided by manufacturers. Reprinted from ref. 3 with permission from Nature Publishing Group.

| Trade Name | Chemical Composition | Density ($kg/m^3$) | Kinematic Viscosity ($cm^2/s$) |
|---|---|---|---|
| FC-70 | perfluorotri-n-pentylamine | 1940 (at 25°C) | 0.12 (at 25°C) |
| Krytox® 100 | perfluoropolyether | 1870 (at 0°C) | 0.12 (at 20°C) |
| Krytox® 103 | perfluoropolyether | 1920 (at 0°C) | 0.82 (at 20°C) |

## 10.3. Characterizations of slippery surfaces

In this section, we have conducted various measurements of slippery surfaces to evaluate their characteristics and performance. First, we characterized their surface roughness to verify

ultra-smoothness of slippery surfaces. Second, we measured contact and sliding angles, which are standard techniques to characterize the liquid repellency of surfaces. Third, we measured the effects of the thickness of the lubricating layer and the evaporation curve of the lubricating layer because the lubricating layer thickness can vary due to evaporation or flow during use. Fourth, we tested slippery surfaces under high pressure to evaluate its pressure stability. Fifth, we characterized self-repairing behavior of slippery surfaces, which is a unique feature of slippery surfaces due to presence of the lubricating layer. Finally, we measured optical transmission of slippery surfaces in both visible and infra red wavelength ranges to evaluate transparency of the generated surfaces.

### 10.3.1. Surface roughness measurements

To analyze the surface roughness of SLIPS, a replication process was developed to reproduce the morphology of the surface. We first made a negative mold of the lubricating layer using polydimethylsiloxane (PDMS), then fabricated positive replicas with UV curable epoxy resin (UVO 114 available from Epoxy Technology) (see Figure 67). The smoothness of the replicated surface was characterized by the high resolution atomic force microscopic measurements, where the average roughness was on the order of 1 nm or less as shown in Table 4. In this measurement, it is important to note that the measured roughness has reached the physical roughness limits for flat PDMS and UVO 114 epoxy resin (i.e., order of 1 nm or

less[112,204]). Therefore, the measured values may only represent an upper bound for the actual roughness of the lubricating film, which in principle should be close to molecular smoothness (i.e., roughness < 0.5 nm). Nonetheless, it is evident from the roughness analysis that the lubricating fluid overcoats the surface topographies of the porous solid, forming a near molecularly smooth surface.

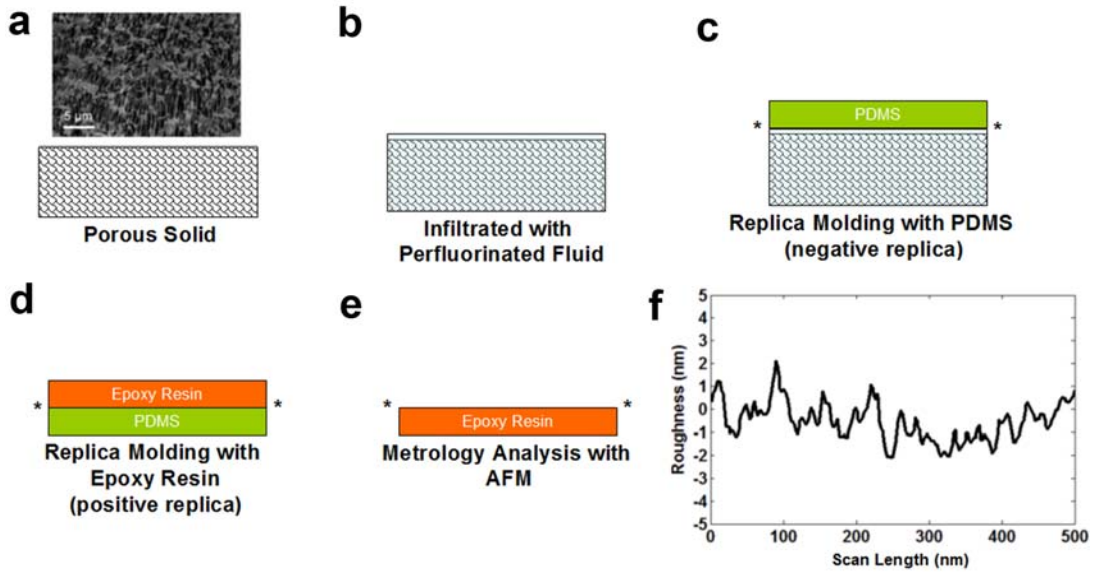


Figure 67. (a)–(e) Schematics showing the replication process using polydimethylsiloxane (PDMS) and UVO 114 epoxy resin. The interface marked with an asterisk indicates the surface that was replicated for surface characterization. (f) The smoothness of the surface was further confirmed by the high resolution atomic force microscopic measurements, where the average roughness is on the order of 1 nm or less (see Table 4 for the measured average and root-mean-square roughness). Reprinted from ref. 3 with permission from Nature Publishing Group.

Table 4. Surface roughness measurements on the replicas of SLIPS. Surface roughness measurements were carried out with an atomic force microscope (Veeco NanoMan VS). The scanning tip used for the measurements was Veeco RTESP, with a measured operating resonant frequency of 270.66 kHz. Typical operating parameters are: scan rate = 0.5 Hz – 1.02 Hz; Integral gain = 1.087; Proportional gain = 5.344; Amplitude set-point = 252.3 mV. Both average and root-mean-square (R.M.S.) roughness were obtained for different scan sizes. *N* denotes the number of independent measurements. Reprinted from ref. 3 with permission from Nature Publishing Group.

| Scan Size | Average Roughness (nm) | R.M.S. Roughness (nm) | N |
|---|---|---|---|
| 100 nm × 100 nm | 0.84±0.13 | 1.11±0.16 | 3 |
| 500 nm × 500 nm | 1.07±0.05 | 1.43±0.05 | 3 |
| 2500 nm × 2500 nm | 1.05±0.01 | 1.47±0.04 | 3 |

### 10.3.2. Contact and sliding angle measurements

The contact angle measurements were performed by a contact angle measurement system (KSV CAM 101) at room temperature (i.e., 20–23$^{o}$C) with ~20% relative humidity. The system was calibrated before all the measurements were taken. The droplet volume for the measurement was ~5 μL (unless otherwise specified) and the macroscopic droplet profile was captured through a camera equipped with an optical system for amplification of the captured images. In measuring the contact angle hysteresis, the surface was tilted with respect to the horizontal plane until the liquid droplet started to slide along the surface. The droplet profile was fitted into a spherical cap profile by a computer program provided from the system in order to determine the advancing and receding angles, the sliding angle of the droplet, as well as the droplet volume. The accuracy of

the contact angle measurements and of the sliding angles is ~0.1°. The contact and sliding angles of various liquids on SLIPS are summarized in the Figure 68 and the surface tension values used in Figure 68a are measured by pendant drop measurements using KSV CAM 101 system as summarized in Table 5.

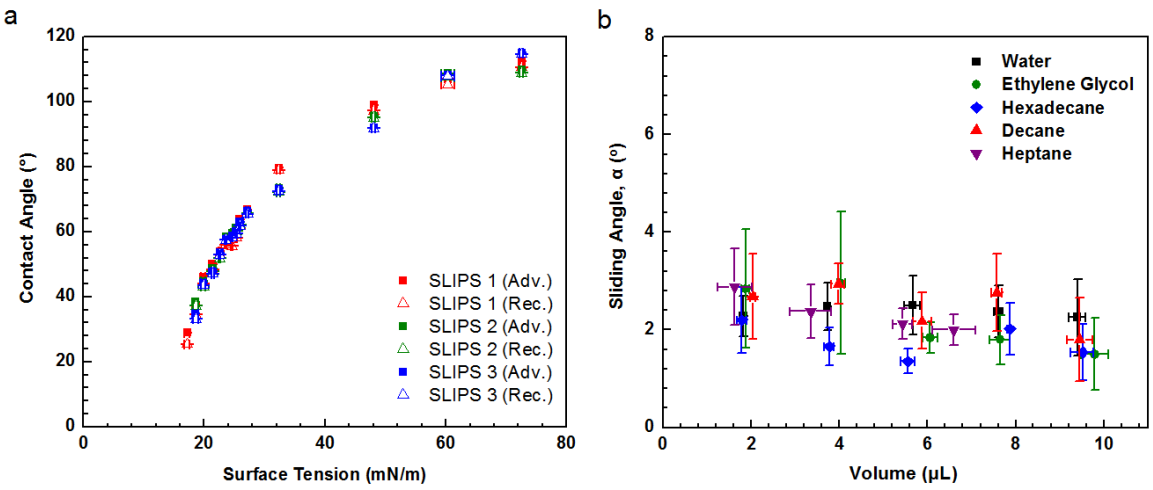


Figure 68. Contact and sliding angles of various liquids on SLIPS. (a) A plot showing the contact angles of various polar and non-polar liquids on different SLIPS. SLIPS 1, 2, and 3 refer to the surfaces made from 1: Teflon membrane, 2: epoxy nanofiber array of geometry 1 (pitch = 2 μm; height = 5 μm; and fiber diameter = 300 nm), and 3: geometry 2 (pitch = 900 nm; height = 500 nm to 2 μm; and fiber diameter = 300 nm), respectively. Advancing and receding contact angles on the respective surfaces are indicated in solid squares and empty triangle symbols, respectively. The test liquids used in the measurements were (in ascending order of liquid surface tension): hexane, heptane, octane, nonane, decane, undecane, dodecane, tridecane, hexadecane, dipropylene glycol, ethylene glycol, glycerol, and water (See also Table 5). (b) A plot showing the sliding angles of the various liquid droplets with respect to the droplet volume on a SLIPS. High liquid mobility on the surface is signified by the low sliding angles for all liquids. Error bars indicate standard deviations from at least five independent measurements. Reprinted from ref. 3 with permission from Nature Publishing Group.

Table 5. Measured surface tension for various polar and non-polar liquids. Surface tension measurements were performed by the pendant drop method at ambient conditions (temperature = 22 to 24$^{o}$C and relative humidity = 18 to 26%). Densities of the individual liquids are provided by the manufacturer specifications. *N* denotes the number of independent measurements. *Extra-light crude oil was obtained from Appalachian Basin, USA. **Light crude oil was obtained from Louisiana, USA. Reprinted from ref. 3 with permission from Nature Publishing Group.

| **Liquid** | **Surface Tension (mN/m)** | ***N*** |
|---|---|---|
| Water | 72.4 ± 0.1 | 116 |
| Glycerol | 60.3 ± 1.1 | 35 |
| Ethylene Glycol | 48.1 ± 0.3 | 32 |
| Dipropylene Glycol | 32.3 ± 0.3 | 35 |
| Extra-light Crude Oil* | 27.0 ± 0.8 | 15 |
| Light Crude Oil** | 25.6 ± 0.9 | 15 |
| Hexadecane | 27.2 ± 0.2 | 31 |
| Tridecane | 25.9 ± 0.1 | 30 |
| Dodecane | 25.3 ± 0.1 | 32 |
| Undecane | 24.6 ± 0.2 | 32 |
| Decane | 23.6 ± 0.1 | 32 |
| Nonane | 22.6 ± 0.2 | 31 |
| Octane | 21.4 ± 0.2 | 30 |
| Heptane | 19.9 ± 0.3 | 32 |
| Hexane | 18.6 ± 0.5 | 30 |
| Pentane | 17.2 ± 0.5 | 57 |
| 3M Fluorinert™ FC-70 | 17.1 ± 0.3 | 43 |

Each of these SLIPS exhibits extreme liquid repellency as signified by very low contact angle hysteresis ($\Delta\theta < 2.5°$, Figure 69) and by very low sliding angles ($\alpha \leq 5°$ for droplet volume $\geq 2$ μL; Figure 68b) against liquids of surface tension ranging from ~17.2±0.5mN/m (n-pentane) to 72.4 mN/m (water). Contact angle hysteresis (that is, the difference between the advancing and receding contact angles of a moving droplet), and sliding angle (that is, the surface tilt required for droplet motion) directly characterize resistance to mobility[205]; the low values therefore confirm a lack of pinning, consistent with a nearly defect-free surface[206].

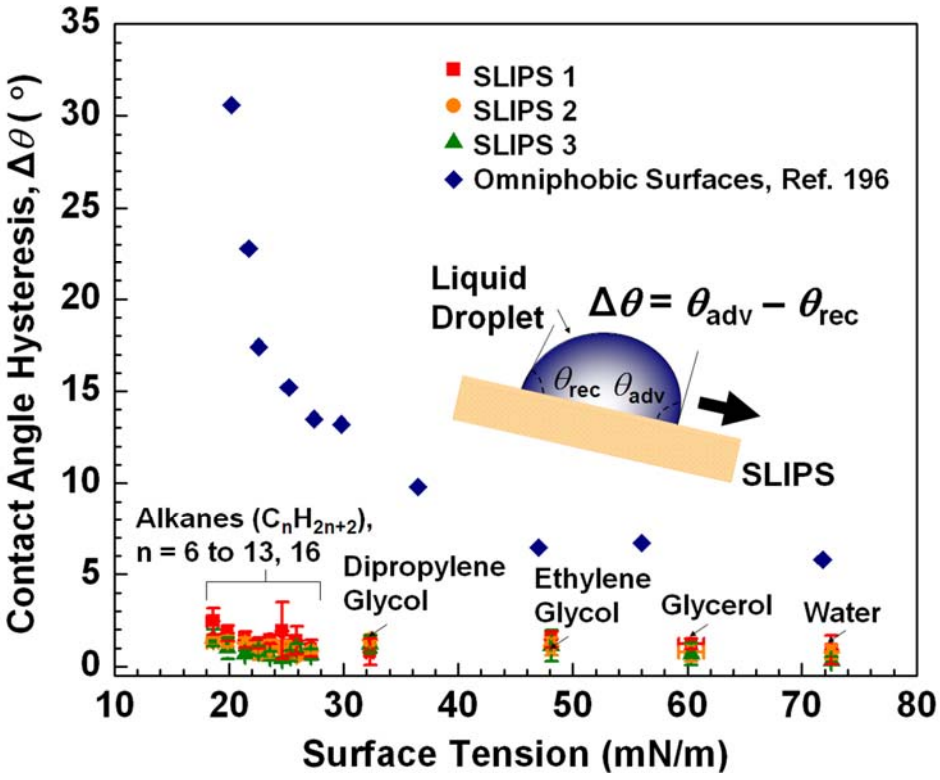


Figure 69. Comparison of contact angle hysteresis as a function of surface tension of test liquids (indicated) on SLIPS and on an omniphobic surface reported in ref. 196. In the inset, the advancing and receding contact angles of a liquid droplet are denoted as $\theta_{adv}$, and $\theta_{rec}$, respectively. SLIPS 1, 2 and 3 refer to the surfaces made of Teflon porous membrane (SLIPS 1), an array of epoxy fibers of geometry 1 (pitch ~ 2 μm, height ~ 5 μm, fiber diameter ~ 300 nm)

(SLIPS 2) and an array of epoxy fibers of geometry 2 (pitch ~ 900 nm, height ~ 500nm – 2 mm, fiber diameter ~ 300 nm) (SLIPS 3). Error bars indicate standard deviations from three independent measurements. Reprinted from ref. 3 with permission from Nature Publishing Group.

Based on the measured contact angle hysteresis and droplet volume (~4.5 μL), the estimated liquid retention force[207] on each of the SLIPS is 0.83±0.22 mN for n = 6. This performance is nearly an order of magnitude better than the state-of-the-art lotus-leaf-inspired omniphobic surfaces, whose liquid retention forces are of the order of 5 mN for low-surface-tension liquids (that is, $\gamma_A < 25$ mN/m) at similar liquid volumes[196]. Moreover, the liquid-repellency of SLIPS is insensitive to texture geometry (Figure 69), provided that the lubricating layer covers the textures (Figure 70). This further confirms that liquid repellency is primarily conferred by the lubricating film, with the porous solid having the secondary, but critically important, role of immobilizing the film. Additionally, unlike lotus-leaf-inspired omniphobic surfaces where contact angle hysteresis depends on liquid surface tension and increases dramatically upon decrease of surface tension (Figure 69), such a dependence is absent for SLIPS owing to the chemical homogeneity and physical smoothness of the liquid–liquid interface.

### 10.3.3. Thickness and evaporation measurements

As briefly mentioned above, the thickness of the lubricating layer is important to maintain the slipperiness of our surface. The thickness of the lubricating fluid was determined by measuring the weight of the fluid added to the porous solid over a measured wetted area. The weight of the fluid was measured by a high resolution balance (Mettler Toledo XP 105 DeltaRange analytical balance) with a sensitivity of 0.01 mg. The density of the lubricating fluid (i.e., 3M fluorinert™, FC-70) was provided by the manufacturer specifications (Table 3). The thickness of the fluid was then determined from the information based on the measured weight, the wetted area, and the fluid density. As shown in Figure 70, the performance of the slippery surface was insensitive to the thickness of the lubricating layer as long as the lubricating layer covers the texture. But, as the texture was exposed, they acted as pinning sites and induced increase in the contact angle hysteresis. Therefore, it is important to maintain the lubricating layer so that it covers the underlying the texture.

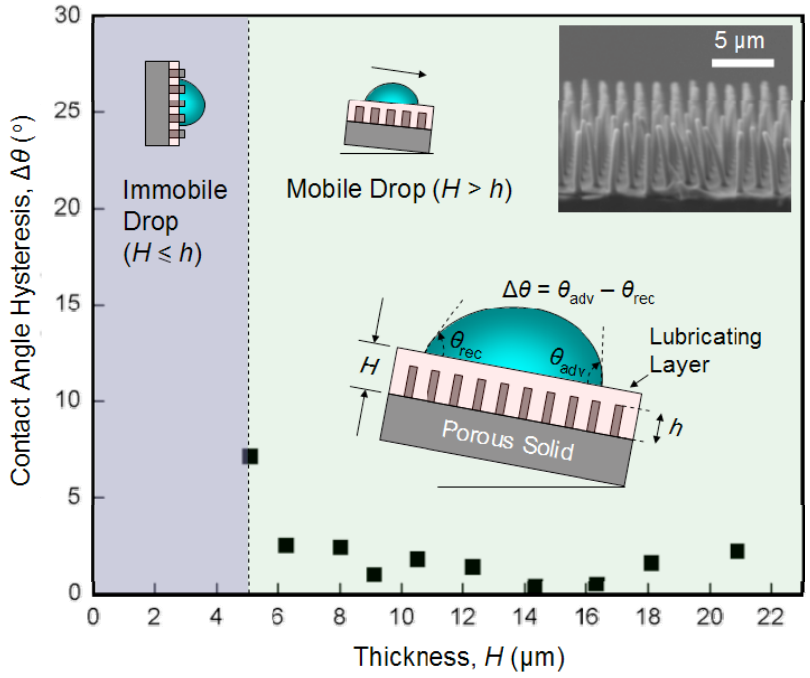


Figure 70. Dependence of liquid repellency on lubricating film thickness. A plot showing the liquid contact angle hysteresis of the surface (black squares) as a function of the thickness of the lubricating layer. It is important to note that when the thickness of the lubricating layer is lower than the height of the surface textures, the liquid droplet becomes pinned on the surface (purple region). The test liquid used for the characterization was decane ($\gamma_A$ = 23.6 ± 0.1 mN/m, volume of ~5 μL). Reprinted from ref. 3 with permission from Nature Publishing Group.

To have a better understanding about the long-term stability of the slippery surface, we have measured the evaporation rate of the liquids that we used for the lubricating layer. The perfluorinated fluids used for the measurements were FC-70, Krytox® 100 and 103. These fluids were incorporated within porous solids to reflect the actual operating conditions. Specifically, the porous solids consisted of a Teflon membrane (SLIPS 1, 47 mm in diameter) connected to a porous glass membrane (pore size ≥ 300 nm, thickness of ~470 μm, and diameter of ~47 mm, Sterlitech Corporation) as a fluid reservoir (Figure 71a). The initial volume of the perfluorinated

fluid was ~1 mL. The mass loss of individual samples was monitored by a high resolution balance with a sensitivity of 0.1 mg. The evaporation data were measured for nine consecutive days in an open area under room conditions (i.e., 22.6±0.8$^{o}$C with 53.2±6.2% relative humidity, $n$ = 9) (Figure 71b). The measured evaporation rates for FC-70, Krytox® 100, and Krytox® 103 were 9.48%/day, 0.80%/day, and <0.05%/day, respectively. And, the performance of SLIPS characterized by tilting angle showed stable behaviors for a month for Krytox® 100, and Krytox® 103 while it rapidly deteriorated for FC-70 as shown in Figure 71c. From the results, we can select the lubricating liquid according to the specific needs and we can further extend the lifetime of the slippery surface by utilizing a reservoir which can self-replenish the lubricating fluid by wicking.

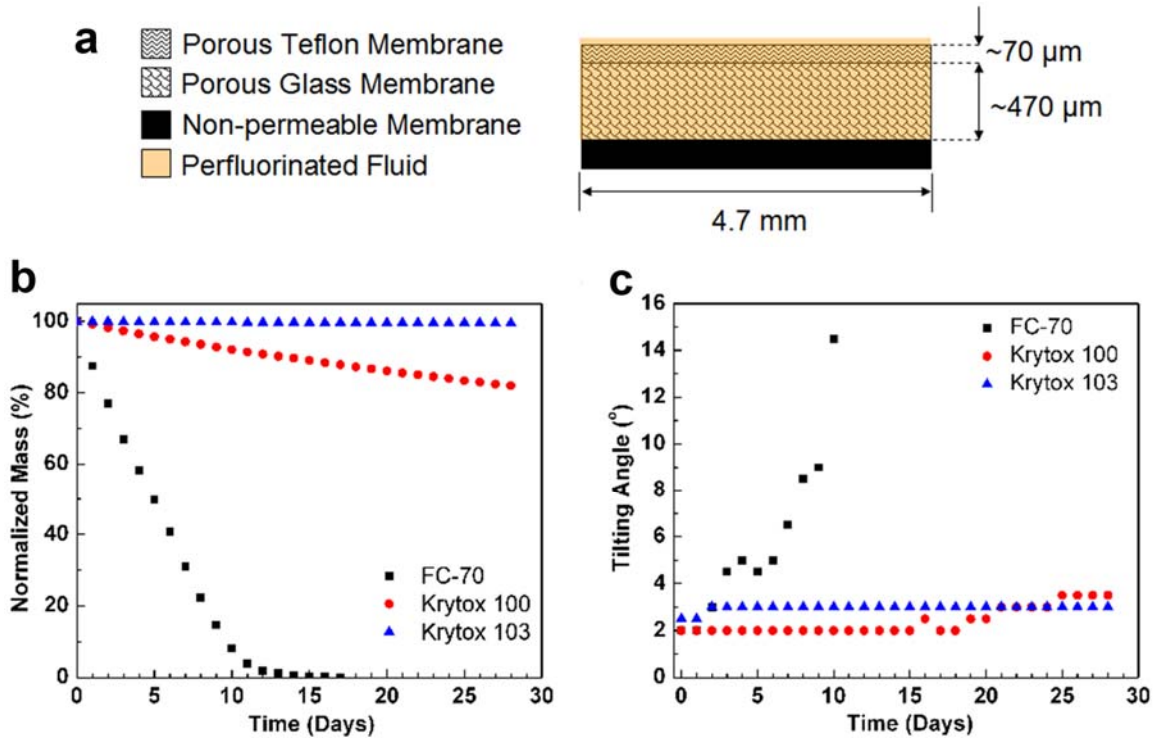


Figure 71. Evaporation characteristics of perfluorinated fluids in SLIPS. (a) Schematic showing the cross section of a SLIPS with a reservoir containing a fixed amount of a perfluorinated fluid. The initial thickness of the perfluorinated fluid was ~550 – 570 μm. (b) A plot showing the mass change of the perfluorinated fluids in the SLIPS in a 9-day period. (c) A plot showing the wetting property of the SLIPS in a 9-day period. Specifically, the wetting property was characterized by measuring the tilting angle of octane (~30 μL) on the surfaces, where the measurement error is within $0.5^{o}$. Reprinted from ref. 3 with permission from Nature Publishing Group.

### 10.3.4. High pressure measurements

We tested the pressure stability of the slippery surfaces by using a pressurized chamber and a drop impact test. The characterization of the performance of the SLIPS at high pressure was carried out in the facilities at Schlumberger-Doll Research Center, Cambridge, MA. Specifically, a decane droplet (~2 to 3 μL) was placed on a Teflon porous membrane (Sterlitech, ≥ 200 nm

pore size, ~5 mm × 5 mm) infiltrated with perfluorinated lubricating fluid (Dupont™, Krytox® 103). The membrane was glued onto a metal platform for transfer into a custom-made high-pressure chamber. The pressure chamber was equipped with transparent sapphire windows for external optical monitoring. During the experiment, pressurized nitrogen gas was injected into the high-pressure cell, and pressure in the chamber was monitored via the output of a strain gauge. The rates of pressure change were monitored during the process, and were typically from ~ 70 to 675 atm/min. Once the targeted pressure was reached, the sliding angle of the decane droplet was measured by tilting the chamber with respect to the horizontal until the droplet started to slide.

Experiments performed in a pressurized nitrogen environment show that SLIPS are capable of repelling water and liquid hydrocarbons both at and while transitioning to a pressure of ~676 atm (the highest available pressure in our setup). This is equivalent to the hydrostatic pressure at a depth of ~7 km (Figure 72). To our knowledge, the highest recorded pressure stability of a superhydrophobic surface for water is ~7 atm[208]. However, it is important to note that pressure stability for structured surfaces decreases drastically for liquids with low surface tension. For example, recent pressure stability studies of omniphobic surfaces based on impacting hexadecane droplets and evaporating octane droplets demonstrated stability up to only 400 to 1,400 Pa ($4\times10^{-3}$ to $1.4\times10^{-2}$ atm)[193,196]. Whereas the reported omniphobic surfaces fail upon dynamic

impact of low-surface-tension liquids[193], SLIPS repel impacting droplets for a wide assortment of liquid hydrocarbons.

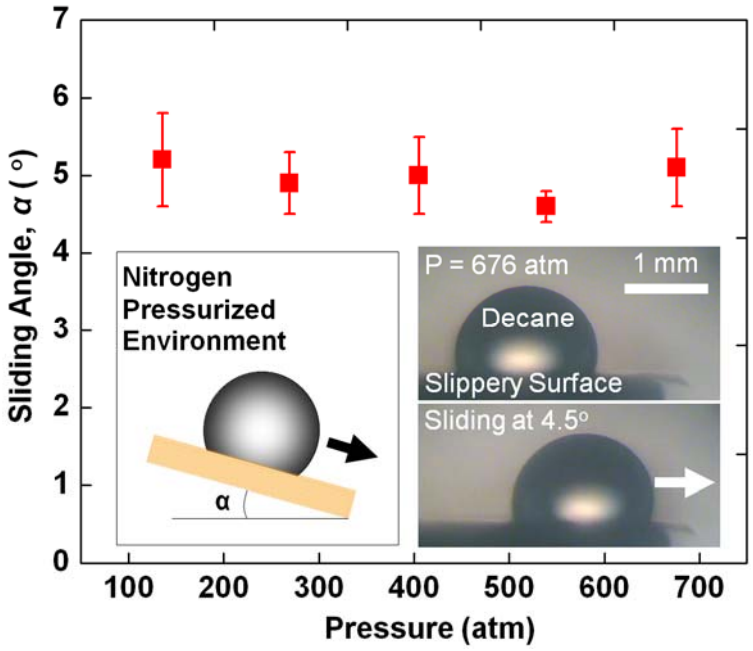


Figure 72. A plot showing the high pressure stability of SLIPS, as evident from the low sliding angle of a decane droplet ($\gamma_A$ = 23.6±0.1mN/m, volume ~ 3 μL) subjected to pressurized nitrogen gas in a pressure chamber. Error bars indicate standard deviations from at least seven independent measurements. Reprinted from ref. 3 with permission from Nature Publishing Group.

The dynamic impact pressure of the droplet acting on the surface, $P_{dynamic}$, was determined by the relationship, $P_{dynamic} = 1/2\rho V^2$, where $V$ and $\rho$ are the velocity and density of the liquid droplet. The free-falling velocity of the liquid droplet was controlled by adjusting the release height of the liquid droplet from a glass syringe needle (Hamilton Company, 0.71 mm in diameter). The motion of the droplet and its subsequent impact onto the surface was captured by a high-speed camera (Phantom V7.3) equipped with a long working distance macro lens (Canon

28, 135 mm) at a frame rate of 10,000 fps. The impact velocity of the droplet was measured by analyzing the high-speed movies, and the experiment was repeated at least three times for each condition. The densities of the liquids were taken from the data provided by the manufacturer specifications. SLIPS remains highly liquid repellent after high pressure liquid impact (dynamic impact pressure > 5000 Pa), as reflected by the low sliding angles of the liquid droplets (i.e., < $2^{o}$). The test liquids used for the experiments were octane ($\gamma_A$ = 21.4 ± 0.2 mN/m), decane ($\gamma_A$ = 23.6 ± 0.1 mN/m), tridecane ($\gamma_A$ = 25.9 ± 0.1 mN/m), and hexadecane ($\gamma_A$ = 27.2 ± 0.2 mN/m), where the volume of individual liquid droplet was ~ 5 – 6 μL. In contrast, lotus-leaf-inspired omniphobic surfaces can withstand only a ~400 Pa impact pressure for hexadecane droplets[193], which is at least an order of magnitude lower than that of SLIPS.

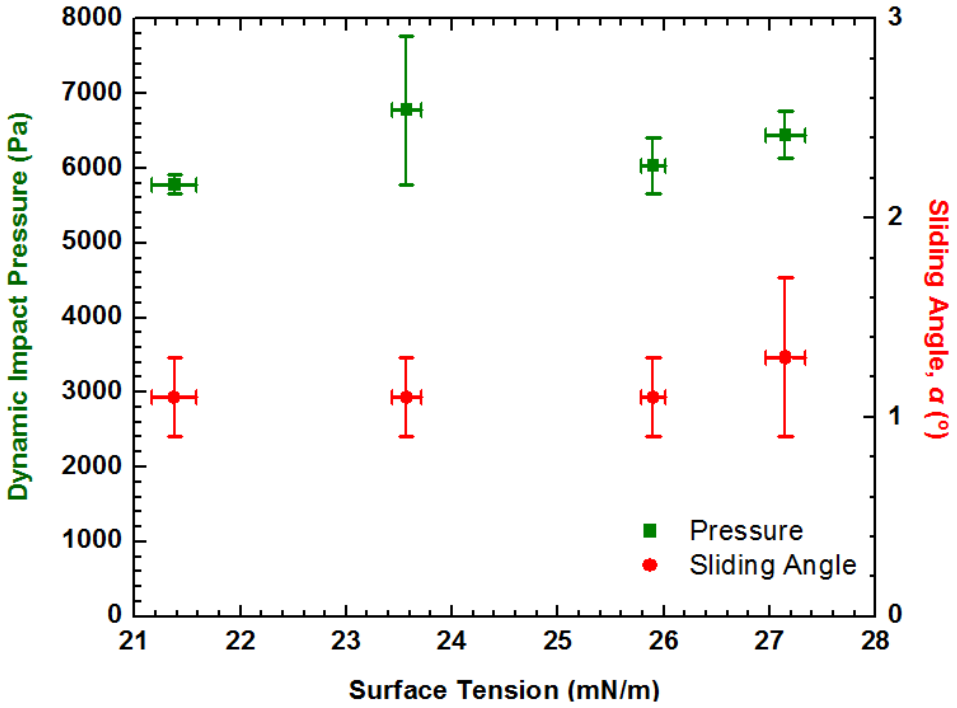


Figure 73. Drop impact characterization of SLIPS. A plot showing the dynamic impact pressure of liquid hydrocarbons and their sliding angles on SLIPS. Error bars indicate standard deviations from at least five independent measurements. Reprinted from ref. 3 with permission from Nature Publishing Group.

### 10.3.5. Self-healing property measurements

The lubricating film also serves as a self-healing coating to rapidly restore the liquid-repellent function following damage of the porous material by abrasion or impact. The fluidic nature of the lubricating layer means that the liquid simply flows towards the damaged area by surface-energy-driven capillary action[209], and spontaneously refills the physical voids. As observed by high-speed camera (Phantom v. 7.3) imaging, the measured self-recovery time for a ~50 μm fluid displacement of the FC-70 lubricating layer on an epoxy-resin-based SLIPS is

~150 ms (Figure 74a)[197]. Even more impressively, SLIPS can repeatedly restore their liquid-repellent function upon recurring, large-area physical damage (Figure 74b, Figure 75).

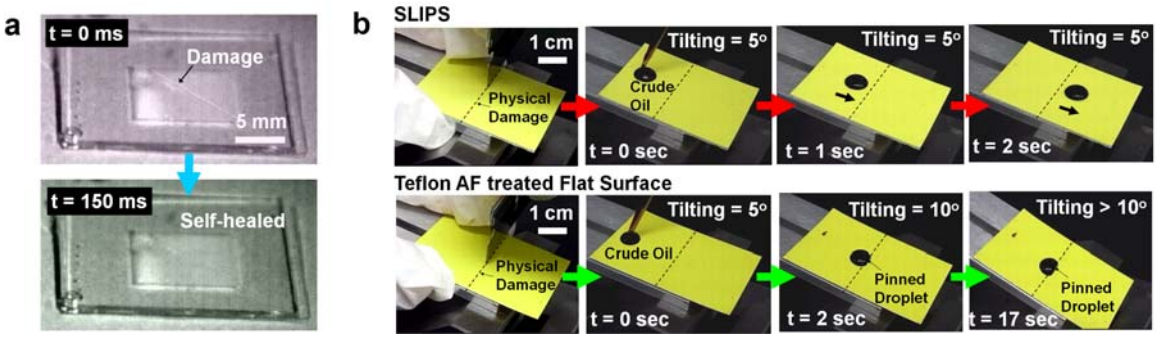


Figure 74. (a) Time-lapse images showing the capability of a SLIPS to self-heal from physical damage ~ 50 μm wide on a timescale of the order of 100 ms. (b) Time-lapse images showing the restoration of liquid repellency of a SLIPS after physical damage, as compared to a typical hydrophobic flat surface (coated with DuPont Teflon AF amorphous fluoropolymers) on which oil remains pinned at the damage site. Reprinted from ref. 3 with permission from Nature Publishing Group.

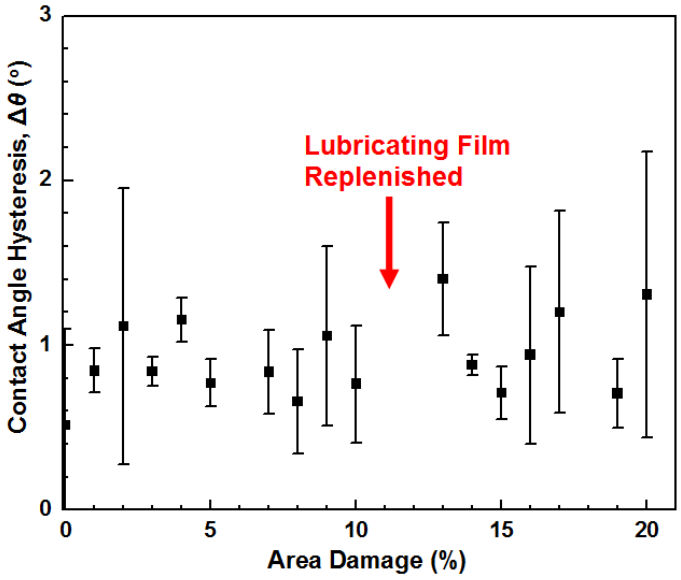


Figure 75. Restoration of liquid repellency function of SLIPS upon repeated physical damage. A plot showing the liquid contact angle hysteresis with respect to cumulative physical damage of

SLIPS. Area damage is the area of physical damage normalized with respect to the total surface area of SLIPS. It is evident that the liquid repellency function is restored even after repeated physical damage. The test liquid used was decane ($\gamma_A = 23.6 \pm 0.1$ mN/m, volume of ~5 μL) with an initial lubricating film thickness of ~ 20 μm. In addition, SLIPS is repairable by simply replenishing the lubricating fluid (as indicated in the red arrow), which regenerates the liquid repellency. Error bars indicate standard deviations from at least three independent measurements. Reprinted from ref. 3 with permission from Nature Publishing Group.

### 10.3.6. Optical transparency measurements

We further demonstrate that, by choosing substrate and lubricant materials with matching refractive indices, SLIPS can be engineered for enhanced optical transparency in visible and/or near-infrared wavelengths (Figure 76a-c). Optical transparency is challenging to achieve through superhydrophobic surfaces, because they require nanostructures with dimensions under the sub-diffraction limit (< ~100 nm)[210]; the large difference in refractive index at the solid–air interface of these structured surfaces results in significant light scattering that reduces light transmission (Figure 76a-c). Thus, the unique design of slippery surfaces allow us to control the optical property by selecting the substrate and lubricant liquids depending on the specific needs of applications.

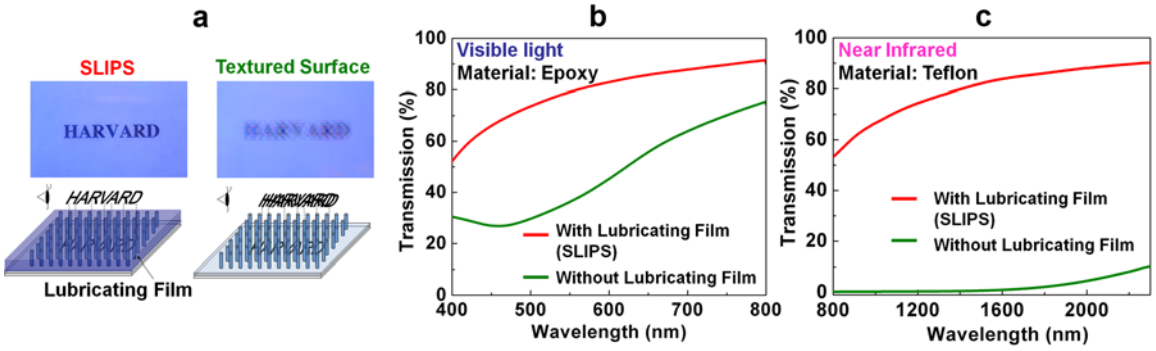


Figure 76. (a) Optical images showing enhanced optical transparency of an epoxy-resin-based SLIPS (left) as compared to significant scattering in the non-infused superhydrophobic nanostructured surface (right) in the visible light range. Top panels show top views; bottom panels show schematic side views. (b) Optical transmission measurements for an epoxy resin-based SLIPS in the visible light range (400–750 nm). (c) Optical transmission measurements for a Teflon-based SLIPS in the near-infrared range (800–2,300 nm). Optical transmission measurements were carried out using an UV-Vis-NIR spectrophotometer (Varian Cary® 5000) in the facilities at Schlumberger-Doll Research Center, Cambridge, MA. Measurements for all of the samples were taken from the wavelength range of 400 nm to 2300 nm at a resolution of 1 nm. All optical transmission measurements were normalized with respect to the transmission spectrum of air at room conditions. Reprinted from ref. 3 with permission from Nature Publishing Group.

## 10.4. Applications of slippery surfaces

In addition to repelling liquids in their pure forms, SLIPS effectively repel complex fluids, such as crude oil (Figure 77a) and blood (Figure 77b), that rapidly wet and stain most existing surfaces. SLIPS also repel ice (Figure 77c) and can serve as anti-sticking, slippery surfaces for insects (Figure 77d)—a direct mimicry of pitcher plants. The omniphobic nature of our SLIPS also helps to protect the surface from a wide range of particulate contaminants by allowing

self-cleaning by a broad assortment of fluids that collect and remove the particles from the surface (Figure 78). Any of these capabilities could be compromised over time if the lubricant evaporates or is lost owing to shearing under high flow conditions, so choosing a lubricant with a minimal evaporation rate or an enhanced viscosity, or integrating the SLIPS with a fluid reservoir that enables continual self-replenishing (Figure 71), enables prolonged operation.

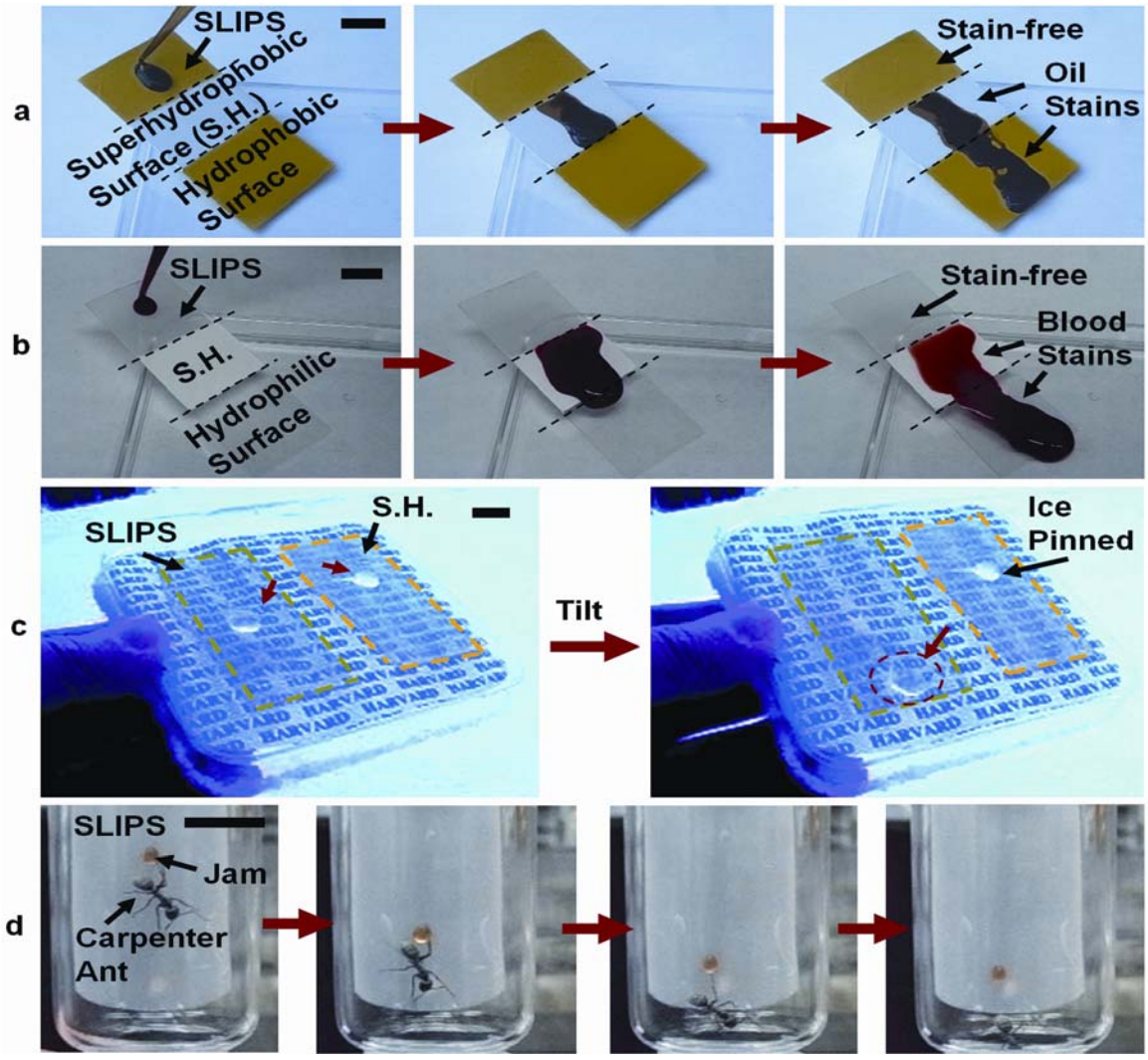


Figure 77. Repellency of complex fluids, ice and insects by SLIPS. (a) Movement of light crude oil on a substrate composed of a SLIPS, a superhydrophobic Teflon porous membrane, and a flat hydrophobic surface. (b) Comparison of the ability to repel blood by a SLIPS, a

superhydrophobic Teflon porous membrane, and a flat hydrophilic glass surface. (c) Ice mobility on a SLIPS (highlighted in green) compared to strong adhesion to an epoxy-resin-based nanostructured superhydrophobic surface (highlighted in yellow). The experiments were performed outdoors (note the snow in the background) when temperature and relative humidity were –4 °C and ~45%, respectively. Note also the reduced frosting and the resulting transparency of the SLIPS. (d) Demonstration of the inability of a carpenter ant to hold on to SLIPS. The ant (and a drop of fruit jam it is attracted to) slide along the SLIPS when the surface is tilted. Note that the ant can stably attach to normal flat hydrophobic surfaces, such as Teflon. All scale bars represent 10mm. Reprinted from ref. 3 with permission from Nature Publishing Group.

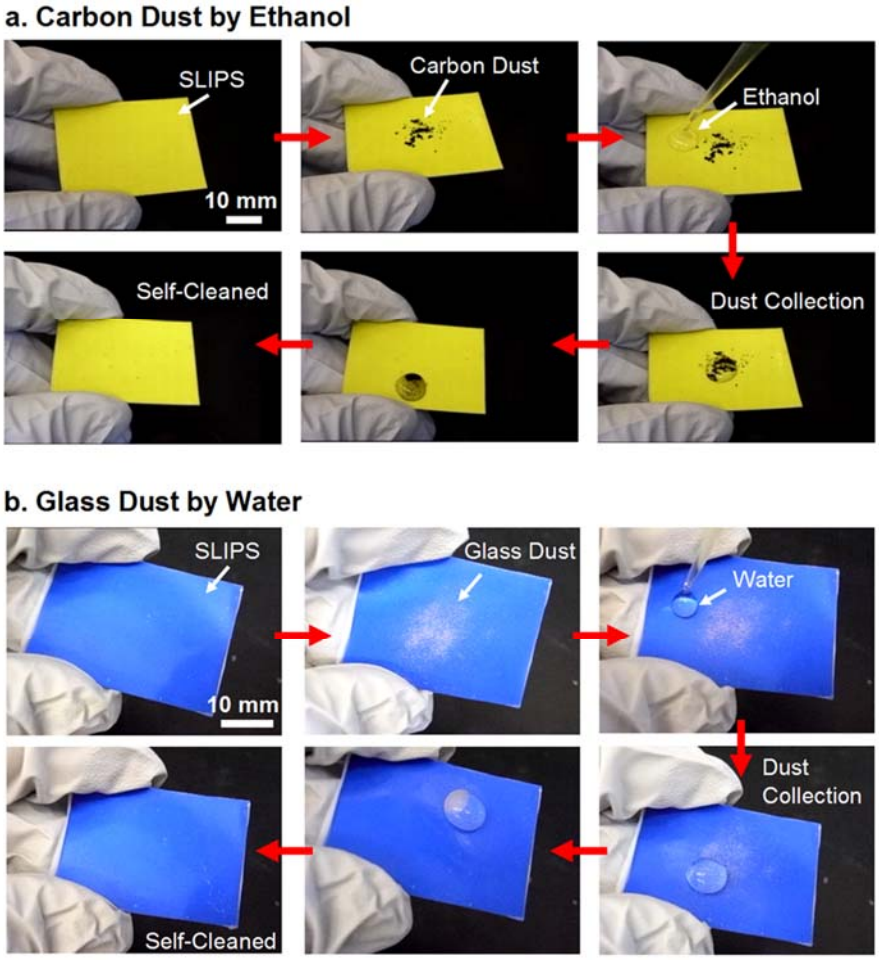


Figure 78. Self-cleaning of SLIPS. (a) Time sequence images showing the dusting of SLIPS with carbon particles (≤ 150 μm), and the subsequent self-cleaning action by an ethanol droplet (~50 μL). (b) Time sequence images showing the dusting of SLIPS with glass particles (≤ 106 μm), and the subsequent self-cleaning action by a water droplet (~50 μL). Activated carbon particles

(Sigma Aldrich, Darco® G-60 100 mesh, ≤ 150 μm) and glass beads (Sigma Aldrich, acid washed, ≤ 106 μm) were used as dust for self-cleaning experiments. In the rare situation where dust particles are preferentially adhered to the surface (e.g., fluorinated particles) and are completely over-coated by the lubricant, the wetting property of the surface remains unaffected as any immiscible foreign liquids will be floating on top of the over-coated lubricating fluid layer. Reprinted from ref. 3 with permission from Nature Publishing Group.

## 10.5. Summary

No synthetic surface reported until now possesses all the unique characteristics of SLIPS: negligible contact angle hysteresis for low surface tension liquids and their complex mixtures, low sliding angles, instantaneous and repeatable self-healing, extreme pressure stability and optical transparency. Our bioinspired SLIPS, which are prepared simply by infiltrating low-surface-energy porous solids with lubricating liquids, provide a straightforward and versatile solution for liquid repellency and resistance to fouling. Because low-surface-energy porous solids are abundant and commercially available, and the structural details are irrelevant to the resulting performance, one can turn any of these solids into highly omniphobic surfaces without the need to access expensive fabrication facilities. Any liquid film is inherently smooth, self-healing and pressure resistant, so the lubricant can be chosen to be either biocompatible, index-matched with the substrate, optimized for extreme temperatures, or otherwise suitable for specific applications. With a broad variety of commercially available lubricants that possess a

range of physical and chemical properties, we are currently exploring the limits of the performance of SLIPS for long-term operation and under extreme conditions, such as high flow, turbulence, and high- or low-temperature environments. It is anticipated that SLIPS can be developed to serve as omniphobic materials capable of meeting emerging needs in biomedical fluid handling, fuel transport, anti-fouling, anti-icing, self-cleaning windows and optical devices, and many more areas that are beyond the reach of current technologies.

# Chapter 11 Conclusions and Recommendations for Future Research

We have studied a variety of phenomena occurring by interaction of structured solids with liquids. In particular, we have investigated pattern formation of fibrous surfaces by self-organization. By changing the properties of fiber arrays, we have shown formation of various assembly patterns by evaporation-induced self-organization. Especially, we have demonstrated that control of fiber properties by simple benchtop processes can be used to generate complex patterns like hierarchical and/or chiral structures, which are frequently observed in nature. We have also demonstrated that controlling the shape and movement of the liquid-vapor interface can be used to form tunable patterns with a long-range order. Going beyond fiber arrays, we have investigated cellular structures as another example of building blocks and demonstrated reversible chiral pattern formation by utilizing swelling-induced buckling. Moreover, when structured solids are infiltrated with lubricating liquids, they can show exceptional liquid-repellent behaviors by minimizing adhesion between the liquid-infused surface and immiscible liquids that we want to repel. All these studies show that coupling liquids and structured solids with controlled properties open exciting opportunities for generating complex bioinspired structures with novel functionality and discovering new phenomena that

open up new horizons for research.

Key conclusions from this dissertation are summarized as follows:

1. For the first time, we have demonstrated spontaneous chiral pattern formation at mesoscale without using chiral building blocks or environment by immersing rationally designed arrays of fibers in an evaporating liquid. As a liquid evaporates, chirality appears by assembly of fibers which try to maximize contact areas between them.
2. Using a model self-assembly system with easily tunable parameters, we have demonstrated that varying the mechanical and/or surface properties of the nanofibers provides us with simple routes for fabricating complex structures with control of size, chirality, and anisotropy by capillary-induced self-organization. Our study provides a broader perspective of how a variety of features contribute collectively to capillary-induced self-assembly and demonstrates many options for fine tuning the assembly to generate diverse structures.
3. The assembly process can be utilized for various applications such as controlled trapping and releasing of objects, adhesion by mechanical interlocking, and security features by reconfiguration of three dimensional surface patterns by interacting with liquids.
4. Besides the fiber properties, manipulating shape and movement of the liquid-vapor

interface can give us new opportunities for controlling pattern formation. Patterning menisci by superimposing two fiber arrays with a liquid between them can generate ordered patterns with tunable periodicity and chirality. Especially, this approach uncovered a new physics phenomenon that Moire patterns could be formed in liquids, which then imprinted patterns on solids by force-mediated patterning due to liquid-vapor interfaces formed among fiber arrays. In addition, controlling the movement of the evaporation front can generate a large-area assembly with a single domain by preventing random nucleation and propagation of the assemblies.

5. We have demonstrated a new mechanism of reversible chiral pattern formation across length scales and chiral amplification by swelling-induced buckling of rationally designed surface-attached cellular structures. Different from previous works, our approach is applicable to wide range of length scales and materials, which opens great potential for applying it to designing a variety of functional surfaces.

6. Coupling thermodynamics and kinetics is important to understand dynamic pattern formation. While previous works modeled the assembly size by minimizing energy of the assembling fibrous surfaces, the kinetics of the assembly shows a multi-step growth of the assembly size. Moreover, harnessing kinetics can provide us novel options to control the pattern formation as we demonstrated control of long-range order and chirality of

swelling-induced patterns from surface-attached cellular structures.

7. Besides pattern formation, infusing fibrous surfaces with lubricating liquids can give us a simple and versatile solution to fabricate slippery surfaces with exceptional liquid repellency, instantaneous and repeatable self-healing, high pressure stability, and optical transparency. Due to its flexibility in design and versatility, it is expected that the slippery surfaces can be developed to meet emerging needs in many areas including biomedical fluid handling, fuel transport, anti-fouling, anti-icing and many other areas that are beyond the reach of current technologies.

Finally, some research topics for further advance are suggested as below:

1. By utilizing development of surface chemistry and surface characterization tools, fine tuning and quantitative characterization of surface properties of fiber arrays can deepen our understanding of the assembly process and provide rich opportunities for dynamically tunable surfaces for applications such as optics, wetting, and drug delivery.

2. Monitoring three dimensional shapes of menisci during evaporation-induced pattern formation using advanced imaging methods such as nano-tomography will further enhance our understanding of dynamics of pattern formation.

3. Trapping chiral objects with mixed chirality by utilizing our swelling-induced chiral structure formation can be useful for application such as sorting structures with desired

chirality.

4. Investigation of memory/erasing mechanisms during swelling-induced pattern formation can be scientifically interesting topics to study. The understanding may provide opportunities to turn conventional materials into shape-memory materials.

5. Expansion of material systems can open new opportunities for applications. For example, using stimuli-responsive materials or other functional materials can give us more control of the system and the resulting properties.

6. Further scaling down of our systems can be beneficial for studying optical properties and applications such as sensing because chiral structures show distinct responses depending on the polarization of light.

# Bibliography


1 Kang, S. H., Wu, N., Grinthal, A. & Aizenberg, J. Meniscus Lithography: Evaporation-Induced Self-Organization of Pillar Arrays into Moire Patterns. *Phys. Rev. Lett.* **107**, 177802 (2011).

2 Pokroy, B., Kang, S. H., Mahadevan, L. & Aizenberg, J. Self-Organization of a Mesoscale Bristle into Ordered, Hierarchical Helical Assemblies. *Science* **323**, 237-240 (2009).

3 Wong, T. S. *et al.* Bioinspired self-repairing slippery surfaces with pressure-stable omniphobicity. *Nature* **477**, 443-447 (2011).

4 Seminara, A., Pokroy, B., Kang, S. H., Brenner, M. P. & Aizenberg, J. Mechanism of nanostructure movement under an electron beam and its application in patterning. *Phys. Rev. B* **83**, 235438 (2011).

5 Pokroy, B., Epstein, A. K., Persson-Gulda, M. C. M. & Aizenberg, J. Fabrication of Bioinspired Actuated Nanostructures with Arbitrary Geometry and Stiffness. *Adv. Mater.* **21**, 463-469 (2009).

6 Shah, A. S., Ben-Shahar, Y., Moninger, T. O., Kline, J. N. & Welsh, M. J. Motile Cilia of Human Airway Epithelia Are Chemosensory. *Science* **325**, 1131-1134 (2009).

7 Gao, X. F. & Jiang, L. Water-repellent legs of water striders. *Nature* **432**, 36-36 (2004).

8 Arzt, E., Gorb, S. & Spolenak, R. From micro to nano contacts in biological attachment devices. *Proc. Natl. Acad. Sci. U. S. A.* **100**, 10603-10606 (2003).

9 Krupenkin, T. N., Taylor, J. A., Schneider, T. M. & Yang, S. From rolling ball to complete wetting: The dynamic tuning of liquids on nanostructured surfaces. *Langmuir* **20**, 3824-3827 (2004).

10 Sidorenko, A., Krupenkin, T. & Aizenberg, J. Controlled switching of the wetting behavior of biomimetic surfaces with hydrogel-supported nanostructures. *J. Mater. Chem.* **18**, 3841-3846 (2008).

11 Shields, A. R. *et al.* Biomimetic cilia arrays generate simultaneous pumping and mixing regimes. *Proc. Natl. Acad. Sci. U. S. A.* **107**, 15670-15675 (2010).

12 Ou, F. S. *et al.* Hot-Spot Engineering in Polygonal Nanofinger Assemblies for Surface Enhanced Raman Spectroscopy. *Nano Lett.* **11**, 2538-2542 (2011).

13 Lau, K. K. S. *et al.* Superhydrophobic carbon nanotube forests. *Nano Lett.* **3**, 1701-1705 (2003).

14 Zhao, Y. P. & Fan, J. G. Clusters of bundled nanorods in nanocarpet effect. *Appl. Phys. Lett.* **88**, 103123 (2006).

15 Geim, A. K. *et al.* Microfabricated adhesive mimicking gecko foot-hair. *Nature Mater.* **2**, 461-463 (2003).

16 Raccurt, O., Tardif, F., d'Avitaya, F. A. & Vareine, T. Influence of liquid surface tension on stiction of SOI MEMS. *J. Micromech. Microeng.* **14**, 1083-1090 (2004).

17 Eisner, T. & Aneshansley, D. J. Defense by foot adhesion in a beetle (Hemisphaerota cyanea). *Proc. Natl. Acad. Sci. U. S. A.* **97**, 6568-6573 (2000).

18 Autumn, K. *et al.* Adhesive force of a single gecko foot-hair. *Nature* **405**, 681-685 (2000).

19 Grinthal, A. *et al.* Steering nanofibers: An integrative approach to bio-inspired fiber fabrication and assembly. *Nano Today* **7**, 35-52 (2012).

20 de Gennes, P.-G., Brochard-Wyart, F. & Quere, D. *Capillarity and Wetting Phenomena : Drops, Bubbles, Pearls, Waves* (Springer, 2004).

21 Kim, H. Y. & Mahadevan, L. Capillary rise between elastic sheets. *J. fluid mech.* **548**, 141-150 (2006).

22 Bico, J., Roman, B., Moulin, L. & Boudaoud, A. Elastocapillary coalescence in wet hair. *Nature* **432**, 690-690 (2004).

23 Green, M. M., Nolte, R. J. M. & Meijer, E. W. *Materials-Chirality*. Vol. 24 (Wiley, 2003).

24 Rubin, N., Perugia, E., Goldschmidt, M., Fridkin, M. & Addadi, L. Chirality of amyloid suprastructures. *J. Am. Chem. Soc.* **130**, 4602-4603 (2008).

25 Lichtenegger, H., Muller, M., Paris, O., Riekel, C. & Fratzl, P. Imaging of the helical arrangement of cellulose fibrils in wood by synchrotron X-ray microdiffraction. *J. appl. crystallogr.* **32**, 1127-1133 (1999).

26 Weiner, S. & Wagner, H. D. The material bone: Structure mechanical function relations. *Annu. Rev. Mater. Sci.* **28**, 271-298 (1998).

27 Wagermaier, W. *et al.* Spiral twisting of fiber orientation inside bone lamellae. *Biointerphases* **1**, 1-5 (2006).

28 Essner, J. J. *et al.* Conserved function for embryonic nodal cilia. *Nature* **418**, 37-38 (2002).

29 Kolb, H. C., Vannieuwenhze, M. S. & Sharpless, K. B. Catalytic Asymmetric Dihydroxylation. *Chem. Rev.* **94**, 2483-2547 (1994).

30 Goodby, J. W. Chirality in liquid-crystals. *J. Mater. Chem.* **1**, 307-318 (1991).

31 Moore, J. S. & Stupp, S. I. Materials Chemistry of Chiral Macromolecules. 1. Synthesis and Phase-Transitions. *J. Am. Chem. Soc.* **114**, 3429-3441 (1992).

32 Sone, E. D., Zubarev, E. R. & Stupp, S. I. Semiconductor nanohelices templated by supramolecular ribbons. *Angew. Chem. Int. Ed.* **41**, 1705-1709 (2002).

33 Gier, T. E., Bu, X. H., Feng, P. Y. & Stucky, G. D. Synthesis and organization of zeolite-like materials with three-dimensional helical pores. *Nature* **395**, 154-157 (1998).

34 Zhu, J. *et al.* Formation of chiral branched nanowires by the Eshelby Twist. *Nature Nanotech.* **3**, 477-481 (2008).

35 Orme, C. A. *et al.* Formation of chiral morphologies through selective binding of amino acids to calcite surface steps. *Nature* **411**, 775-779 (2001).

36 Cohen, A. E. & Mahadevan, L. Kinks, rings, and rackets in filamentous structures. *Proc. Natl. Acad. Sci. U. S. A.* **100**, 12141-12146 (2003).

37 Betz, O. & Kolsch, G. The role of adhesion in prey capture and predator defence in arthropods. *Arth. Struct. & Dev.* **33**, 3-30 (2004).

38 Neukirch, S. & van der Heijden, G. H. M. Geometry and mechanics of uniform n-plies: from engineering ropes to biological filaments. *J. Elasticity* **69**, 41-72 (2002).

39 Nicolson, M. M. The Interaction between Floating Particles. *Proc. Cambridge Philos. Soc.* **45**, 288-295 (1949).

40 Johnson, K. L. *Contact Mechanics*. (Cambridge University Press, 1985).

41 Ahuja, A. *et al.* Nanonails: A simple geometrical approach to electrically tunable superlyophobic surfaces. *Langmuir* **24**, 9-14 (2008).

42 Tuteja, A. *et al.* Designing superoleophobic surfaces. *Science* **318**, 1618-1622 (2007).

43 Collings, P. J. & Hird, M. *Introduction to Liquid Crystals*. (Taylor & Francis, 1997).

44 Hui, C. Y., Jagota, A., Lin, Y. Y. & Kramer, E. J. Constraints on microcontact printing imposed by stamp deformation. *Langmuir* **18**, 1394-1407 (2002).

45 Huang, Y. G. Y. *et al.* Stamp collapse in soft lithography. *Langmuir* **21**, 8058-8068 (2005).

46 Dev, A. & Chaudhuri, S. Uniform large-scale growth of micropatterned arrays of ZnO nanowires synthesized by a surfactant assisted approach. *Nanotechnology* **18**, 175607 (2007).

47 Liu, H., Zhai, J. & Jiang, L. Wetting and anti-wetting on aligned carbon nanotube films. *Soft Matter* **2**, 811-821 (2006).

48 Sidorenko, A., Krupenkin, T., Taylor, A., Fratzl, P. & Aizenberg, J. Reversible switching of hydrogel-actuated nanostructures into complex micropatterns. *Science* **315**, 487-490 (2007).

49 Kang, S. H., Pokroy, B., Mahadevan, L. & Aizenberg, J. Control of Shape and Size of Nanopillar Assembly by Adhesion-Mediated Elastocapillary Interaction. *ACS Nano* **4**, 6323-6331 (2010).

50 Lehn, J. M. Perspectives in Supramolecular Chemistry - from Molecular Recognition Towards Molecular Information-Processing and Self-Organization. *Angew. Chem. Int. Ed.* **29**, 1304-1319 (1990).

51 Whitesides, G. M., Mathias, J. P. & Seto, C. T. Molecular Self-Assembly and Nanochemistry - a Chemical Strategy for the Synthesis of Nanostructures. *Science* **254**, 1312-1319 (1991).

52 Whitesides, G. M. & Grzybowski, B. Self-assembly at all scales. *Science* **295**, 2418-2421 (2002).

53 Israelachvili, J. N., Mitchell, D. J. & Ninham, B. W. Theory of Self-Assembly of Hydrocarbon Amphiphiles into Micelles and Bilayers. *J. Chem. Soc., Faraday Trans. 2* **72**, 1525-1568 (1976).

54 Boncheva, M., Bruzewicz, D. A. & Whitesides, G. M. Millimeter-scale self-assembly and its applications. *Pure Appl. Chem.* **75**, 621-630 (2003).

55 Stauth, S. A. & Parviz, B. A. Self-assembled single-crystal silicon circuits on plastic. *Proc. Natl. Acad. Sci. U. S. A.* **103**, 13922-13927 (2006).

56 Grzybowski, B. A., Stone, H. A. & Whitesides, G. M. Dynamic self-assembly of magnetized, millimetre-sized objects rotating at a liquid-air interface. *Nature* **405**, 1033-1036 (2000).

57 Tien, J., Terfort, A. & Whitesides, G. M. Microfabrication through electrostatic self-assembly. *Langmuir* **13**, 5349-5355 (1997).

58 Adams, M., Dogic, Z., Keller, S. L. & Fraden, S. Entropically driven microphase transitions in mixtures of colloidal rods and spheres. *Nature* **393**, 349-352 (1998).

59 Bowden, N., Terfort, A., Carbeck, J. & Whitesides, G. M. Self-assembly of mesoscale objects into ordered two-dimensional arrays. *Science* **276**, 233-235 (1997).

60 Jacobs, H. O., Tao, A. R., Schwartz, A., Gracias, D. H. & Whitesides, G. M. Fabrication of a cylindrical display by patterned assembly. *Science* **296**, 323-325 (2002).

61 Rothemund, P. W. K. Using lateral capillary forces to compute by self-assembly. *Proc. Natl. Acad. Sci. U. S. A.* **97**, 984-989 (2000).

62 Smela, E., Inganas, O. & Lundstrom, I. Controlled Folding of Micrometer-Size Structures. *Science* **268**, 1735-1738 (1995).

63 Srinivasan, U., Liepmann, D. & Howe, R. T. Microstructure to substrate self-assembly using capillary forces. *J. MEMS* **10**, 17-24 (2001).

64 Syms, R. R. A. Surface tension powered self-assembly of 3-D micro-optomechanical structures. *J. MEMS* **8**, 448-455 (1999).

65 Chen, R. *et al.* Nanowires for Enhanced Boiling Heat Transfer. *Nano Lett.* **9**, 548-553 (2009).

66 De Volder, M. *et al.* Diverse 3D Microarchitectures Made by Capillary Forming of Carbon Nanotubes. *Adv. Mater.* **22**, 4384-4389 (2010).

67 Duan, H. & Berggren, K. K. Directed Self-Assembly at the 10 nm Scale by Using Capillary Force-Induced Nanocohesion. *Nano Lett.* **10**, 3710-3716 (2010).

68 Py, C., Bastien, R., Bico, J., Roman, B. & Boudaoud, A. 3D aggregation of wet fibers. *Europhys. Lett.* **77**, 44005 (2007).

69 Chandra, D., Yang, S., Soshinsky, A. A. & Gambogi, R. J. Biomimetic Ultrathin Whitening by Capillary-Force-Induced Random Clustering of Hydrogel Micropillar Arrays. *ACS Appl. Mater. Inter.* **1**, 1698-1704 (2009).

70 Chandra, D. & Yang, S. Stability of High-Aspect-Ratio Micropillar Arrays against Adhesive and Capillary Forces. *Acc. Chem. Res.* **43**, 1080-1091 (2010).

71 Jewell, S. A., Vukusic, P. & Roberts, N. W. Circularly polarized colour reflection from helicoidal structures in the beetle Plusiotis boucardi. *New J. Phys.* **9**, 99 (2007).

72 Vukusic, P., Sambles, J. R., Lawrence, C. R. & Wootton, R. J. Quantified interference and diffraction in single Morpho butterfly scales. *Proc. R. Soc. B* **266**, 1403-1411 (1999).

73 Webb, J. F. Neuromast Morphology and Lateral Line Trunk Canal Ontogeny in 2 Species of Cichlids - an Sem Study. *J. Morphol.* **202**, 53-68 (1989).

74 Boudaoud, A., Bico, J. & Roman, B. Elastocapillary coalescence: Aggregation and fragmentation with a maximal size. *Phys. Rev. E* **76**, 060102 (2007).

75 Liston, E. M., Martinu, L. & Wertheimer, M. R. Plasma Surface Modification of Polymers for Improved Adhesion - a Critical-Review. *J. Adhes. Sci. Technol.* **7**, 1091-1127 (1993).

76 Journet, C., Moulinet, S., Ybert, C., Purcell, S. T. & Bocquet, L. Contact angle measurements on superhydrophobic carbon nanotube forests: Effect of fluid pressure. *Europhys. Lett.* **71**, 104-109 (2005).

77 Chiodi, F., Roman, B. & Bico, J. Piercing an interface with a brush: Collaborative stiffening. *Europhys. Lett.* **90**, 44006 (2010).

78 Bernardino, N. & Dietrich, S. Comment on Biomimetic Ultrathin Whitening by Capillary-Force-Induced Random Clustering of Hydrogel Micropillar Arrays. *ACS Appl. Mater. Inter.* **2**, 603-604 (2010).

79 Lee, J. S., Ryu, J. & Park, C. B. Bio-inspired fabrication of superhydrophobic surfaces through peptide self-assembly. *Soft Matter* **5**, 2717-2720 (2009).

80 Pang, C. *et al.* Bioinspired Reversible Interlocker: Bioinspired Reversible Interlocker Using Regularly Arrayed High Aspect-Ratio Polymer Fibers *Adv. Mater.* **24**, 475-479 (2012).

81 Vukusic, P., Hallam, B. & Noyes, J. Brilliant whiteness in ultrathin beetle scales. *Science* **315**, 348-348 (2007).

82 Cheng, J. Y. *et al.* Formation of a cobalt magnetic dot array via block copolymer lithography. *Adv. Mater.* **13**, 1174-1178 (2001).

83 Hu, M. *et al.* Gold Nanofingers for Molecule Trapping and Detection. *J. Am. Chem. Soc.* **132**, 12820-12822 (2010).

84 Bico, J., Tordeux, C. & Quere, D. Rough wetting. *Europhys. Lett.* **55**, 214-220 (2001).

85 Brinker, C. J., Lu, Y. F., Sellinger, A. & Fan, H. Y. Evaporation-induced self-assembly: Nanostructures made easy. *Adv. Mater.* **11**, 579-585 (1999).

86 Huang, J. X., Kim, F., Tao, A. R., Connor, S. & Yang, P. D. Spontaneous formation of nanoparticle stripe patterns through dewetting. *Nature Mater.* **4**, 896-900 (2005).

87 Chakrapani, N., Wei, B. Q., Carrillo, A., Ajayan, P. M. & Kane, R. S. Capillarity-driven assembly of two-dimensional cellular carbon nanotube foams. *Proc. Natl. Acad. Sci. U. S. A.* **101**, 4009-4012 (2004).

88 Deegan, R. D. *et al.* Capillary flow as the cause of ring stains from dried liquid drops. *Nature* **389**, 827-829 (1997).

89 Harris, D. J., Hu, H., Conrad, J. C. & Lewis, J. A. Patterning colloidal films via evaporative lithography. *Phys. Rev. Lett.* **98**, 148301 (2007).

90 Hong, S. W., Byun, M. & Lin, Z. Q. Robust Self-Assembly of Highly Ordered Complex Structures by Controlled Evaporation of Confined Microfluids. *Angew. Chem. Int. Ed.* **48**, 512-516 (2009).

91 Duan, H. G. & Berggren, K. K. Directed Self-Assembly at the 10 nm Scale by Using Capillary Force-Induced Nanocohesion. *Nano Lett.* **10**, 3710-3716 (2010).

92 Kralchevsky, P. A. & Denkov, N. D. Capillary forces and structuring in layers of colloid particles. *Curr. Opin. Colloid Interface Sci.* **6**, 383-401 (2001).

93 Chandra, D. & Yang, S. Capillary-Force-Induced Clustering of Micropillar Arrays: Is It Caused by Isolated Capillary Bridges or by the Lateral Capillary Meniscus Interaction Force? *Langmuir* **25**, 10430-10434 (2009).

94 Amidror, I. *The theory of the Moiré phenomenon*. Vol. 1 pp. 1-3 (Kluwer Academic Publishers, 2000).

95 Nishijima, Y. & Oster, G. Moiré Patterns: Their Application to Refractive Index and RefractiveIndex Gradient Measurements. *J. Opt. Soc. Am.* **54**, 1-4 (1964).

96 Kloxin, C. J., Scott, T. F., Park, H. Y. & Bowman, C. N. Mechanophotopatterning on a Photoresponsive Elastomer. *Adv. Mater.* **23**, 1977-1981 (2011).

97 Chen, B. & Lu, K. Moire Pattern Nanopore and Nanorod Arrays by Focused Ion Beam Guided Anodization and Nanoimprint Molding. *Langmuir* **27**, 4117-4125 (2011).

98 Glass, L. Moire Effect from Random Dots. *Nature* **223**, 578-580 (1969).

99 Kang, S. H., Wu, N. & Aizenberg, J. *manuscript in preparation*.

100 Paulose, J., Nelson, D. R. & Aizenberg, J. Two-parameter sequential adsorption model applied to microfiber clustering. *Soft Matter* **6**, 2421-2434 (2010).

101 Kang, S. H., Salman, O. U., Kureh, J., Truskinovsky, L. & Aizenberg, J. *manuscript in preparation*.

102 National Research Council Committee on Synthetic Hierarchical Structures. *Hierarchical Structures in Biology as a Guide for New Materials Technology*. (The National Academies Press, 1994).

103 Brinker, C. J. Evaporation-induced self-assembly: Functional nanostructures made easy. *MRS Bull.* **29**, 631-640 (2004).

104 Lee, Y. W., Park, S. H., Kim, K. B. & Lee, J. K. Fabrication of hierarchical structures on a polymer surface to mimic natural superhydrophobic surfaces. *Adv. Mater.* **19**, 2330-2335 (2007).

105 He, Y. *et al.* Hierarchical self-assembly of DNA into symmetric supramolecular polyhedra. *Nature* **452**, 198-201 (2008).

106 Yang, P. D. *et al.* Hierarchically ordered oxides. *Science* **282**, 2244-2246 (1998).

107 Lin, Y. *et al.* Self-directed self-assembly of nanoparticle/copolymer mixtures. *Nature* **434**, 55-59 (2005).

108 Boker, A. *et al.* Hierarchical nanoparticle assemblies formed by decorating breath figures. *Nature Mater.* **3**, 302-306 (2004).

109 Byun, M. *et al.* Controlled evaporative self-assembly of hierarchically structured regioregular conjugated polymers. *Soft Matter* **5**, 1583-1586 (2009).

110 Bernardino, N. R., Blickle, V. & Dietrich, S. Wetting of Surfaces Covered by Elastic Hairs. *Langmuir* **26**, 7233-7241 (2010).

111 Duan, H., Yang, J. K. W. & Berggren, K. K. Controlled Collapse of High-Aspect-Ratio Nanostructures. *Small* **7**, 2661-2668 (2011).

112 Matsunaga, M., Aizenberg, M. & Aizenberg, J. Controlling the Stability and Reversibility of Micropillar Assembly by Surface Chemistry. *J. Am. Chem. Soc.* **133**, 5545-5553 (2011).

113 Yue, T. T. & Zhang, X. R. Self-Assembly of Semiflexible Homopolymers into Helical Bundles: A Brownian Dynamics Simulation Study. *J. Phys. Chem. B* **115**, 11566-11574 (2011).

114 Jarai-Szabo, F., Horvat, E. A., Vajtai, R. & Neda, Z. Spring-block approach for nanobristle patterns. *Chem. Phys. Lett.* **511**, 378-383 (2011).

115 Kim, A. *et al.* Study of Molecular Trapping Inside Gold Nanofinger Arrays on Surface-Enhanced Raman Substrates. *J. Am. Chem. Soc.* **133**, 8234-8239 (2011).

116 Crandall, S. H., Dahl, N. C. & Lardner, T. J. *An Introduction to the Mechanics of Solids*. 2nd edn. (McGraw-Hill 1978).

117 Aizenberg, J., He, X., Kang, S. H. & Wong, T. S. Anti-Counterfeiting Methods in Security Documents. Patent application in preparation (2012).

118 Wilson, G. J. Australian polymer banknote: a review *Proc. SPIE* **3314**, 2–7 (1998).

119 Solomon, D. H., Ross, J. B., Girolamo, M. & Brett, R. A. Banknotes and the like. U.S. patent No.: US 4,536,016 (1985).

120 Coventry, L. Life of polymer currency notes – a study in *XV Rim Banknote Printers' Conference.* (2001).

121 Benoit, G. L. & Velden, R. V. Cross-laminated multilayer film structures for use in the production of banknotes or the like. U.S. patent No.: US 5,716,695 (1998).

122 Benoit, G. L. & Velden, R. V. Multilayer film structures for use in the production of banknotes or the like. US patent No.: US 5,698,333 (1997).

123 *Secrets of making money* <http://www.pbs.org/wgbh/nova/transcripts/2314secr.html> (1996).

124 *The world's first polymer banknote* <http://www.csiro.au/science/World-first-polymer-banknote.html> (2007).

125 *Independent states in the world* <http://www.state.gov/s/inr/rls/4250.htm> (2009).

126 The new paradigm in currency. (International Polymer Currency Association Bulletin, 2007).

127 Jackson, W. K. Embossing of banknotes or the like with security devices. US patent No.: US 5,915,731 (1999).

128 Jackson, W. K. Embossing of bank notes or the like with security devices. US patent No.: US 6,176,522 B1 (2001).

129 Jackson, W. K. & Goodman, R. A. Diffraction grating. US patent No.: US 5,335,113 (1994).

130 Leech, P. W. & Lee, R. A. Hot embossing of diffractive optically variable images in biaxially-oriented polypropylene. *Microelectron Eng.* **84**, 25-30 (2007).

131 Leech, P. W., Lee, R. A., Sexton, B. A. & Smith, F. Hot embossing of micrographic elements in polypropylene. *Microelectron Eng.* **84**, 109-113 (2007).

132 Vukusic, P. Evolutionary Photonics with a Twist. *Science* **325**, 398-399 (2009).

133 Shawkey, M. D., Morehouse, N. I. & Vukusic, P. A protean palette: colour materials and mixing in birds and butterflies. *J. R. Soc. Interface* **6**, S221-S231 (2009).

134 Vukusic, P. & Hooper, I. Directionally controlled fluorescence emission in butterflies. *Science* **310**, 1151-1151 (2005).

135 Vukusic, P. & Sambles, J. R. Photonic structures in biology. *Nature* **424**, 852-855 (2003).

136 Wenzel, R. N. Resistance of solid surfaces to wetting by water. *Ind. Eng. Chem.* **28**, 988-994 (1936).

137 Koch, K., Blecher, I. C., Koenig, G., Kehraus, S. & Barthlott, W. The superhydrophilic and superoleophilic leaf surface of Ruellia devosiana (Acanthaceae): a biological model for spreading of water and oil on surfaces. *Funct. Plant Biol.* **36**, 339-350 (2009).

138 Dorrer, C. & Ruhe, J. Mimicking the stenocara beetle-dewetting of drops from a patterned superhydrophobic surface. *Langmuir* **24**, 6154-6158 (2008).

139 Lai, P., Lu, Y.-T. & Wu, C.-C. Anti-counterfeit method and system by using a nano metal grating. US patent No.: US 7,113,690 B2 (2006).

140 Lopata, H. Fraud resistant credit card system. US patent No.: US 4,641,017 (1987).

141 Mallik, D. W. Holograms with discontinuous metallization including alpha-numeric shapes. US patent No.: US 5,142,383 (1992).

142 Xia, Y. N. & Whitesides, G. M. Soft lithography. *Annu. Rev. Mater. Sci.* **28**, 153-184 (1998).

143 Goldstein, J. I. *et al. Scanning Electorn Microscopy and X-ray Microanalysis* (Plenum Press, 1992).

144 Henderson, R. & Glaeser, R. M. Quantitative-Analysis of Image-Contrast in Electron-Micrographs of Beam-Sensitive Crystals. *Ultramicroscopy* **16**, 139-150 (1985).

145 Glaeser, R. M. Retrospective: Radiation damage and its associated "Information Limitations". *J. Struct. Biol.* **163**, 271-276 (2008).

146 Kim, T. I., Jeong, H. E., Suh, K. Y. & Lee, H. H. Stooped Nanohairs: Geometry-Controllable, Unidirectional, Reversible, and Robust Gecko-like Dry Adhesive. *Adv. Mater.* **21**, 2276-2281 (2009).

147 Glaeser, R. M. & Downing, K. H. Specimen charging on thin films with one conducting layer: Discussion of physical principles. *Microsc. Microanal.* **10**, 790-796 (2004).

148 Ragab, A. R. & Bayoumi, S. E. A. *Engineering Solid Mechanics: Fundamentals and Applications*. (CRC Press, 1998).

149 Cazaux, J. Mechanisms of charging in electron spectroscopy. *J. Electron. Spectrosc. Relat. Phenom.* **105**, 155-185 (1999).

150 Cazaux, J. Electron probe microanalysis of insulating materials: Quantification problems and some possible solutions. *X-Ray Spectrom.* **25**, 265-280 (1996).

151 Landau, L. & Lifshitz, L. *Theory of Elasticity*. (Addison-Wesley, 1959).

152 Jackson, J. D. *Classical Electrodynamics*. (Wiley, 1962).

153 Vettiger, P. *et al.* The "millipede" - Nanotechnology entering data storage. *IEEE. Trans. Nanotechnol.* **1**, 39-55 (2002).

154 Badzey, R. L., Zolfagharkhani, G., Gaidarzhy, A. & Mohanty, P. A controllable nanomechanical memory element. *Appl. Phys. Lett.* **85**, 3587-3589 (2004).

155 Kang, S. H. *et al. Manuscript in preparation*.

156 Pasteur, L. Mémoire sur la relation qui peut exister entre la forme cristalline et la composition chimique, et sur la cause de la polarisation rotatoire. *Hebd. Séanc. Acad. Sci. Paris* **26**, 535–538 (1848).

157 Barron, L. D. True and false chirality and absolute asymmetric-synthesis. *J. Am. Chem. Soc.* **108**, 5539-5542 (1986).

158 Schulte, E. & Weiss, A. I. Chirality and projective linear-groups. *Discrete Math.* **131**, 221-261 (1994).

159 Crewther, R. J. Chirality selection-rules and U(1) problem. *Phys. Lett. B* **70**, 349-354 (1977).

160 De Camp, W. H. Specification of molecular chirality. *Chirality* **1**, 97-98 (1989).

161 Taniguchi, K. *et al.* Chirality in planar cell shape contributes to left-right asymmetric epithelial morphogenesis. *Science* **333**, 339-341 (2011).

162 Qing, G. & Sun, T. The transformation of chiral signals into macroscopic properties of materials using chirality-responsive polymers. *NPG Asia Materials* **4** (2012).

163 Ribo, J. M., Crusats, J., Sagues, F., Claret, J. & Rubires, R. Chiral sign induction by vortices during the formation of mesophases in stirred solutions. *Science* **292**, 2063-2066 (2001).

164 Soai, K., Shibata, T., Morioka, H. & Choji, K. Asymmetric autocatalysis and amplification of enantiomeric excess of a chiral molecule. *Nature* **378**, 767-768 (1995).

165 Weissbuch, I., Addadi, L., Lahav, M. & Leiserowitz, L. Molecular recognition at crystal interfaces. *Science* **253**, 637-645 (1991).

166 Chen, H. P. *et al.* Glassy liquid-crystal films,with opposite chirality as high-performance optical notch filters and reflectors. *Adv. Mater.* **12**, 1283-1286 (2000).

167 Hendry, E. *et al.* Ultrasensitive detection and characterization of biomolecules using superchiral fields. *Nature Nanotech.* **5**, 783-787 (2010).

168 Bettini, P. *et al.* Composite chiral structures for morphing airfoils: Numerical analyses and development of a manufacturing process. *Compos. Part B-Eng.* **41**, 133-147 (2010).

169 Gibson, L. J. & Ashby, M. F. *Cellular Solids: Structure and Properties*. (Cambridge University Press, 1988).

170 Mansfield, E. H. *The Bending and Stretching of Plates* 2nd edn. (Cambridge University Press, 1989).

171 Föppl, A. *Vorlesungen über technische Mechanik*. 132 (B.G. Teubner, 1907).

172 von Kármán, T. Festigkeitsproblem im Maschinenbau. *Encyk. D. Math. Wiss. IV* (1910).

173 Kittel, C. *Introduction to Solid State Physics*. 8th edn. (Wiley, 2005).

174 Triantafyllidis, N. & Schraad, M. W. Onset of failure in aluminum honeycombs under general in-plane loading. *J. Mech. Phys. Solids* **46**, 1089-1124 (1998).

175 Han, Y. L. *et al.* Geometric frustration in buckled colloidal monolayers. *Nature* **456**, 898-903 (2008).

176 Jang, J. H., Koh, C. Y., Bertoldi, K., Boyce, M. C. & Thomas, E. L. Combining pattern instability and shape-memory hysteresis for phononic switching. *Nano Lett.* **9**, 2113-2119 (2009).

177 Queheillalt, D. T. & Wadley, H. N. G. Cellular metal lattices with hollow trusses. *Acta Mater.* **53**, 303-313 (2005).

178 Baggetto, L., Danilov, D. & Notten, P. H. L. Honeycomb-structured silicon: Remarkable morphological changes induced by electrochemical (de)lithiation. *Adv. Mater.* **23**, 1563-1566 (2011).

179 Tsuchiya, M., Lai, B.-K. & Ramanathan, S. Scalable nanostructured membranes for solid-oxide fuel cells. *Nature Nanotech.* (2011).

180 Papka, S. D. & Kyriakides, S. Inplane compressive response and crushing of honeycomb. *J. Mech. Phys. Solids* **42**, 1499-1532 (1994).

181 Deshpande, V. S. & Fleck, N. A. High strain rate compressive behaviour of aluminium alloy foams. *Int. J. Impact Eng.* **24**, 277-298 (2000).

182 Verdejo, R. *et al.* Enhanced acoustic damping in flexible polyurethane foams filled with carbon nanotubes. *Compos. Sci. Technol.* **69**, 1564-1569 (2009).

183 Yoshida, R. *et al.* Comb-type grafted hydrogels with rapid de-swelling response to temperature-changes. *Nature* **374**, 240-242 (1995).

184 Philippova, O. E., Hourdet, D., Audebert, R. & Khokhlov, A. R. pH-responsive gels of hydrophobically modified poly(acrylic acid). *Macromolecules* **30**, 8278-8285 (1997).

185 Holtz, J. H. & Asher, S. A. Polymerized colloidal crystal hydrogel films as intelligent chemical sensing materials. *Nature* **389**, 829-832 (1997).

186 Cai, S. Q., Bertoldi, K., Wang, H. M. & Suo, Z. G. Osmotic collapse of a void in an elastomer: breathing, buckling and creasing. *Soft Matter* **6**, 5770-5777 (2010).

187 Pelrine, R., Kornbluh, R., Pei, Q. B. & Joseph, J. High-speed electrically actuated elastomers with strain greater than 100%. *Science* **287**, 836-839 (2000).

188 Qiu, Y. & Park, K. Environment-sensitive hydrogels for drug delivery. *Adv. Drug Deliver. Rev.* **53**, 321-339 (2001).

189 Barthlott, W. & Neinhuis, C. Purity of the sacred lotus, or escape from contamination in biological surfaces. *Planta* **202**, 1-8 (1997).

190 Cassie, A. B. D. & Baxter, S. Wettability of porous surfaces. *Trans. Faraday Soc.* **40**, 0546 – 0550 (1944).

191 Cassie, A. B. D. & Baxter, S. Large contact angles of plant and animal surfaces. *Nature* **155**, 21-22 (1945).

192 Shafrin, E. G. & Zisman, W. A. Constitutive relations in the wetting of low energy surfaces and the theory of the retraction method of preparing monolayers. *J. Phys. Chem.* **64**, 519-524 (1960).

193 Nguyen, T. P. N., Brunet, P., Coffinier, Y. & Boukherroub, R. Quantitative testing of robustness on superomniphobic surfaces by drop impact. *Langmuir* **26**, 18369-18373 (2010).

194 Quere, D. Wetting and roughness. *Annu. Rev. Mater. Res.* **38**, 71-99 (2008).

195 Bocquet, L. & Lauga, E. A smooth future? *Nature Mater.* **10**, 334-337 (2011).

196 Tuteja, A., Choi, W., Mabry, J. M., McKinley, G. H. & Cohen, R. E. Robust omniphobic surfaces. *Proc. Natl. Acad. Sci. U. S. A.* **105**, 18200-18205 (2008).

197 Li, Y., Li, L. & Sun, J. G. Bioinspired self-healing superhydrophobic coatings. *Angew. Chem. Int. Ed.* **49**, 6129-6133 (2010).

198 Bohn, H. F. & Federle, W. Insect aquaplaning: Nepenthes pitcher plants capture prey with the peristome, a fully wettable water-lubricated anisotropic surface. *Proc. Natl. Acad. Sci. U. S. A.* **101**, 14138-14143 (2004).

199 Bauer, U. & Federle, W. The insect-trapping rim of Nepenthes pitchers: Surface structure and function. *Plant Signal. Behav.* **4**, 1019–1023 (2009).

200 Federle, W., Riehle, M., Curtis, A. S. G. & Full, R. J. An integrative study of insect adhesion: Mechanics and wet adhesion of pretarsal pads in ants. *Integr. Comp. Biol.* **42**, 1100-1106 (2002).

201 Courbin, L. *et al.* Imbibition by polygonal spreading on microdecorated surfaces. *Nature Mater.* **6**, 661-664 (2007).

202 Fowkes, F. M. Attractive Forces at Interfaces. *Ind. Eng. Chem.* **56**, 40 - 42 (1964).

203 Israelachvili, J. N. *Intermolecular and surface forces*. 3rd edn. (Academic Press, 2011).

204 Xu, Q. B., Mayers, B. T., Lahav, M., Vezenov, D. V. & Whitesides, G. M. Approaching zero: Using fractured crystals in metrology for replica molding. *J. Am. Chem. Soc.* **127**, 854-855 (2005).

205 Chen, W. *et al.* Ultrahydrophobic and ultralyophobic surfaces: Some comments and examples. *Langmuir* **15**, 3395-3399 (1999).

206 Delmas, M., Monthioux, M. & Ondarcuhu, T. Contact Angle Hysteresis at the Nanometer Scale. *Phys. Rev. Lett.* **106**, 136102 (2011).

207 Furmidge, C. G. Studies at Phase Interfaces.1. Sliding of Liquid Drops on Solid Surfaces and a Theory for Spray Retention. *J. Coll. Sci.* **17**, 309-324 (1962).

208 Lee, C. & Kim, C. J. Underwater Restoration and Retention of Gases on Superhydrophobic Surfaces for Drag Reduction. *Phys. Rev. Lett.* **106**, 014502 (2011).

209 Ishino, C., Reyssat, M., Reyssat, E., Okumura, K. & Quere, D. Wicking within forests of micropillars. *Europhys. Lett.* **79**, 56005 (2007).

210 Nakajima, A., Fujishima, A., Hashimoto, K. & Watanabe, T. Preparation of transparent superhydrophobic boehmite and silica films by sublimation of aluminum acetylacetonate. *Adv. Mater.* **11**, 1365-1368 (1999).